Active Flows and Networks

by

Aden Forrow

Submitted to the Department of Mathematics
in partial fulfillment of the requirements for the degree of

Doctor of Philosophy

at the

MASSACHUSETTS INSTITUTE OF TECHNOLOGY

June 2018

Author ..... Signature redacted

Department of Mathematics
May 4, 2018

Certified by ..... Signature redacted

Jörn Dunkel
Assistant Professor
Thesis Supervisor

Accepted by ..... Signature redacted

Jonathan Kelner
Chairman, Department Committee on Graduate Theses

Active Flows and Networks

by

Aden Forrow

Submitted to the Department of Mathematics
on May 4, 2018, in partial fulfillment of the
requirements for the degree of
Doctor of Philosophy

Abstract

Coherent, large scale dynamics in many nonequilibrium physical, biological, or information transport networks are driven by small-scale local energy input. In the first part of this thesis, we introduce and explore two analytically tractable nonlinear models for such active flow networks, drawing motivation from recent microfluidic experiments on bacterial and other microbial suspensions. In contrast to equipartition with thermal driving, we find that active friction selects discrete states with only a limited number of modes excited at distinct fixed amplitudes. When the active transport network is incompressible, these modes are cycles with constant flow; when it is compressible, they are oscillatory. As is common in such network dynamical systems, the spectrum of the underlying graph Laplacian plays a key role in controlling the flow. Spectral graph theory has traditionally prioritized analyzing Laplacians of unweighted networks with specified adjacency properties. For the second part of the thesis, we introduce a complementary framework, providing a mathematically rigorous positively weighted graph construction that exactly realizes any desired spectrum. We illustrate the broad applicability of this approach by showing how designer spectra can be used to control the dynamics of three archetypal physical systems. Specifically, we demonstrate that a strategically placed gap induces weak chimera states in Kuramoto-type oscillator networks, tunes or suppresses pattern formation in a generic Swift-Hohenberg model, and leads to persistent localization in a discrete Gross-Pitaevskii quantum network.

Thesis Supervisor: Jörn Dunkel
Title: Assistant Professor

Acknowledgments

This is a summary of deeply collaborative work, and so I gratefully acknowledge the contributions of everyone who has helped me along the way. Particular thanks go to my advisor, Jörn Dunkel, who was indispensible both in inspiring and executing these projects and as a wonderful graduate mentor, as well as to our close collaborator Francis Woodhouse without whom we would have far fewer results to share, described less well, with less pretty figures.

My graduate work was generously supported by the National Science Foundation and the MIT Mathematics Department.

Contents

1 Introduction **25**

1.1 Active flows 25

1.2 Graph Laplacians 27

2 Incompressible flow networks **31**

2.1 Model 31

2.1.1 Lattice ϕ^6 field theory for active flow networks 31

2.1.2 Network dynamics 35

2.2 Results 37

2.2.1 Stochastic cycle selection 37

2.2.2 Waiting times and graph symmetries 39

2.2.3 Transition rate estimation 41

2.2.4 Edge girth determines rate band structure 43

2.2.5 Asymmetric networks 44

2.3 Discussion 48

2.3.1 Incompressible limit 48

2.3.2 Low temperature limit and ice-type models 52

2.3.3 Complex networks 54

2.4 Numerical methods 56

2.4.1 Numerical integration and waiting times 56

2.4.2 Graph generation and properties 56

2.5 Conclusions 56

3 Compressible active flow networks **59**

3.1 Model 60

3.1.1 Weight scaling and nondimensionalization 60

3.1.2 Relation to physical flow systems 62

3.1.3 Compressibility 64

3.2 Mode selection 66

3.2.1 Rayleigh friction approximation 67

3.2.2 Perturbation expansion 69

3.2.3 Leading order amplitude dynamics 70

3.2.4 Accuracy of Rayleigh friction approximation 74

3.2.5 One- and two-mode selection 74

3.2.6 Differential growth rates 79

3.2.7 Higher order oscillations 80

3.3 Stochastic forcing 82

3.3.1 Thermalization 83

3.4 Complex networks 85

3.4.1 Attractor characteristics on tree networks 85

3.4.2 Networks with cycles 87

3.4.3 Band gaps 88

3.5 Conclusions 89

4 Designing spectra **91**

4.1 Discrete band gaps 91

4.2 Network construction and sparsification 93

4.2.1 Spectral graph construction 94

4.2.2 Sparsification 98

4.3 Applications 99

4.3.1 Random matched-degree graphs 101

4.3.2 Kuramoto oscillators 101

4.3.3 Swift-Hohenberg pattern formation 105

4.3.4 Gross-Pitaevskii localization 109
4.4 Band structure in periodic networks 112
4.5 Conclusions 114

List of Figures

1-1 Active driving interacts with networks in diverse biological systems. (a) In Drosophila embryos, networks of ATP-driven myosin motors (fluorescently labeled in green) couple to the cell boundaries (magenta) to control tissue folding [33]. (b) The slime mold *Physarum polycephalum* (yellow) can form complex optimized transport networks to connect food sources like the oat flakes (white dots) shown. Here, the food was placed in roughly the pattern of population centers around Tokyo. The organism's final state is reminiscent of the human-designed rail system [131]. (c) Microtubules and kinesin motors like these from the Dogic lab can be confined to channels where they drive coherent shape-dependent flows [147]. (d) Our theoretical work models most closely confined suspensions of swimming microbes. In this picture, from preliminary experiments by the Kantsler lab, sperm cells are confined to a network of channels in a microfluidic chamber with barriers (light gray polygons). 28

2-1 Stochastic cycle selection in two elementary graphs. (a) Flux–time traces from Eq. 2.4 for each of the three edges in the graph shown, signed according to the edges' arrows, with three different temporary configurations highlighted as indicated by (i)–(iii). $\lambda = 2.5$, $\mu = 25$, $\beta^{-1} = 0.05$. (b) Same as (a), but with an additional edge in the graph. States are more stable with even-degree vertices, since flux conserving flows are possible with all edges flowing. 32

2-2 Noise and activity cause stochastic cycle selection. (a–c) Flux–time traces (b) for each edge of the complete graph on four vertices, K_4. Edge orientations are as in (a). The sub-diagrams in (c)(i–iv) exemplify the flow state in the corresponding regions of the trace. Parameters $\lambda = 2.5$, $\mu = 25$, $\beta^{-1} = 0.05$. (d–f) As in (a–c), but for the generalized Petersen graph $P_{3,1}$. The same switching behavior results, but now with more cycle states. (g) Survival function $S(t) = \mathbb{P}(T > t)$ of the transition waiting time T for an edge in K_4, at regularly-spaced values of λ in $2 \leqslant \lambda \leqslant 3$ with $\mu = 25$, $\beta^{-1} = 0.05$. Log-scaled vertical; straight lines imply an exponential distribution at large t. Inset: $S(t)$ at small t with log-scaled vertical, showing non-exponential behavior. (h,i) Slow and fast edge transition rates in K_4, with parameters as in (g). Circles are from fitting T to a mixture of two exponential distributions, lines show best-fit theoretical rates $k \propto \lambda \exp(-\beta \Delta H)$ with ΔH calculated for transitions between 3- and 4-cycles. (j) Transition rate $k = \langle T \rangle^{-1}$ for each set of equivalent edges in $P_{3,1}$, as per the key, as a function of λ, with $\mu = 25$, $\beta^{-1} = 0.05$. Log-scaled vertical shows exponential dependence on λ. 38

2-3 Transition rates in highly symmetric graphs are determined by cycle structure. (a) Transition rate for edges in the first eight generalized Petersen graphs with $\lambda = 2.5$, $\mu = 25$, $\beta^{-1} = 0.05$. The rate was determined for each edge, then averaged within classes of equivalent edges. Symbols denote the rate for each class, categorized by e-girth g_e as in the key. The range of computed rates within each class is smaller than the symbols. (b) The graphs in (a) with their edge equivalence classes when more than one exists. Edges colors denote g_e as in (a). Observe that identical e-girth does not imply equivalence of edges. . 43

2-4 Cycle structure determines edge transition rates in asymmetric graphs. (a) Transition rate for each edge in 20 random asymmetric bridgeless cubic graphs on 21 edges. Markers denote e-girth g_e as per the key in (c). $\lambda = 2.5$, $\mu = 25$, $\beta^{-1} = 0.05$. (b) One of the graphs in (a), corresponding to the marked column ($\star$). Edges colored and labelled according to g_e. All 20 graphs are shown in Fig. 2-5. (c) Transition rates k from (a) binned by girth-weighted rate R_g, using best-fit value $\alpha = 1.31$, with markers denoting g_e as per the key. Horizontal error bars are range of marker position over 95% confidence interval in α, vertical error bars are ± 1 standard deviation in k within each group. Solid line is best fit $k = \gamma R_g$, dashed lines are 95% prediction intervals on k with α fixed. 45

2-5 The 20 non-isomorphic asymmetric cubic graphs in Fig. 2-4. Edges are colored according to e-girth as indicated in graph 1 and in Fig. 2-4. Graph 19 is that illustrated in Fig. 2-4b. All planar graphs (2, 3, 5, 6, 7, 12, 16 and 19) are shown in a planar embedding. 46

2-6 Constructing a cycle basis for $P_{4,1}$. (a) A planar embedding of $P_{4,1}$, with edges numbered and oriented as shown. (b) The dual of the embedding in (a), with dual graph vertices (original graph faces) numbered as shown. Edge orientations depend on those chosen in (a), as described in the text. Vertex 6 and its incident edges, highlighted, correspond to the external face whose flux is fixed at zero. 50

2-7 Incompressible flow on planar graphs can be represented using a face-based cycle basis. (a) Flux–time traces for flow about each of the internal faces of $P_{4,1}$, as labelled in (c), from Eq. (2.11) with $\lambda = 2.5$, $\beta^{-1} = 0.05$. (b) Zoom of trace showing a transition between two 8-cycles, which are global minima, via a 6-cycle. (c) Distinct state configurations in (b) of face fluxes (upper) and corresponding edge flows (lower). 52

2-8 Incompressible flow on a 15×15 hexagonal lattice using the face cycle basis. (a) Plot of flux values over time for each face in an integration on the 15×15 lattice, at $\lambda = 2.5$, $\mu = 25$, $\beta^{-1} = 0.05$. (b,c) Configurations of the face fluxes at the times marked in (a), along with the cycle configurations they represent. Cycles are colored according to their orientation clockwise (cyan) or counterclockwise (magenta). Faces are ordered in (a) column-wise from bottom-left to top-right of the lattice. 53

2-9 Empirical probability distributions of e-girth determined from ten graph realizations each from four random 1000-vertex graph ensembles: (a) fixed degree 3, i.e. cubic; (b) uniform with 1500 edges; (c) 'scale free' Barabási–Albert with a degree $k = 2$ vertex added at every step; and (d) 'small world' Watts–Strogatz with rewiring probability $p = 0.5$ and mean degree $k = 4$. The pseudo-real-life networks of (c) and (d) exhibit distributions with far more small e-girth edges than the more generic random graphs in (a) and (b). 55

3-1 Our active network model exhibits behavior similar to the topological edge modes of Ref. [124]. (a) A discretized version of the Lieb lattice considered in Ref. [124]. Edges shared by adjacent 8-cycles have weight $w_e = 2$ to account for the additional width of the corresponding channels. The most stable flow on this network consists of a lattice of counter-rotating cycles, in which both the active friction term $g(\mu, \phi_e/\sqrt{w_e})$ and the pressure variations ϱ_v are everywhere zero. (b) This lattice has modes confined to the edges of the domain, allowing sound waves to propagate and decay without scattering into the bulk (cf. discussion in App. I.B of Ref. [124]); one such mode is pictured. Simulations started in this mode as a perturbation to the most stable flow pattern do not cause density changes in the center. The network model allows study of such phenomena without resorting to full scale simulation of the flow patterns. 65

3-2 Activity can select a single dominant oscillation mode on hierarchically weighted networks. (a) The edges in the graph simulated in (b) and (c) are given weights decreasing exponentially with their distance from the central red path. (b) Oscillations in pressure and flux develop primarily along the central high-weight path. (c) Edge fluxes ϕ_e settle into steady synchronized oscillations as exemplified for two edges indicated in (b), one on (ϕ_{17}) and one off (ϕ_{59}) the path. (d) Plotting the time-dependent amplitude of each analytically-determined flow eigenmode confirms selection of a single oscillatory mode. The ten modes with the highest average amplitude in this simulation run are pictured; the marked top two rows are oscillatory modes, while the remaining rows are cyclic modes. See Fig. 3-3 for all modes. Simulation parameters are $\epsilon = 0.1$, $\mu = 1$, and $D = 10^{-4}$. 67

3-3 Including all of the modes from the simulation in Fig. 3-2 shows clear single mode selection on this weighted network. Edges a distance d from the central red path were given weight e^{-d}. Modes are ordered by frequency from high (top) to low (bottom); the last thirty modes, marked in red, are cycles. The modes pictured in Fig. 3-2 are marked in black. 68

3-4 Steady state amplitudes A_i as a function of activity μ for the tree pictured undergo a Hopf bifurcation as μ crosses 0. Dots are long-time root-mean-square amplitudes from simulations started in each mode; lines are numerical solutions of Eq. (3.20). Mode A_2 is too unstable to reliably observe in simulations, so it is omitted. For $\mu < 0$, all amplitudes go to zero in simulations; the dot included in that region is at $\mu = -1$ where the friction is purely passive. Some deviations between simulation and analytics are expected because the simulations do not use the Rayleigh friction approximation and $\epsilon \neq 0$. Parameters are $\epsilon = 0.5$ and $D = 0$. 75

3-5 First order perturbation theory accurately predicts the stable states on small trees. (a) A five vertex tree possessing four nontrivial modes, as illustrated. (b) On the tree in (a), mode amplitudes settle into one of two stable stationary states, as seen in simulations for three different initial conditions. Modes are ordered by frequency from high (top) to low (bottom). (c) Simulated mode trajectories (rainbow) in (b) match analytic predictions (blue streamlines) in the subspaces of activated modes. There are three possible arrangements of nonzero critical points in each 2D subspace: a saddle point on one axis and a stable node on the other axis (left), a stable node on each axis and a saddle point in the middle (center), or a saddle point on each axis and a stable node in the middle (right). Higher order effects cause both the convergence to a point with $A_2 > 0$ in the left and middle plots and the oscillations in the trajectories. Parameters used are $\epsilon = 0.5$, $\mu = 1$, $D = 0$. 77

3-6 States on larger trees possess surprisingly few active modes, which can be inferred from time series with non-zero noise. (a) The mean number of stationary states of Eq. (3.13) grows exponentially with edges E as $1.77^E \approx (2^E)^{4/5}$ (solid orange line), close to the upper bound of 2^E states (dashed black line), while the mean number of stable states grows as $1.21^E \approx (2^E)^{1/4}$ (solid blue line). We counted states on all nonisomorphic trees with $E \leq 14$ edges (filled circles) and on a random sample of ~ 175 trees per point for $15 \leq E \leq 24$ (open circles). Averages are over trees with a fixed number of edges. (b) As E increases, both the mean and the variance of the distribution of trees with each number of stable states increase rapidly. (c) Distribution of the average number of modes active in a stable state. The mean over trees scales like $0.26E \approx E/4$ (solid line), significantly below $E/2$ expected if modes were selected randomly. (d) Two example trees indicated in (a-c) by the corresponding colored symbols. Stable states on paths ($\times$) always only activate one mode; complex trees ($+$) have more modes active. (e) Noisy networks ($D > 0$) transition stochastically between stable states, exemplified by an amplitude-time trace for the tree shown. Modes are ordered by frequency from high (top) to low (bottom). Simulation parameters are $\epsilon = 0.5$, $\mu = 1$, $D = 5 \times 10^{-3}$. (f) States found by vbFRET from simulations on the tree in (e). The second, first, and fifth columns are states seen in (e), indicated by the colored bars above. (g) States predicted by Eq. (3.13) for the tree in (e). The first five states in (f) match those in (g); the sixth column in (f) is likely a transient combination of analytically stable states. . . . 78

3-7 Slow global oscillations emerge from the fast active dynamics. (a) First order considerations fix a constant mean flow energy; higher order effects cause significant slow oscillations about that mean. Simulation parameters were $\mu = 1$, $\epsilon = 0.5$, and $D = 0$; the tree used is inset. (b) The mode amplitudes A_2 and A_3, like the energy, oscillate much more slowly than the harmonic oscillations of f_2 and f_3. All other mode amplitudes (unlabelled traces) are close to zero. (c) Frequency spectra of the two active modes and the energy H for the simulation in (a) and (b). The energy oscillates due to higher-order interactions between modes at frequencies that are linear combinations of active mode frequencies, not the harmonic frequencies alone (dashed lines). 81

3-8 Activity causes depth-dependent separation of time scales on a large tree. (a) Most pressure variation occurs near the leaves on large binary trees. (b) The tree in (a) develops an activity-driven steady state with slow oscillations in the center and fast oscillations near the edges, as illustrated by the flux ϕ_e on the three edges labelled in (a). (c) Unnormalized correlations between the Fourier transforms of the flux through the edges of the tree in (a), with phases ignored. Colors indicate the tree level of the tail vertex of the edge. There are strong correlations within each level and between neighboring levels, but low correlations for edges in widely-separated levels. (d) Frequency spectra of each tree level, computed by taking Fourier transforms of the edge fluxes as in (c) and averaging the magnitudes across all edges at each level. A distinct primary oscillation frequency for each level can be seen, which increases with distance from the tree center. Simulation parameters in all panels are $\epsilon = 0.5$, $\mu = 1$, and $D = 10^{-3}$. (e-h) While adding edges in the center leads to steady flow on cycles there, frequency still increases with distance from the center in the outer, tree-like sections. 86

3-9 Lower energy modes transition more often for the graph in Fig. 3-6. Modes are ordered by frequency from high (top) to low (bottom). Simulation parameters are $\epsilon = 0.5$, $\mu = 1$, $D = 5 \times 10^{-3}$, identical to those in Fig. 3-6. Note that rows 7 and 8, the two modes that switch on and off most, are degenerate. 87

3-10 States on graphs with cycles, like the one shown, tend to be more stable. Modes are ordered by frequency from high (top) to low (bottom). Note that the eight modes at the bottom, which are the only ones active in the lower half of the trace, are all cycles. Simulation parameters are $\epsilon = 0.5$, $\mu = 1$, $D = 5 \times 10^{-3}$. 88

3-11 The emergence of an activity-driven spectral band gap is exhibited by a simulation on a 14-vertex path with (a) all weights equal to 1 and (b) alternating vertex weights 1 and 5. Modes are ordered by frequency from high (top) to low (bottom). Note that in (b) the central $n = 7$ mode is always active and the low energy states on the right half of the plot are significantly more suppressed than they ever are in (a). The qualitative difference is due to the presence of vertices with unequal weights, not the overall scale of the vertex weights; changing vertex weights uniformly is equivalent to rescaling other parameters. Parameters are $\mu = 1.2$, $D = 5 \times 10^{-3}$, and $\epsilon = 0.5$. Both simulations used the same random seed. 90

4-1 Designing networks from spectra. (a), Schematic of DBG network construction. Given a spectrum of eigenvalues distributed in two (or more) groups, we build a graph with non-negative edge weights that realizes this spectrum exactly (1). Sparsification of this complete DBG network with the Spielman-Srivastava [125] algorithm (2) yields a new network with wider eigenvalue distributions and a smaller gap (3). (b), Example graphs used in applications below: Starting from a DBG graph on 200 vertices with 100 eigenvalues set to i.i.d. $\mathcal{N}(5, 0.25)$ and 99 set to i.i.d. $\mathcal{N}(20, 0.25)$ (left), sparsification with $\epsilon = 0.5$ creates a new graph (top) with the number of edges reduced from 19900 to 3758. As a control, we also compare to a gapless random graph (bottom) with 362 edges and the same weighted vertex degrees as the original DBG graph. (c), The eigenvalues for the graphs in (b). The mode on the complete DBG network with the k-th largest nonzero eigenvalue is supported on the first $k+1$ vertices, counted counterclockwise from the top red vertex, and highly localized on vertex $k+1$, which is colored to match in (b). Grey lines indicate the borders of the unstable region for the Swift-Hohenberg model with the parameters used in Fig. 4-3. (d), Sparsified networks retain a significant gap even for relatively large ϵ. Each point shows the mean number of edges and gap size at fixed ϵ between 1 (left) and 0.01 (right), starting from a graph on 200 vertices designed to have 100× eigenvalue 5 and 99× eigenvalue 20. The solid curve shows the worst-case gap estimate, reduction by a factor $1 - \frac{5}{3}\epsilon$. Sample size is 1000 for $\epsilon \geq 0.1$ and 300 for $\epsilon < 0.1$. Error bars are ± 1 standard deviation; horizontal error bars are smaller than the marker size. 97

4-2 DBG networks lead to staggered synchronization and chimeras. (a-f), In the Kuramoto model with $\alpha = 0$, the complete (first row) and sparsified (second row) graphs synchronize much faster than the random graph (third row). For the complete graph the gap affects the rate of synchronization, with highly-connected vertices synchronizing faster (a), while on the sparsified graph the gap is only visible in the mode basis (e). (g-i), Weak chimera states appear when $\alpha = 1$. Both the complete (g) and sparsified (h) graphs have two dominant groups of phase-locked oscillators, with the complete graph more fully synchronized. Dynamics on the random graph (i) are much less coherent. Solid black lines indicate the predicted approximate frequency difference for a network with two distinct eigenvalues, 5 and 20. (j-l), Order parameter $r = |\sum_j e^{i\theta_j}|$ for the simulations in (g-i) for the strongly-connected vertices (red), weakly-connected vertices (teal), and all vertices (gray). 102

4-3 Generic suppression of pattern formation with a designed discrete band gap. (a), Pattern formation in the Swift-Hohenberg system is completely suppressed by constructing a gap around the range where eigenvalues would be unstable (Fig. 4-1c). (b), On a sparsified graph that has a few eigenvalues just within the unstable region, some modes settle at small nonzero values. (c), On the random graph many more eigenvalues are well within the unstable region and the corresponding modes settle at larger amplitudes. Inset graphs show the final steady state on each graph; the size of vertices corresponds to $|\phi|$. All simulations used identical initial conditions $u_i \sim \mathcal{N}(0, 1)$ and parameters $\alpha = 90$, $D_1 = -20$, $D_2 = 1$. 106

4-4 Controlling pattern formation with a designed discrete band gap. (a) Instead of placing a gap in the spectrum around the unstable pattern-forming range, as in Fig. 4-3, we deliberately place particular eigenvalues in the middle of that range corresponding to eigenvectors localised on a desired pattern. (b) From random initial conditions, the system settles into a state where only the chosen modes have nonnegligible amplitudes. (c–e) Time series of pattern evolution on a designed network, with vertices colored according to the stability of the mode localized there as in (a). The size of the vertices indicates $|\phi|$. (c) The encoded pattern is not obvious from either the designed network or the random initial conditions. (d) By time $t = 0.07$ the stable modes have nearly all vanished. (e) The steady state reveals the eigenmode-designed pattern. Because the modes are highly localized, selecting a set of modes to activate is approximately equivalent to selecting a set of vertices to activate. Thus we can encode an arbitrary pattern as the steady state. Depending on initial conditions, the system may settle into other stable states with slight variations in the vertex activations; the pattern is always identifiable and often as clear as shown. The parameters $\alpha = 90$, $D_1 = -20$, and $D_2 = 1$ are identical to those in Fig. 4-3; the tuning parameters to control pattern formation are only the network edge weights. 108

4-5 Localization on a DBG quantum network. (a-c), When the wavefunction in the Gross-Pitaevskii model of Eq. (4.20) is initialized at a weakly connected vertex with low kinetic energy, localization or delocalization (indicated by high or low potential energy, respectively) is controlled by the interplay between the graph spectrum and the rate of potential energy loss g. The random graph (purple) always delocalizes, due to its dense spectrum. However, while the sparsified graph (yellow) can delocalize for low g (a) and high g (c), again due to available eigenmodes, intermediate g (b) places the range of allowed modes inside the spectral gap, preventing delocalization. The complete graph (blue) always inhibits spreading due to the extreme localization of its eigenvectors. 111

4-6 Designed spectra on a discrete network are preserved when extended periodically in one dimension. (a) We extend a finite network to an infinite one by rewiring a subset of the edges to cross between adjacent copies of the original network. Here, we take the network with the spectrum in (b) and rewired the edge between vertices j and k if $|k - j| > n/2$. This rewires roughly one quarter of the edges. (b) One unit cell in (a) would have a discrete spectrum with $\lambda_j = 21 - j$. (c) Most of the eigenvalue bands do not change significantly with q, so the density of states consists of 21 sharp peaks with low- or zero-density regions between. (d) The same construction as in (a) can be repeated for any spectrum; this is the result for a gapped network. (e) One unit cell in (d) would have a gapped spectrum, with 10 eigenvalues equal to 20 and 10 equal to 5, in addition to the always-present zero eigenvalue. (f) Again, most of the eigenvalue bands are roughly constant, even though the eigenvectors do depend strongly on q. The gap in the middle of the spectrum is nearly perfectly preserved; a small gap remains between the bottom two bands. Note the log scale on both density of states plots. 113

Chapter 1

Introduction

This thesis will explore two related topics in network theory. For the first two chapters, we will study active flows, investigating the nonequilibrium mode selection principles [43, 45] governing their dynamics in the network setting. The tools from the active flow chapters are in fact of much more general interest. In particular, one mathematical object called the *graph Laplacian* plays a critical role in problems across mathematics and physics. Motivated by this broad relevance, we will show in the last chapter how to construct networks with exactly specified Laplacian spectra.

1.1 Active flows

Classical fluid dynamics deals with externally-imposed driving forces such as gravity or applied pressure gradients. These passive fluids dissipate energy through viscosity, but do not generate it. Biological systems may act very differently, producing energy at a very small scale, perhaps individual swimming bacteria, and propagating the energy upwards to drive larger flows. Often, the flows occur within an intricate network structure (Fig. 1-1). These biological flow networks, such as capillaries [51], leaf veins [67], and slime molds [2], use an evolved topology or active remodeling to achieve near-optimal transport when diffusion is ineffectual or inappropriate [10, 39, 67, 95, 131].

Even in the absence of explicit matter flux, living systems often involve flow of

information currents along physical or virtual links between interacting nodes, as in neural networks [31], biochemical interactions [65], epidemics [103], and traffic flow [50]. The ability to vary the flow topology gives network-based dynamics a rich phenomenology distinct from that of equivalent continuum models [96]. Identical local rules can invoke dramatically different global dynamical behaviors when node connectivities change from nearest-neighbor interactions to the broad distributions seen in many networks [1, 12, 21, 141]. Certain classes of interacting networks are now sufficiently well understood to be able to exploit their topology for the control of input–output relations [90, 97], as exemplified by microfluidic logic gates [104, 109]. However, when matter or information flow through a noisy network is not merely passive but actively driven by non-equilibrium constituents [2], as in maze-solving slime molds [95], there are no overarching dynamical self-organization principles known. In such an *active network*, noise and flow may conspire to produce behavior radically different from that of a classical forced network. This raises the general question of how path selection and flow statistics in an active flow network depend on its interaction topology.

Flow networks can be viewed as approximations of a complex physical environment, using nodes and links to model intricate geometric constraints [41, 42, 148]. These constraints can profoundly affect matter transport [17, 47, 63, 92], particularly for active systems [44, 85, 137] where geometric confinement can enforce highly ordered collective dynamics [24, 30, 48, 80, 102, 104, 110, 132, 144, 146, 150]. In symmetric geometries like discs and channels, active flows can often be effectively captured by a single variable $\phi(t)$, such as angular velocity [143, 144] or net flux [150], that tends to adopt one of two preferred states $\pm\phi_0$. External or intrinsic fluctuations can cause $\phi(t)$ to diffuse in the vicinity of, say, $-\phi_0$ and may occasionally trigger a fast transition to ϕ_0 and *vice versa* [143, 150]. Geometrically coupling together many such confined units then results in a lattice field theory, reducing a non-equilibrium active medium to a discrete set of variables obeying pseudo-equilibrium physics, as was recently demonstrated for a lattice of bacterial vortices [143].

In Chapter 2, we develop this idea by constructing a generic lattice field model for

an incompressible active medium flowing in an arbitrary network of narrow channels. By connecting concepts from lattice field theory, graph theory, and transition rate theory we can understand how topology controls dynamics for this actively driven network flow. Our combined theoretical and numerical analysis identifies symmetry-based rules that make it possible to classify and predict the selection statistics of complex flow cycles from the network topology. The conceptual framework developed is applicable to a broad class of non-biological far-from-equilibrium networks, including actively controlled information flows, and establishes a new correspondence between active flow networks and generalized ice-type models. The content of chapter 2 was published in the *Proceedings of the National Academy of Sciences* [145].

In Chapter 3, we extend to the compressible case where variations in local density or volume are dynamically relevant. Using perturbation theory, we systematically predict the stationary states of noisy networks and find good agreement with a Bayesian state estimation based on a hidden Markov model applied to simulated time series data. Our results suggest that the macroscopic response of active network structures, from actomyosin force networks to cytoplasmic flows, can be dominated by a significantly reduced number of modes, in contrast to energy equipartition in thermal equilibrium. The model is also well-suited to study topological sound modes and spectral band gaps in active matter. This work appeared in *Physical Review Letters* [46].

1.2 Graph Laplacians

Complex real-world phenomena across a wide range of scales, from aviation [25] and internet traffic [151] to electronic [36] and gene regulatory [83] circuits, can be efficiently described through active and passive network models encoded with weighted graphs. Their dynamics are often essentially determined by the associated graph Laplacian, which we introduce here. A weighted simple graph G is defined by its vertex set $\mathcal{V}$, edge set $\mathcal{E}$ containing unordered pairs of distinct vertices (u, v), and corresponding edge weights w_{uv}. We consider the case with real, nonnegative weights

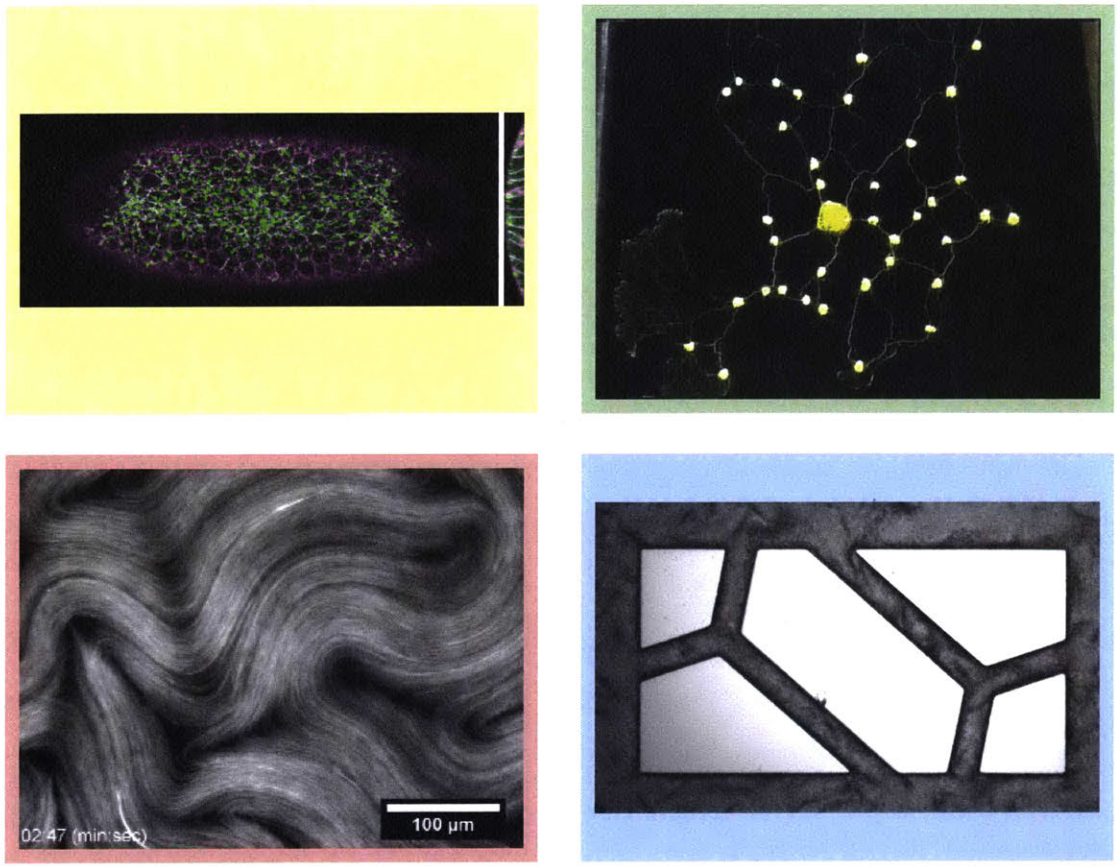

Figure 1-1: Active driving interacts with networks in diverse biological systems. (a) In Drosophila embryos, networks of ATP-driven myosin motors (fluorescently labeled in green) couple to the cell boundaries (magenta) to control tissue folding [33]. (b) The slime mold *Physarum polycephalum* (yellow) can form complex optimized transport networks to connect food sources like the oat flakes (white dots) shown. Here, the food was placed in roughly the pattern of population centers around Tokyo. The organism's final state is reminiscent of the human-designed rail system [131]. (c) Microtubules and kinesin motors like these from the Dogic lab can be confined to channels where they drive coherent shape-dependent flows [147]. (d) Our theoretical work models most closely confined suspensions of swimming microbes. In this picture, from preliminary experiments by the Kantsler lab, sperm cells are confined to a network of channels in a microfluidic chamber with barriers (light gray polygons).

$w_{uv} \geq 0$ and set $w_{uv} = 0$ if there is no edge between u and v. The Laplacian of G is the matrix whose off-diagonal elements are the negatives of the edge weights and whose diagonal elements are the weighted vertex degrees. That is, $L_{uv} = -w_{uv}$ for $u \neq v$ and $L_{uu} = \sum_{v \neq u} w_{uv}$.

The Laplacian matrix occurs naturally in a wide range of physical systems. Up to a sign, it is the discrete analog of the continuous Laplacian: where ∇^2 appears in continuous models, $-L$ typically appears in the discrete version of the model. For example, the ubiquitous nearest-neighbour finite difference approximation to ∇^2 arises as the graph Laplacian of a square lattice [62]. In Chapters 2 and 3 we will work with the discrete gradient operator ∇_{ve}, which with weighted edges equals $-\sqrt{w_{uv}}$ if there is an edge from u to v, $\sqrt{w_{uv}}$ if there is an edge from v to u, and zero otherwise. For any arbitrary orientation of G, the Laplacian is equal to the gradient times its transpose: $L_{uv} = \sum_e \nabla_{ue} \nabla_{ev}^\top$. The singular value decomposition of ∇_{uv}, which will feature prominently in Chapter 3, is then the eigendecomposition of L.

The simplest physical examples of network Laplacians come from spring systems and discrete random walks. If a set of identical masses moving in one dimension are coupled by springs with stiffness w_{uv} between masses u and u, the force on mass u is exactly $-\sum_v L_{uv} x_v = \sum_v w_{uv}(x_v - x_u)$. Here x_u is the coordinate of the uth mass. The mechanics then decouple into $n = |\mathcal{V}|$ oscillation modes corresponding to the eigenvectors of L, with the eigenvalues as squared frequencies.

Similarly, if a particle follows a random walk on a network, traveling from node u to node v with rate w_{uv} (so the probability flow from u to v is the probability p_u of being in state u times the rate), then the probability distribution evolves in time according to

$$\frac{dp_u}{dt} = -\sum_{v \neq u} w_{uv} p_u + \sum_{v \neq u} w_{uv} p_v = -\sum_v L_{uv} p_v. \tag{1.1}$$

The solution again comes from the eigendecomposition of L: the eigenvalues determine the diffusion rate and the rate of decay to the stationary distribution.

It is natural, then, to ask whether we can control these eigenvalues. By designing the network appropriately, what spectra can we construct? There are two clear

constraints. First, the rows and columns of L sum to zero, implying that $\mathbf{1}$, the vector of all ones, is an eigenvector with eigenvalue zero. This eigenvector corresponds to the stationary distribution for the random walk, rigid translation for the spring system, and a constant pressure shift for flow networks. Moreover, the remaining eigenvalues must be nonnegative by the Gershgorin circle theorem [27]. We will see in Chapter 4 that these are the only two restrictions for weighted networks, and that by explicitly constructing networks to have particular spectra we can control a wide variety of classic physical models, including Kuramoto-type coupled oscillators, Swift-Hohenberg pattern formation, and quantum Gross-Pitaevskii dynamics.

Chapter 2

Incompressible flow networks

In this chapter we introduce the active network model in the incompressible setting.[1] Combining concepts from transition rate theory and graph theory, we show how the competition among incompressibility, noise, and spontaneous flow can trigger stochastic switching between states comprising cycles of flowing edges separated by acyclic sets of non-flowing edges. As a main result, we find that the state transition rates for individual edges can be related to one another via the cycle structure of the underlying network, yielding a topological heuristic for predicting these rates in arbitrary networks. We conclude by establishing a mapping between incompressible active flow networks and generalized ice-type or loop models [14, 16, 72].

2.1 Model

2.1.1 Lattice ϕ^6 field theory for active flow networks

Our network is a set of vertices $v \in \mathcal{V}$ connected by edges $e \in \mathcal{E}$, forming an undirected loop-free graph G. (We use graph theoretic terminology throughout, where a loop is a single self-adjacent edge and a cycle is a closed vertex-disjoint walk.) To describe signed flux, we construct the directed graph $\hat{G}$ by assigning an arbitrary orientation

[1] This work was published in the following paper:
Francis G. Woodhouse, Aden Forrow, Joanna B. Fawcett, and Jörn Dunkel. Stochastic cycle selection in active flow networks *Proc. Natl. Acad. Sci. U.S.A.*, 113(29):8200–8205, 2016.

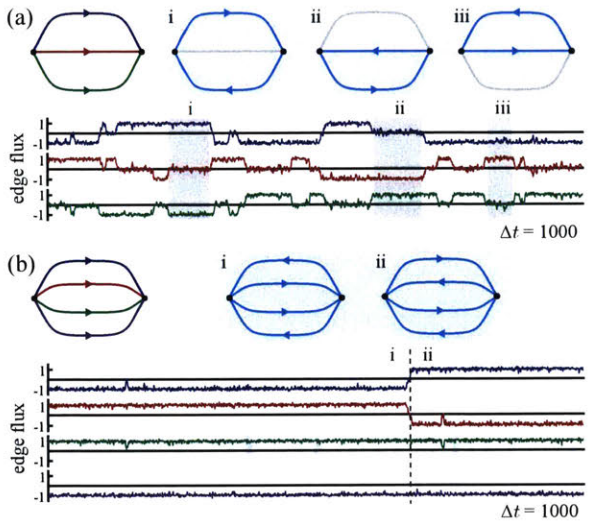

Figure 2-1: Stochastic cycle selection in two elementary graphs. (a) Flux–time traces from Eq. 2.4 for each of the three edges in the graph shown, signed according to the edges' arrows, with three different temporary configurations highlighted as indicated by (i)–(iii). $\lambda = 2.5$, $\mu = 25$, $\beta^{-1} = 0.05$. (b) Same as (a), but with an additional edge in the graph. States are more stable with even-degree vertices, since flux conserving flows are possible with all edges flowing.

to each edge. Now, let ϕ_e be the flux along edge e, where $\phi_e > 0$ denotes flow in the direction of the orientation of e in $\hat{G}$ and $\phi_e < 0$ denotes the opposite. To model typical active matter behavior [80, 143, 144, 146], we assume that fluxes either spontaneously polarize into flow states $\phi_e \approx \pm 1$ or adopt some other non-flowing mode $\phi_e \approx 0$. We formalize this by imposing a bistable potential $V(\phi_e)$ on each flux variable. The typical symmetric, bistable potential is the quartic $V_4(\phi) = -\frac{1}{2}\phi^2 + \frac{1}{4}\phi^4$. However, we use the sixth-order form $V(\phi) = V_6(\phi) = -\frac{1}{4}\phi^4 + \frac{1}{6}\phi^6$. This form, of higher order than in a typical Landau theory, ensures that incompressible potential minima are polarized flows with every ϕ_e in the set $\{-1, 0, +1\}$, rather than the continuum of fractional flow states that a typical ϕ^4 potential would yield.

Incompressibility, appropriate to dense bacterial suspensions or active liquid crystals, is imposed as follows. The net flux into vertex v is $\sum_{e \in \mathcal{E}} \nabla_{ve} \phi_e$, where the discrete negative gradient operator $\nabla = (\nabla_{ve})$ is the $|\mathcal{V}| \times |\mathcal{E}|$ incidence matrix of $\hat{G}$ such that ∇_{ve} is -1 if e is directed out of v, $+1$ if e is directed into v, and 0 if e is not incident to v [53]. Exact incompressibility corresponds to the constraint $\nabla\Phi = 0$ on

the global flow configuration $\Phi = (\phi_e) \in \mathbb{R}^{|\mathcal{E}|}$. To allow for small fluctuations, modeling variability in the microscopic flow structure, we apply this as a soft constraint via an interaction potential $\propto |\nabla\Phi|^2$. The total energy $H(\Phi)$ of the active flow network then reads

$$H(\Phi) = \lambda \sum_{e\in\mathcal{E}} V(\phi_e) + \tfrac{1}{2}\mu|\nabla\Phi|^2, \tag{2.1}$$

with coupling constants λ and μ.

To see why $V_4(\phi)$ has the undesirable symmetry mentioned above, consider the elementary (though not simple!) two-vertex, three-edge graph in Fig. 2-1a. Here the energy is

$$H(\phi_1, \phi_2, \phi_3) = \lambda[V(\phi_1) + V(\phi_2) + V(\phi_3)] + \mu(\phi_1 + \phi_2 + \phi_3)^2.$$

In the limit $\mu/\lambda \gg 1$, the flow is incompressible, so we can substitute $\phi_3 = -\phi_1 - \phi_2$ to obtain a reduced energy $\hat{H}(\phi_1, \phi_2) = \lambda\mathcal{H}(\phi_1, \phi_2)$, where, assuming a symmetric potential $V(\phi)$,

$$\mathcal{H}(\phi_1, \phi_2) = V(\phi_1) + V(\phi_2) + V(\phi_1 + \phi_2).$$

Local minima of $\mathcal{H}$ then yield metastable states of the system, independent of λ.

Consider the case $V = V_4$. Then $\mathcal{H}$ factorizes as

$$\mathcal{H} = \tfrac{1}{2}f(\phi_1, \phi_2)[f(\phi_1, \phi_2) - 2],$$

where $f(\phi_1, \phi_2) = \phi_1^2 + \phi_1\phi_2 + \phi_2^2$. Thus $\boldsymbol{\nabla}\mathcal{H} = 0$ implies $(f-1)\boldsymbol{\nabla}f = 0$, so either $f = 1$ or $\phi_1 = \phi_2 = 0$. The latter is a local maximum, so our minima are the solutions of $\phi_1^2 + \phi_1\phi_2 + \phi_2^2 = 1$. But these solutions form an ellipse in the (ϕ_1, ϕ_2) plane, implying a *continuous* U(1)-symmetric set of fixed points. In other words, with $V = V_4$, mixed states such as $(\frac{1}{\sqrt{3}}, \frac{1}{\sqrt{3}}, -\frac{2}{\sqrt{3}})$ are equally preferable to unit-flux states like $(1, 0, -1)$. In contrast, the choice $V = V_6$ results in minima of $\mathcal{H}$ only at

the six states $(\phi_1, \phi_2) = (\pm 1, 0), (0, \pm 1), (\pm 1, \mp 1)$, which is the phenomenology we are interested in. Based on simulations, these results carry over to more complicated networks, though we do not prove so here; V_4 typically allows mixed states while V_6 selects unit fluxes.

The energy in Eq. (2.1) is comparable to that of a lattice spin field theory, but with interactions given by higher-dimensional quadratic forms akin to a spin theory on the vertices of a hypergraph. Suppose we switch to a typical vertex-based picture, where fluxes ϕ_e on edges e in G are now spins ψ_i on vertices i in an interaction graph Ξ. A scalar lattice spin theory then has Hamiltonian

$$H_{\text{spin}} = \lambda \sum_i V(\psi_i) + \tfrac{1}{2}\mu \sum_{\{i,j\}} (\psi_i \pm_{ij} \psi_j)^2, \tag{2.2}$$

where in the sum over adjacent spins $\{i, j\}$ in Ξ, the sign $\pm_{ij}$ is $+$ or $-$ according to whether the interaction between i and j is antiferromagnetic or ferromagnetic, respectively. In our theory, however, multiple spins are permitted inside each interaction term according to the degree of each vertex in G. For instance, on a cubic graph, the energy (2.1) is equivalent to

$$H = \lambda \sum_i V(\psi_i) + \tfrac{1}{2}\mu \sum_{\{i,j,k\}} (\psi_i \pm_{ij} \psi_j \pm_{jk} \psi_k)^2, \tag{2.3}$$

where the interaction is now a sum over interacting *triples* of spins, one term for each vertex in G, with pairwise signs being $-$ or $+$ according to whether the corresponding edges in $\hat{G}$ are oriented head-to-tail or not at the vertex. Thus we have essentially defined a theory on an interaction *hypergraph* Ξ, with Eq. (2.2) being the special case where Ξ is a graph: while Eq. (2.2) has two types of interaction edge—antiferro- and ferromagnetic—between two spins, the general theory has 2^{n-1} types of interaction hyperedge between n spins for all $n \geqslant 1$.

2.1.2 Network dynamics

Appealing to recent results showing that bacterial vortex lattices obey equilibrium-like physics [143], we impose that Φ obeys the overdamped Langevin equation

$$d\Phi = -\frac{\delta H}{\delta \Phi} dt + \sqrt{2\beta^{-1}} d\mathbf{W}_t, \tag{2.4}$$

with $\mathbf{W}_t$ an $|\mathcal{E}|$-dimensional vector of uncorrelated Wiener processes and β the inverse temperature. We choose additive noise for mathematical simplicity and because we focus on the effect of the active driving; plausibly, more detailed physical modeling could lead to a different stochastic term potentially depending on Φ. This would change the quantitative results of this chapter and Chapter 3, for example the calculation of transition rates, but broad qualitative features like the selection of stable flow states will remain.

The stochastic dynamical system in Eq. (2.4) has a Boltzmann stationary distribution $\propto e^{-\beta H}$. The components of the energy gradient $\delta H/\delta\Phi$ in Eq. (2.4) are

$$\left(\frac{\delta H}{\delta \Phi}\right)_e = -\lambda \phi_e^3 (1 - \phi_e^2) + \mu (\nabla^\top \nabla \Phi)_e. \tag{2.5}$$

$\nabla^\top \nabla$ is the discrete Laplacian operator on edges, which is of opposite sign to the continuous Laplacian ∇^2 by convention. Remember that the vertex Laplacian defined in Chapter 1 is equal to $\nabla \nabla^\top$; the edge Laplacian is a related but distinct operator. The last term in Eq. (2.5) arises in an otherwise equivalent fashion to how a bending energy $|\boldsymbol{\nabla} \psi|^2$ yields a diffusive term $\nabla^2 \psi$ in a continuous field theory. On its own, this term damps non-cyclic components of the flow while leaving cyclic components untouched; these components' amplitudes would then undergo independent Brownian walks were they not constrained by the ϕ^6 component of V. This process results in a long-term state dominated by a weighted sum of cycles of the graph, as we now describe.

As in the derivation of the incompressible limit (see section 2.3.1 below), by analogy with a spectral decomposition for the diffusion equation, we decompose Φ into a

sum $\Phi = f_j \Psi^j$ over an orthonormal eigenbasis Ψ^j of the edge Laplacian $\nabla^\top \nabla$, where $\Psi^j = (\psi_e^j)$ has eigenvalue $\nu_j \geqslant 0$. If λ is set to zero, the components f_i then obey

$$df_i = -\mu \nu_i f_i dt + \sqrt{2\beta^{-1}} dW_{i,t},$$

after combining independent noise terms. Thus modes with $\nu_i > 0$ are damped by the diffusivity μ while modes with $\nu_i = 0$ are only subject to noise-induced fluctuations. The non-zero modes' amplitudes follow Ornstein–Uhlenbeck processes and therefore have mean zero and variance $(\beta \mu \nu_i)^{-1}$ as $t \to \infty$, whereas, because of the absence of damping, the zero modes' amplitudes follow simple Brownian processes and so have variance $2\beta^{-1}t$.

With these dynamics for any λ, all loops in G, i.e., edges of the form (w, w) from one vertex to itself, will decouple from the dynamics of the rest of G. Consider a loop edge $\ell \in \mathcal{E}$ incident to a vertex $w \in \mathcal{V}$. Then ∇ is defined such that $\nabla_{w\ell} = 0$ (consistent with ϕ_ℓ contributing zero to the net flux at w, since flow in along ℓ always equals flow out along ℓ). Therefore, using summation convention, $\nabla_{ve}\phi_e$ is independent of ϕ_ℓ for all $v \in \mathcal{V}$, which implies $\partial H / \partial \phi_e$ is independent of ϕ_ℓ for all $e \neq \ell$ and thus ϕ_ℓ decouples. Furthermore, $(\nabla^\top \nabla \Phi)_\ell = \nabla_{v\ell} \nabla_{ve} \phi_e = 0$, so $d\phi_\ell = -\lambda V'(\phi_\ell) dt + \sqrt{2\beta^{-1}} dW_{\ell,t}$, meaning ϕ_ℓ behaves as a non-interacting Brownian particle in the potential $V(\phi_\ell)$. The remaining non-loop edges follow Eq. (2.4) exactly as they would on the subgraph of G with all loops removed.

Altogether, the preceding paragraphs mean that the interesting behavior is confined to flows around interacting cycles. We now characterize the behavior of this model on a variety of forms of underlying graph G. For clarity, in addition to our prior assumption that G is loop-free (which simplifies definitions and is unimportant dynamically since loops decouple), we will focus on connected, simple graphs G, though multiple edges are not excluded *per se* (Fig. 2-1). In what follows, we work in the near-incompressible regime $\mu \gg \lambda$ before discussing the strictly incompressible limit $\mu \to \infty$ below.

2.2 Results

2.2.1 Stochastic cycle selection

The combination of energy minimization and noise leads to *stochastic cycle selection.* A local energy minimum comprises a maximal edge-disjoint union of unit-flux cycles: edge fluxes seek to be at ± 1 if possible subject to there being zero net flux at every vertex, leading to states where the non-flowing edges contain no cycles (that is, they form a *forest*, or a union of trees). However, noise renders these states only metastable and induces random switches between them. Figure 2-2a–f depicts flow on the 4-vertex complete graph K_4 (Fig. 2-2a–c) and the generalized Petersen graph $P_{3,1}$ (Fig. 2-2d–f)—the tetrahedron and triangular prism, respectively—where we have integrated Eq. (2.4) to yield flux–time traces of each edge. The coordinated switching of edges between states of mean flux at -1, 0 and $+1$ leads to random transitions between cyclic states, as illustrated. Note that the more flowing edges a state has, the lower its energy and therefore the longer-lived that state will be; thus in K_4, for example, 4-cycles, which are global minima, persist longer than 3-cycles (Fig. 2-2b,c).

A graph possessing an Eulerian cycle—a non-repeating tour of all edges starting and ending at one vertex, which exists if and only if all vertices are of even degree—has global energy minima with all edges flowing. By contrast, a graph possessing many vertices of odd degree will have minimum energy states with non-flowing edges, because edges flowing into and out of such a vertex pair up to leave an odd number of 0-flow edges. Such 'odd' networks are particularly interesting dynamically as they are more susceptible to noise-induced state switches than graphs with even degree vertices. This susceptibility is exemplified by the small graphs in Fig. 2-1, where adding an extra edge markedly slows transition rates. For the graph in Fig. 2-1a to change state while conserving flux, one edge changes from $+1$ (or -1) to 0 while another simultaneously goes from 0 to -1 (or $+1$), which has an energy barrier $11\lambda/192$. However, for the graph in Fig. 2-1b, one edge changes from $+1$ to -1 while another goes from -1 to $+1$, with an energy barrier $\lambda/6$ nearly three times that of graph (a). For this reason, from now on we restrict our attention to *cubic* or *3-regular*

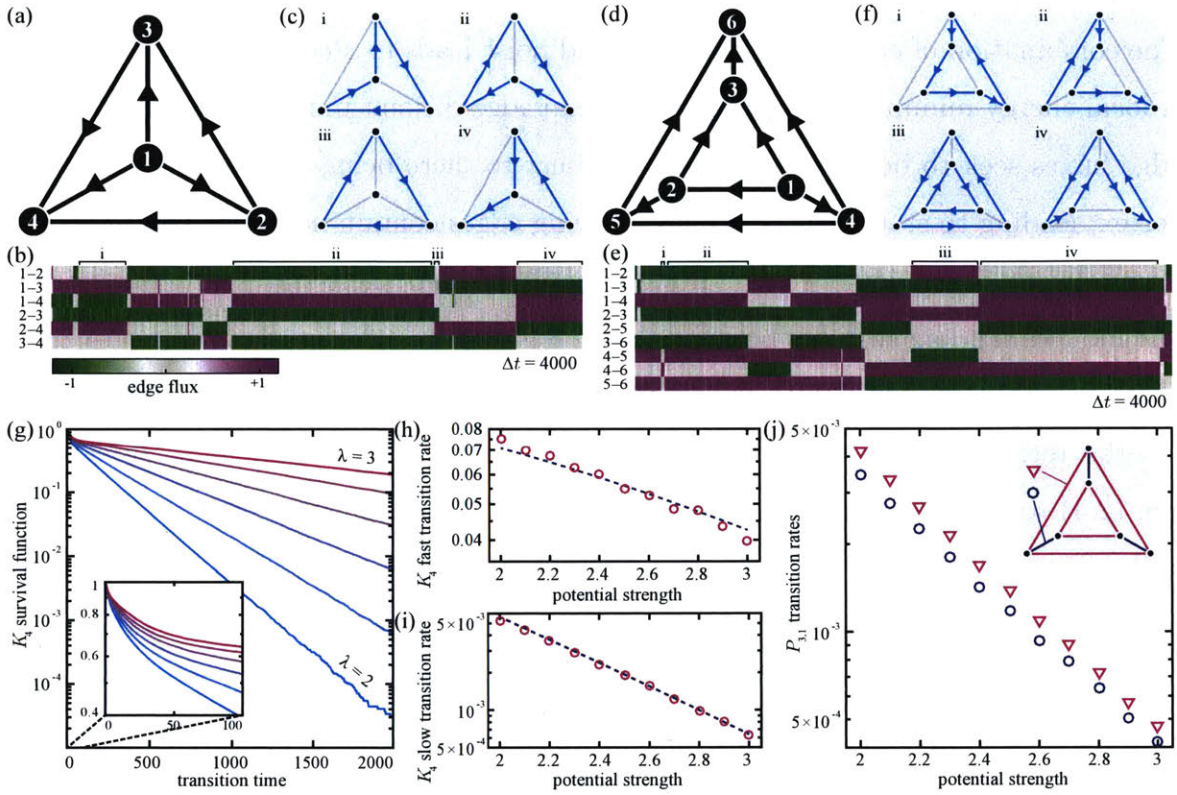

Figure 2-2: Noise and activity cause stochastic cycle selection. (a–c) Flux–time traces (b) for each edge of the complete graph on four vertices, K_4. Edge orientations are as in (a). The sub-diagrams in (c)(i–iv) exemplify the flow state in the corresponding regions of the trace. Parameters $\lambda = 2.5$, $\mu = 25$, $\beta^{-1} = 0.05$. (d–f) As in (a–c), but for the generalized Petersen graph $P_{3,1}$. The same switching behavior results, but now with more cycle states. (g) Survival function $S(t) = \mathbb{P}(T > t)$ of the transition waiting time T for an edge in K_4, at regularly-spaced values of λ in $2 \leqslant \lambda \leqslant 3$ with $\mu = 25$, $\beta^{-1} = 0.05$. Log-scaled vertical; straight lines imply an exponential distribution at large t. Inset: $S(t)$ at small t with log-scaled vertical, showing non-exponential behavior. (h,i) Slow and fast edge transition rates in K_4, with parameters as in (g). Circles are from fitting T to a mixture of two exponential distributions, lines show best-fit theoretical rates $k \propto \lambda \exp(-\beta \Delta H)$ with ΔH calculated for transitions between 3- and 4-cycles. (j) Transition rate $k = \langle T \rangle^{-1}$ for each set of equivalent edges in $P_{3,1}$, as per the key, as a function of λ, with $\mu = 25$, $\beta^{-1} = 0.05$. Log-scaled vertical shows exponential dependence on λ.

graphs where all vertices have degree three.

2.2.2 Waiting times and graph symmetries

The cycle-swapping behavior can be quantified by the distribution of the waiting time for an edge to transition between states in $\{-1, 0, 1\}$. For some edges, dependent on G, this distribution will be identical: the interactions in the energy (2.1) are purely topological, with no reference to an embedding of G, implying that only topological properties—in particular, graph symmetries—can influence the dynamics. Symmetries of a graph G are encoded in its automorphism group $\mathrm{Aut}(G)$, whose elements permute vertices and edges while preserving incidence and non-incidence [53]. We will now show that two edges will follow identical state distributions if (but not only if) one can be mapped to the other by some element of $\mathrm{Aut}(G)$; this determines an equivalence relation on $\mathcal{E}$. Here, for clarity, we do not use summation convention.

To permit multiple edges, we define an automorphism $\sigma \in \mathrm{Aut}(G)$ as a permutation of $\mathcal{V} \cup \mathcal{E}$ preserving $\mathcal{V}$ and $\mathcal{E}$ such that $v \in \mathcal{V}$ and $e \in \mathcal{E}$ are incident if and only if $\sigma(v)$ and $\sigma(e)$ are incident. Suppose we have flow Φ on $\hat{G}$ obeying Eq. 2.4, whose components read

$$d\phi_e = -\lambda V'(\phi_e)dt - \mu \sum_{v\in\mathcal{V}} \sum_{f\in\mathcal{E}} \nabla_{ve}\nabla_{vf}\phi_f dt + \sqrt{2\beta^{-1}}dW_{e,t}. \tag{2.6}$$

Let $\Phi^\sigma = (\phi_e^\sigma)$ be the flow vector after permuting by σ, so that $\phi_e^\sigma = \phi_{\sigma(e)}$. Replacing e with $\sigma(e)$ in Eq. (2.6) and substituting this definition implies

$$d\phi_e^\sigma = -\lambda V'(\phi_e^\sigma)dt - \mu \sum_{v\in\mathcal{V}} \sum_{f\in\mathcal{E}} \nabla_{v\sigma(e)}\nabla_{vf}\phi_f dt + \sqrt{2\beta^{-1}}dW_{\sigma(e),t}. \tag{2.7}$$

Since σ is a permutation, we can reorder the sums as

$$\sum_{v\in\mathcal{V}} \sum_{f\in\mathcal{E}} \nabla_{v\sigma(e)}\nabla_{vf}\phi_f = \sum_{v\in\mathcal{V}} \sum_{f\in\mathcal{E}} \nabla_{\sigma(v)\sigma(e)}\nabla_{\sigma(v)\sigma(f)}\phi_{\sigma(f)}.$$

Furthermore, since σ preserves incidence but not necessarily orientation, $\nabla_{\sigma(v)\sigma(e)} =$

$s_e \nabla_{ve}$ where $s_e = \pm 1$ according to whether the orientation of $\sigma(e)$ with respect to $\sigma(v)$ is the same as or opposite to the orientation of e with respect to v. Therefore, Eq. (2.7) becomes

$$d\phi_e^\sigma = -\lambda V'(\phi_e^\sigma)dt - \mu s_e \sum_{v\in\mathcal{V}} \sum_{f\in\mathcal{E}} \nabla_{ve}\nabla_{vf} s_f \phi_f^\sigma dt + \sqrt{2\beta^{-1}} dW_{\sigma(e),t}. \tag{2.8}$$

Let $\tilde{\Phi}^\sigma = (\tilde{\phi}_e^\sigma)$ be the flow with components $\tilde{\phi}_e^\sigma = s_e \phi_e^\sigma$. Multiplying Eq. (2.8) by s_e and using $s_e V'(\phi) = V'(s_e \phi)$ gives

$$d\tilde{\phi}_e^\sigma = -\lambda V'(\tilde{\phi}_e^\sigma)dt - \mu \sum_{v\in\mathcal{V}} \sum_{f\in\mathcal{E}} \nabla_{ve}\nabla_{vf} \tilde{\phi}_f^\sigma dt + \sqrt{2\beta^{-1}} dW_{\sigma(e),t},$$

where we have also used $d\mathbf{W}_t = -d\mathbf{W}_t$ by symmetry of the process $\mathbf{W}$. In other words, $\tilde{\Phi}^\sigma$ and Φ obey identical stochastic differential equations, meaning that $s_e\phi_e^\sigma$ and ϕ_e obey identical waiting time distributions. But ϕ_e^σ and $-\phi_e^\sigma$ also obey identical waiting time distributions, because for every state Φ_0, there is an identical probability state $-\Phi_0$ by symmetry of H. Therefore, any edges e_1 and e_2 for which there exists $\sigma \in \mathrm{Aut}(G)$ with $e_2 = \sigma(e_1)$ will have identical waiting time distributions.

Note that in the incompressible limit $\mu \to \infty$, there may also be pairs of edges with identical waiting time distributions for which no such σ exists, even in connected simple graphs. One way to find examples of this is to construct graphs where (1) every cycle passing through e_1 also passes through e_2 and vice versa and (2) there is no automorphism mapping e_1 to e_2.

In K_4, every vertex is connected to every other, so $\mathrm{Aut}(K_4) = S_4$. This means any edge can be permuted to any other—the graph is *edge transitive*—so all edges are equivalent and may be aggregated together. To quantify cycle swapping in K_4, we numerically determined the distribution of the waiting time for an edge to change its state between -1, 0 and $+1$. The resultant survival function $S(t) = \mathbb{P}(T > t)$ for the transition waiting time T of any edge in K_4 lengthens with increasing flow polarization strength λ (Fig. 2-2g), and is well approximated by a two-part mixture of exponential distributions.

2.2.3 Transition rate estimation

Reaction-rate theory explains the form of the waiting time distribution [59]. In a system such as ours that obeys damped noisy Hamiltonian dynamics, a transition from one local energy minimum to another, respectively Φ_a and Φ_c, will occur along a one-dimensional submanifold crossing a saddle point Φ_b. The waiting time T_{ac} for this transition to occur is then distributed approximately exponentially, with rate constant $k_{ac} = \langle T_{ac} \rangle^{-1}$. For a Hamiltonian that is locally quadratic everywhere, the rate follows from the generalized Arrhenius law [59]

$$k_{ac} \propto \left[-\nu_1^{(b)} \frac{\prod_{i=1}^{N} \nu_i^{(a)}}{\prod_{i=2}^{N} \nu_i^{(b)}} \right]^{1/2} \exp(-\beta \Delta H_{ab}), \tag{2.9}$$

where $\Delta H_{ab} = H(\Phi_b) - H(\Phi_a)$ is the transition energy barrier and $\nu_i^{(a)}$ and $\nu_i^{(b)}$ are the eigenvalues of the Hessian $\delta^2 H / \delta \Phi^2$ with $\nu_1^{(b)} < 0$ the unstable eigenvalue at the saddle point. The reverse transition time T_{ca} obeys another exponential distribution with equivalent rate k_{ca} dependent on the energy barrier ΔH_{cb}. Therefore, the aggregated distribution of the waiting time T for the system to change its state between either minimum is a mixture of two exponential distributions weighted by the equilibrium probabilities of the system to be found in each state. For K_4, almost all transitions should be between 3-cycles and 4-cycles: each Eulerian subgraph is a 3-cycle or a 4-cycle, with 4-cycles being global minima, and direct transitions between different 4-cycles have a large enough energy barrier to be comparatively rare. Thus, we expect K_4 to exhibit a two-part mixture with a slow rate k_{43} from a 4- to a 3-cycle and a fast rate k_{34} from a 3- to a 4-cycle. Figure 2-2h,i shows k_{43} and k_{34} for K_4 at a range of values of λ, as determined by maximum likelihood estimation on simulation data. Our non-quadratic potential means these rates are not precisely determined by Eq. (2.9), but it does suggest an Arrhenius-type dependence $k_{ac} \propto \lambda \exp(-\beta \Delta H_{ab})$. Computing the energy barriers and fitting the proportionality constant for each of k_{34} and k_{43} then gives excellent fits to the data, confirming our hypothesis (Fig. 2-2h,i).

In the limit $\mu/\lambda \gg 1$ the transition energy barriers for K_4 can be computed

directly. We assume incompressibility throughout the transition and enforce that assumption by directly solving the constraints, though using a cycle basis would yield the same result. Using the vertex labelings and edge orientations in Fig. 2-2a, let ϕ_1, ϕ_2 and ϕ_3 be the flows on the outer edges $2 \to 3$, $2 \to 4$, and $3 \to 4$ respectively. Then the flows on the other three edges are fixed by the four vertex constraints (one of which is redundant), giving energy $H(\phi_1, \phi_2, \phi_3) = \lambda \mathcal{H}(\phi_1, \phi_2, \phi_3)$, where

$$\begin{aligned}\mathcal{H}(\phi_1, \phi_2, \phi_3) = V(\phi_1) + V(\phi_2) + V(\phi_3) \\ + V(\phi_1 + \phi_2) + V(\phi_2 + \phi_3) + V(\phi_3 - \phi_1).\end{aligned}$$

Extrema of $\mathcal{H}$ can then be evaluated numerically. By symmetry we need only consider one particular transition. Let Φ_a be the state with unit flux on the 3-cycle $1 \to 2 \to 3 \to 1$ where $(\phi_1, \phi_2, \phi_3) = (1, 0, 0)$. Similarly, let Φ_c be the 4-cycle $1 \to 2 \to 3 \to 4 \to 1$ where $(\phi_1, \phi_2, \phi_3) = (1, 0, 1)$. These states are separated by a saddle point Φ_b with $(\phi_1, \phi_2, \phi_3) \approx (1.03, 0, 0.44)$, where $\mathcal{H}(\Phi_b) \approx -0.20$. Since $\mathcal{H}(\Phi_a) = -1/4$ and $\mathcal{H}(\Phi_c) = -1/3$, there are transition energy barriers $\Delta H_{ab} \approx 0.45\lambda$ from a 3- to a 4-cycle and $\Delta H_{cb} \approx 0.54\lambda$ from a 4- to a 3-cycle.

Note that the transition is not exactly of the form $(\phi_1, \phi_2, \phi_3) = (1, 0, s)$ with $0 \leqslant s \leqslant 1$, as it would be were it only adding or removing a unit of flux around a 3-cycle. Instead, the saddle point is slightly displaced from $\phi_1 = 1$. However, this effect is small, and ϕ_2 remains at $\phi_2 = 0$ throughout.

The complete graph K_4 has as much symmetry as is possible on four vertices. This is unusual: most graphs have multiple classes of equivalent edges. Though $P_{3,1}$ (Fig. 2-2d) is vertex transitive, in that any vertex can be permuted to any other by its automorphism group $\mathrm{Aut}(P_{3,1}) = D_6 \times C_2$, it is *not* edge transitive. Instead, the edges split into two equivalence classes (Fig. 2-2j, inset), one containing the two triangles and the other containing the three edges between them. The waiting times then cluster into two distinct distributions according to these two classes. However, when more than two inequivalent minima exist, as they do for $P_{3,1}$, the potential transitions rapidly increase according to the combinatorics of the mutual accessibility between

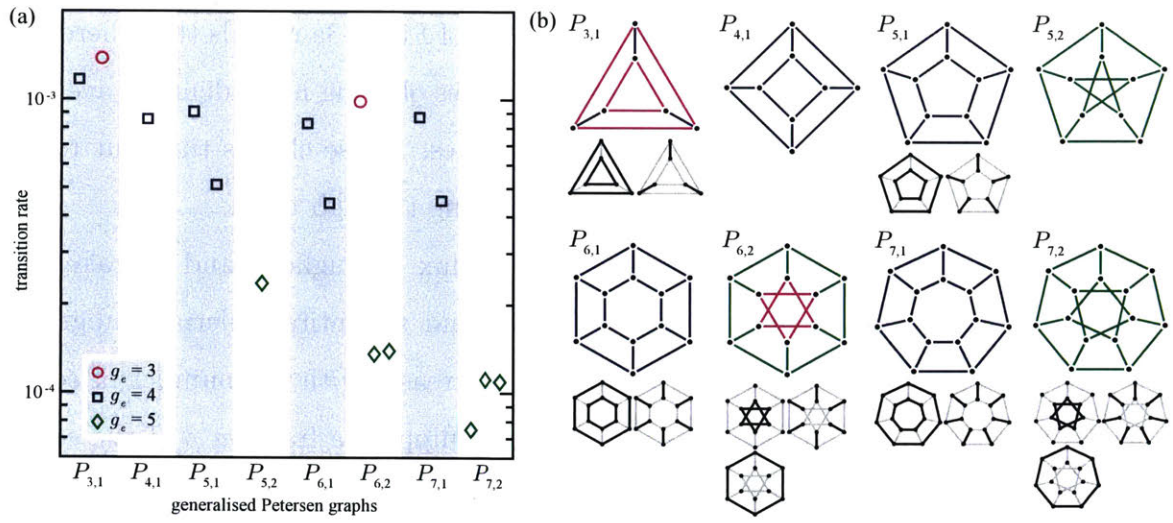

Figure 2-3: Transition rates in highly symmetric graphs are determined by cycle structure. (a) Transition rate for edges in the first eight generalized Petersen graphs with $\lambda = 2.5$, $\mu = 25$, $\beta^{-1} = 0.05$. The rate was determined for each edge, then averaged within classes of equivalent edges. Symbols denote the rate for each class, categorized by e-girth g_e as in the key. The range of computed rates within each class is smaller than the symbols. (b) The graphs in (a) with their edge equivalence classes when more than one exists. Edges colors denote g_e as in (a). Observe that identical e-girth does not imply equivalence of edges.

these minima. On $P_{3,1}$ there is potentially one rate for each pairwise transition between 4-, 5- and 6-cycles, leading to a mixture of six or more exponentials for the waiting time distribution. These mixture components cannot be reliably statistically distinguished without large separations of time scales. Instead, we compute the transition rate $k = \langle T \rangle^{-1}$ for each set of equivalent edges. The rates decay exponentially with λ (Fig. 2-2j), consistent with transitions obeying Eq. (2.9). But why does one set of edges transition more slowly on average than the other? We shall now explore this question for both highly symmetric and totally asymmetric graphs.

2.2.4 Edge girth determines rate band structure

Global symmetries and local graph structure play distinct roles when determining the transition rates. Figure 2-3a shows the edge state transition rates for the first eight generalized Petersen graphs $P_{n,k}$ [140], averaged within edge equivalence classes (Fig. 2-3b), at a representative choice of parameter values which we fix henceforth to

focus on the effects of network topology. Inspection of Fig. 2-3a reveals that there are some graphs, such as $P_{6,2}$, that exhibit distinct classes obeying near-identical average rates, despite these edges' differing global symmetries. These classes turn out to be composed of edges with similar sizes of cycles running through them.

When $\mu \gg \lambda$, state transitions will conserve flux throughout and so take the form of adding or subtracting a unit of flux around an entire Eulerian subgraph $G' \subset G$. The energy barrier to such a transition increases with the number of edges m in G'. Indeed, suppose the transition consists of flipping a fraction ρ of the edges in G' from $\phi = 0$ to $\phi = \pm 1$, with the remaining edges necessarily flipping from $\phi = \pm 1$ to $\phi = 0$. The transition can then be approximated by a one-dimensional reaction coordinate s running from 0 to 1, as follows. Suppose that only edges in G' change during the transition (which is approximately true for K_4; Section 2.2.3). Using the symmetry of V, the energy $H(s)$ at point s of the transition is given by $H(s) = H_0 + \rho m V(s) + (1-\rho) m V(1-s)$ for H_0 a constant dependent on the states of the edges not in G'. The energy barrier is then $\Delta H = \max_s H(s) - H(0)$. H is maximized precisely when $\rho V(s) + (1-\rho) V(1-s)$ is maximized, which is independent of m. Therefore, for fixed ρ, ΔH is linear in m. This argument suggests that, since the transition rate $k \propto \exp(-\beta \Delta H)$, edges contained in small cycles should have exponentially greater transition rates than those with longer minimal cycles. Define the *e-girth* g_e to be the minimum length of all cycles containing edge e, so that the usual graph girth is $\min_e g_e$. Categorizing edge classes in Fig. 2-3 by g_e confirms our hypothesis: the transition rates divide into near-distinct ranges where larger g_e yields rarer transitions, and equivalence classes with similar rates have identical e-girths.

2.2.5 Asymmetric networks

Even for graphs with no symmetry, the behavior of each edge can still be predicted by a simple local heuristic. For our purposes, a graph with 'no symmetry' is one possessing only the identity automorphism, in which case we say it is *asymmetric* [53]. In this case, edges can have transition rates entirely distinct from one another. Figure 2-4a depicts the mean transition rates for the edges of 20 asymmetric bridgeless cubic

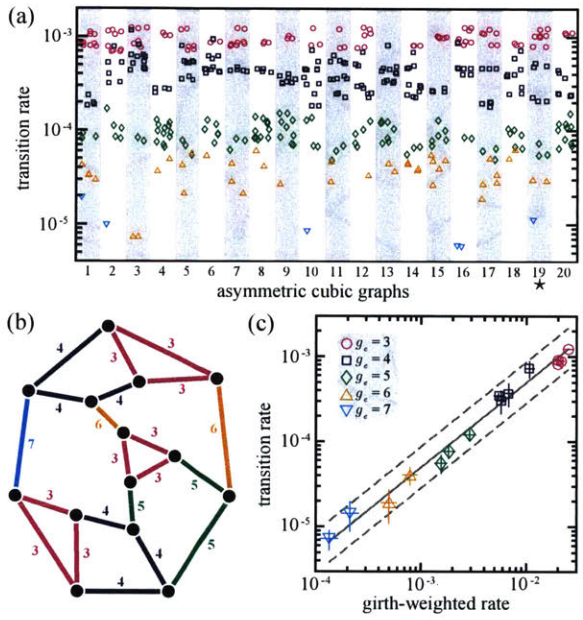

Figure 2-4: Cycle structure determines edge transition rates in asymmetric graphs. (a) Transition rate for each edge in 20 random asymmetric bridgeless cubic graphs on 21 edges. Markers denote e-girth g_e as per the key in (c). $\lambda = 2.5$, $\mu = 25$, $\beta^{-1} = 0.05$. (b) One of the graphs in (a), corresponding to the marked column ($\star$). Edges colored and labelled according to g_e. All 20 graphs are shown in Fig. 2-5. (c) Transition rates k from (a) binned by girth-weighted rate R_g, using best-fit value $\alpha = 1.31$, with markers denoting g_e as per the key. Horizontal error bars are range of marker position over 95% confidence interval in α, vertical error bars are ± 1 standard deviation in k within each group. Solid line is best fit $k = \gamma R_g$, dashed lines are 95% prediction intervals on k with α fixed.

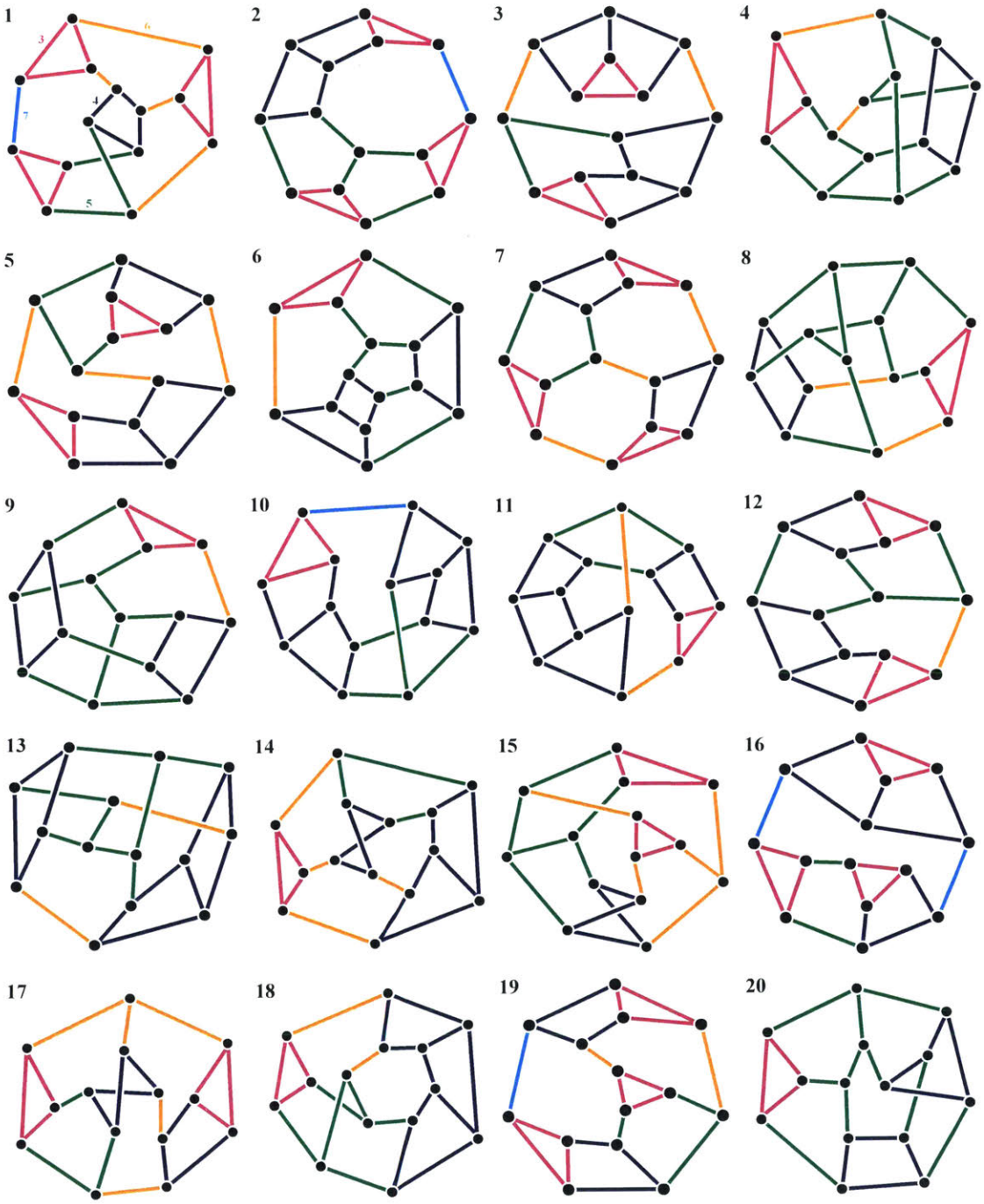

Figure 2-5: The 20 non-isomorphic asymmetric cubic graphs in Fig. 2-4. Edges are colored according to e-girth as indicated in graph 1 and in Fig. 2-4. Graph 19 is that illustrated in Fig. 2-4b. All planar graphs (2, 3, 5, 6, 7, 12, 16 and 19) are shown in a planar embedding.

graphs on 21 edges. As in Fig. 2-3, categorizing edges by their e-girths (illustrated in Fig. 2-4b for the starred graph; see Fig. 2-5 for all 20 graphs) splits the rates into near-distinct bands, despite the total absence of symmetry. However, the bands are not perfectly distinct, and high-girth edges in particular display a range of transition rates both within and across graphs. A large portion of this variation is accounted for by considering the sizes of *all* cycles containing an edge. While the full dependence is highly complex, we can obtain a good transition rate estimate by considering just two cycles. Let $\ell_1 = g_e$ and ℓ_2 be the sizes of the two smallest cycles through e. (It may be that $\ell_1 = \ell_2$.) Drawing on our earlier argument for the transition rate of an m-cycle, suppose that flips of these two cycles occur independently with waiting times T_i distributed exponentially at rates $\Lambda_i = \gamma \exp(-\alpha \ell_i)$ for constants α, γ. The waiting time $T = \min\{T_1, T_2\}$ for one of these to occur is then exponentially distributed with rate $\Lambda_1 + \Lambda_2$. Therefore, $\langle T \rangle = (\Lambda_1 + \Lambda_2)^{-1}$ and so the transition rate $k = 1/\langle T \rangle = \gamma R_g$, where we have defined the *girth-weighted rate*

$$R_g = \exp(-\alpha \ell_1) + \exp(-\alpha \ell_2). \tag{2.10}$$

This could be extended to an arbitrary number of independent cycles, but as the longer cycles are exponentially less likely to transition they have only a small effect. Fitting $k = \gamma R_g$ to the data in Fig. 2-4a yields an exponent $\alpha = 1.31$. This fit gives a strong match to the data (Fig. 2-4c): the different e-girth categories now spread out along the fit line, showing that Eq. (2.10) yields an easily computed heuristic to estimate the transition rates of edges in a given graph better than g_e alone. Moreover, the good fit suggests that interactions among cycles have only minor effects on the transition rates.

2.3 Discussion

2.3.1 Incompressible limit

Thus far, we have been considering approximate incompressibility with $\mu \gg \lambda$ but finite. We now pass to the fully incompressible limit $\mu \to \infty$, which necessitates a change of flow representation. In this limit, the dynamics of Φ are constrained to the null space $\ker \nabla$, and so Φ must be decomposed using a basis of $\ker \nabla$.

Dimensional reduction

Let $\mathbf{L} = \nabla^\top \nabla$ be the ($|\mathcal{E}| \times |\mathcal{E}|$, symmetric, positive semi-definite) Laplacian matrix on edges, and let $\{\Psi^1, \Psi^2, \ldots, \Psi^{|\mathcal{E}|}\}$ be an orthonormal basis of eigenvectors of $\mathbf{L}$ with components $\Psi^i = (\psi^i_e)$ and corresponding real, non-negative eigenvalues $\{\nu_1, \nu_2, \ldots, \nu_{|\mathcal{E}|}\}$. Note that this is not the same as the vertex Laplacian $L = \nabla\nabla^\top$, which will be the subject of Chapter 4. Now, using summation convention, let $f_i = \phi_e \psi^i_e$ be the components of Φ in this basis. Then by orthonormality of the basis vectors, $\phi_e = f_j \psi^j_e$, so f_i obeys

$$df_i = -\lambda V'(f_j \psi^j_e)\psi^i_e dt - \mu \nu_i f_i dt + \sqrt{2\beta^{-1}}\psi^i_e dW_{e,t},$$

with no sum over i. As $\mu \to \infty$, the second term damps to zero all f_i with non-zero eigenvalues $\nu_i > 0$, leaving only components with $\nu_i = 0$. The corresponding eigenvectors span $\ker \nabla$, the space of all incompressible flows termed the *cycle space* or *flow space*. Furthermore, orthonormality implies the noise term $\psi^i_e dW_{e,t}$ reduces to a single term of unit variance. Therefore, in this limit, the system obeys

$$df_\alpha = -\frac{\partial \hat{H}}{\partial f_\alpha} dt + \sqrt{2\beta^{-1}} dW_{\alpha,t},$$

where Greek indices run over only those components where $\nu_\alpha = 0$, and we use the reduced energy $\hat{H} = \lambda \sum_{e \in \mathcal{E}} V(f_\alpha \psi^\alpha_e)$.

Having reduced the dynamics onto $\ker \nabla$, we are now free to change basis inside

this subspace. In general, the orthonormal basis $\{\Psi^\alpha\}$ will not be physically intuitive, since its basis vectors include fractional flows on many edges. More comprehensible is a *cycle basis*, where basis vectors comprise unit flux flows around closed cycles. Such a basis of $\ker \nabla$ always exists: for example, one can start with an empty set C and repeatedly (1) add an arbitrary cycle c_i to C and (2) remove an arbitrary edge in c_i from G. After $\mathcal{E} - \mathcal{V} + n_c$ repetitions, where n_c is the number of components of G, each component will be reduced to a tree. Removing edges at every step ensures that the c_i are linearly independent and that the coefficients a_i in $v = \sum_{i=1}^{\mathcal{E}-\mathcal{V}+n_c} a_i c_i$ for any incompressible flow vector v can be recovered in order by matching the flow on each removed edge. While the intuitiveness comes at the cost of non-orthogonality, a cycle basis is particularly effective for planar graphs, as we describe next.

Fix a planar embedding for G. Let each $\{F_\alpha\}$ be the component of anti-clockwise flux around each of the $|\mathcal{E}|-|\mathcal{V}|+1$ non-external (finite) faces of G, and define the flux about the external (infinite) face to be zero. The flux on an edge is then simply the difference of the fluxes about its two adjacent faces. In particular, let $\mathbf{A} = (A_{\alpha e})$ be the matrix whose rows are the cycle basis vectors, so that $\phi_e = F_\alpha A_{\alpha e}$. This implies $F_\alpha = P_{\alpha e}\phi_e$ for $\mathbf{P} = (\mathbf{A}\mathbf{A}^\top)^{-1}\mathbf{A}$. The components F_α then obey

$$dF_\alpha = -(\mathbf{P}\mathbf{P}^\top)_{\alpha\gamma}\frac{\partial \hat{H}}{\partial F_\gamma}dt + \sqrt{2\beta^{-1}}dX_{\alpha,t}, \tag{2.11}$$

where $\hat{H}$ is the reduced energy $\hat{H} = \lambda \sum_{e\in\mathcal{E}} V(F_\alpha A_{\alpha e})$, and $\mathbf{X}_t$ is a vector of correlated Brownian noise with covariance matrix $\mathbf{P}\mathbf{P}^\top = (\mathbf{A}\mathbf{A}^\top)^{-1}$. Now, $A_{\alpha e}$ is non-zero only when edge e borders face α, and is then $+1$ or -1 depending on the orientation of the edge relative to the face. Therefore, $\mathbf{A}$ is all but one row of the incidence matrix of the planar dual of G, where the missing row is that corresponding to the external face, meaning $\tilde{\mathbf{L}} = \mathbf{A}\mathbf{A}^\top$ is the Laplacian on vertices of the dual (its *Kirchhoff matrix*) with the row and column corresponding to the external face deleted. Thus the independent edge noise turns into correlated noise with covariance $\tilde{\mathbf{L}}^{-1}$ which is typically non-zero almost everywhere. In other words, flux conservation means that the noise on one edge is felt across the entire graph.

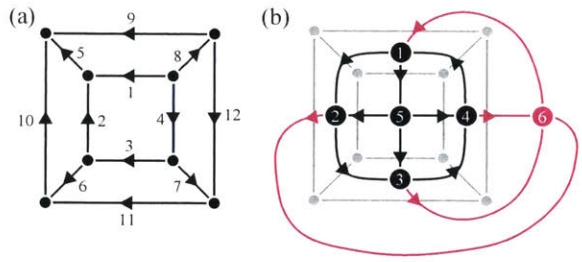

Figure 2-6: Constructing a cycle basis for $P_{4,1}$. (a) A planar embedding of $P_{4,1}$, with edges numbered and oriented as shown. (b) The dual of the embedding in (a), with dual graph vertices (original graph faces) numbered as shown. Edge orientations depend on those chosen in (a), as described in the text. Vertex 6 and its incident edges, highlighted, correspond to the external face whose flux is fixed at zero.

Cycle basis for $P_{4,1}$

As an example, we detail the derivation of the planar cycle basis representation in the incompressible limit for the cube $P_{4,1}$. Using the embedding shown in Fig. 2-6a, orient and number the edges as indicated. Next, construct the dual of the (undirected) plane graph, with vertices numbered as in Fig. 2-6b, and assign an orientation to each edge of the dual such that $A \to B$ implies that the flow on the edge between faces A and B is $F_B - F_A$, where F_α is the flow counter-clockwise around face α (Fig. 2-6b). This dual has incidence matrix

$$\mathsf{I} = \begin{pmatrix} -1 & 0 & 0 & 0 & -1 & 0 & 0 & 1 & 1 & 0 & 0 & 0 \\ 0 & 1 & 0 & 0 & 1 & -1 & 0 & 0 & 0 & -1 & 0 & 0 \\ 0 & 0 & 1 & 0 & 0 & 1 & -1 & 0 & 0 & 0 & -1 & 0 \\ 0 & 0 & 0 & 1 & 0 & 0 & 1 & -1 & 0 & 0 & 0 & -1 \\ 1 & -1 & -1 & -1 & 0 & 0 & 0 & 0 & 0 & 0 & 0 & 0 \\ 0 & 0 & 0 & 0 & 0 & 0 & 0 & 0 & -1 & 1 & 1 & 1 \end{pmatrix},$$

the rows of which are the cycle basis vectors. General face flow components $\mathbf{F} = (F_1, \ldots, F_6)$ then translate to edge flows $\Phi = (\phi_1, \ldots, \phi_{12})$ as $\phi_e = F_\alpha I_{\alpha e}$. However, there is a degree of freedom: adding a constant to each component of $\mathbf{F}$ results in the same Φ, so to obtain a unique correspondence between $\mathbf{F}$ and Φ we fix the external face flux $F_6 = 0$. Let A be I with the corresponding final row omitted and drop

the final component of $\mathbf{F}$. Then for $\Phi \in \ker \nabla$, $\phi_e = F_\alpha A_{\alpha e}$ inverts to $F_\alpha = P_{\alpha e}\phi_e$ with $\mathbf{P} = (\mathbf{A}\mathbf{A}^\top)^{-1}\mathbf{A}$. Thus the truncated dual Kirchhoff matrix $\tilde{\mathbf{L}} = \mathbf{A}\mathbf{A}^\top$ – which is independent of the edge orientations in Fig. 2-6b – reads

$$\tilde{\mathbf{L}} = \begin{pmatrix} 4 & -1 & 0 & -1 & -1 \\ -1 & 4 & -1 & 0 & -1 \\ 0 & -1 & 4 & -1 & -1 \\ -1 & 0 & -1 & 4 & -1 \\ -1 & -1 & -1 & -1 & 4 \end{pmatrix},$$

giving a noise covariance $\mathbf{P}\mathbf{P}^\top = \tilde{\mathbf{L}}^{-1}$ in Eq. (2.11) reading

$$\tilde{\mathbf{L}}^{-1} = \frac{1}{24}\begin{pmatrix} 10 & 5 & 4 & 5 & 6 \\ 5 & 10 & 5 & 4 & 6 \\ 4 & 5 & 10 & 5 & 6 \\ 5 & 4 & 5 & 10 & 6 \\ 6 & 6 & 6 & 6 & 12 \end{pmatrix}.$$

Observe that non-adjacent face pairs such as faces 1 and 3 have correlated noise.

Example

Figure 2-7 shows an integration of Eq. (2.11) for an embedding of the graph $P_{4,1}$ (Fig. 2-3), the cube, whose covariance matrix $\tilde{\mathbf{L}}^{-1}$ is non-zero everywhere. (In fact, the dual of a polyhedral graph is unique [142].) Note that the F_α need not only fluctuate around states $\{-1, 0, 1\}$, as seen in Fig. 2-7 when a state with $F_5 = +2$ is attained. The constraint now is that the *difference* $F_\alpha - F_\beta$ between adjacent faces α and β must be near $\{-1, 0, 1\}$, as this is the flux on the shared edge. Here, the central face F_5 can assume ± 2 if its neighbors are all ± 1. In general, a face of minimum distance d to the external face, which is constrained to zero flux, can be metastable at values up to $\pm d$ if all its neighbors are at $\pm(d-1)$. A further example on a 15×15 hexagonal lattice is given in Fig. 2-8.

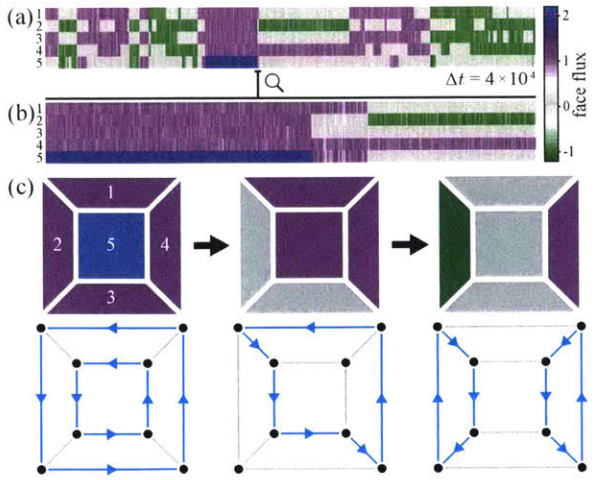

Figure 2-7: Incompressible flow on planar graphs can be represented using a face-based cycle basis. (a) Flux–time traces for flow about each of the internal faces of $P_{4,1}$, as labelled in (c), from Eq. (2.11) with $\lambda = 2.5$, $\beta^{-1} = 0.05$. (b) Zoom of trace showing a transition between two 8-cycles, which are global minima, via a 6-cycle. (c) Distinct state configurations in (b) of face fluxes (upper) and corresponding edge flows (lower).

2.3.2 Low temperature limit and ice-type models

Similar to how a lattice ϕ^4 theory generalizes the Ising model [143], on a regular lattice our model in the incompressible limit gives a lattice field theory generalization of ice-type or loop models [14, 16, 72]. Instead of there being a finite set of permitted flow configurations at each vertex, we now have a continuous space of configurations. Taking the low temperature limit $\beta\lambda \to \infty$ then recovers a discrete vertex model with $\phi_i \in \{-1, 0, 1\}$, where allowed configurations must be maximally flowing; thus, for example, a square lattice yields the six-vertex ice model [16]. For general G, the $\beta\lambda \to \infty$ limit can be understood as a form of random subgraph model [55], where the ground states are flows on maximum Eulerian subgraphs which are selected uniformly with a multiplicity of two for either orientation of every sub-cycle. On a cubic graph, a subset of the ground states are the Hamiltonian cycles (cycles covering every vertex exactly once), if they exist, since a maximally-flowing state will have two out of every three edges at every vertex flowing. The expected number of Hamiltonian cycles on a cubic graph grows like $|\mathcal{V}|^{-1/2}(4/3)^{|\mathcal{V}|/2}$ as $|\mathcal{V}| \to \infty$ [116], meaning large cubic graphs possess a huge number of ground states.

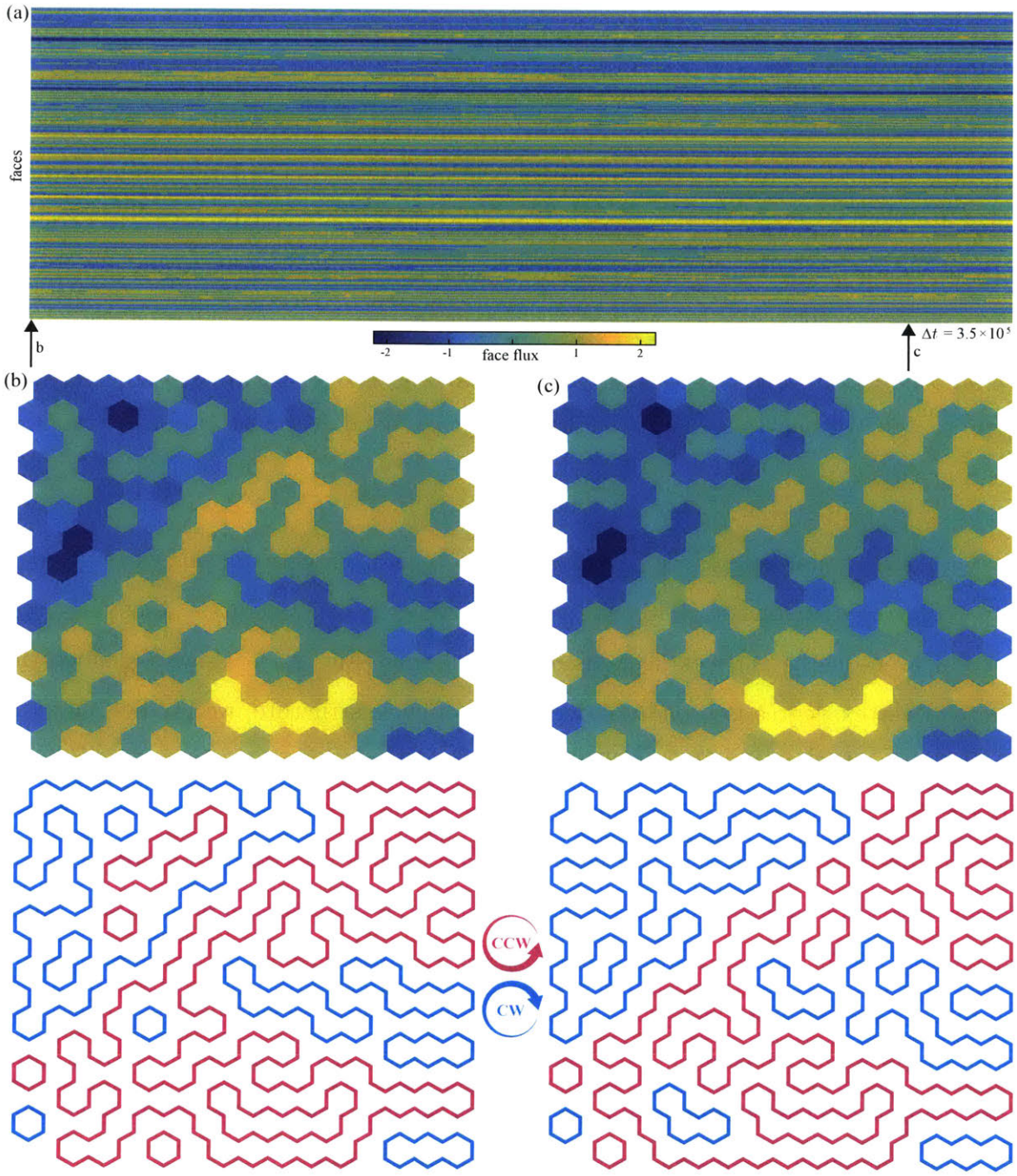

Figure 2-8: Incompressible flow on a 15×15 hexagonal lattice using the face cycle basis. (a) Plot of flux values over time for each face in an integration on the 15×15 lattice, at $\lambda = 2.5$, $\mu = 25$, $\beta^{-1} = 0.05$. (b,c) Configurations of the face fluxes at the times marked in (a), along with the cycle configurations they represent. Cycles are colored according to their orientation clockwise (cyan) or counterclockwise (magenta). Faces are ordered in (a) column-wise from bottom-left to top-right of the lattice.

2.3.3 Complex networks

We have focused on small regular graphs, but the dynamical principles presented here will still apply to active flow on complex networks. The edges in a large random graph typically exhibit a wide distribution of e-girths, where topologically protected edges, whose e-girth is large enough to prevent them ever changing state within a realistic observation window, coexist with frequently switching edges of small e-girth. In fact, graphs drawn from distributions modeling real-life network phenomena [12, 141] seem to have far more small e-girth edges than their fixed degree or uniformly random counterparts.

Unlike the cubic graphs we have focused on, a complex network possesses a broad vertex degree distribution. This will certainly affect transition rates, since the presence of even-degree vertices deepens energy minima (Fig. 2-1). However, since the effect of vertex degree is broadly independent of cycle structure, we predict that the distribution of transition rates will still qualitatively match the e-girth distribution. In Fig. 2-9 we plot e-girth distributions derived from ten instances each of four random graph distributions on 1000 vertices: fixed degree 3, uniform, Barabási–Albert ('scale free'), and Watts–Strogatz ('small world'). Of the four, random cubic graphs display by far the highest e-girths, whereas the Barabási–Albert and Watts–Strogatz graphs, commonly used as prototypes of certain forms of real-life complex networks, both retain many edges with low e-girth despite their size. Therefore, by this measure, complex networks may exhibit a far greater proportion of fast-switching edges than random cubic graphs on the same number of vertices.

Furthermore, though large random graphs are almost always asymmetric [53], many real-life complex networks have very large automorphism groups [81] meaning that, as in Fig. 2-3, there will be large sets of edges in such a network with identical transition rates. Active flow on complex networks can therefore be expected to display a rich phenomenology of local and global state transitions.

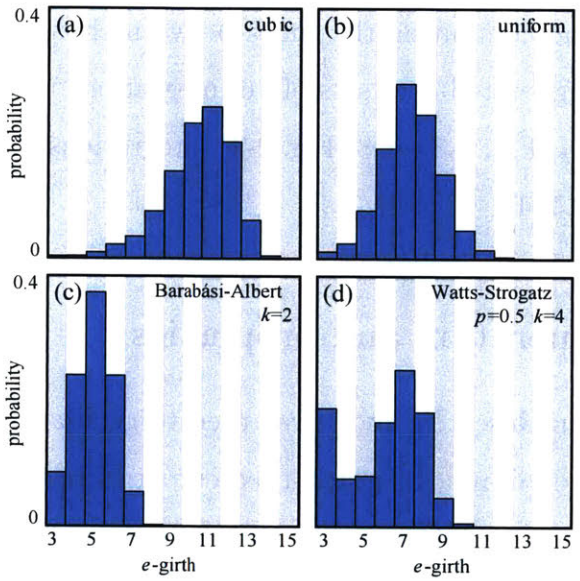

Figure 2-9: Empirical probability distributions of e-girth determined from ten graph realizations each from four random 1000-vertex graph ensembles: (a) fixed degree 3, i.e. cubic; (b) uniform with 1500 edges; (c) 'scale free' Barabási–Albert with a degree $k = 2$ vertex added at every step; and (d) 'small world' Watts–Strogatz with rewiring probability $p = 0.5$ and mean degree $k = 4$. The pseudo-real-life networks of (c) and (d) exhibit distributions with far more small e-girth edges than the more generic random graphs in (a) and (b).

2.4 Numerical methods

2.4.1 Numerical integration and waiting times

Equations (2) and (6) were integrated by the Euler–Maruyama method with time step $\delta t = 5 \times 10^{-3}$. After an initialization period to $t = 500$, state transition waiting times in Figs. 2-2 to 2-4 were determined by applying a moving average filter of width $\Delta t \approx 3$ to eliminate noise-induced recrossings of $\pm\frac{1}{2}$ without a true state change, rounding to the nearest integer, and computing the times between changes in this integer state. Waiting times were aggregated over sets of 16 integrations to $t = 4 \times 10^5$ for each λ in Fig. 2-2, and over 24 (Fig. 2-3) or 8 (Fig. 2-4) integrations to $t = 1.6 \times 10^6$ for each graph in Figs. 2-3 and 2-4.

2.4.2 Graph generation and properties

Mathematica (Wolfram Research, Inc.) was used to generate graphs and their incidence matrices and to determine all graph-theoretic properties including cycle lengths and edge equivalence classes. The graphs in Fig. 2-4 and Fig. 2-5 were chosen uniformly at random from the database of all non-isomorphic bridgeless connected cubic graphs on 14 vertices accessible in Mathematica after filtering to discard those with non-trivial automorphism group. A bridge is a single edge that is not part of any cycle and therefore cannot support incompressible flow.

2.5 Conclusions

Our analysis shows that the state transition statistics of actively driven nearly incompressible flow networks can be understood by combining reaction rate theory with graph-theoretic symmetry considerations. In particular, we have shown that the girth of an edge is a strong predictor of the time it takes to change its flow, and therefore that the length of a cyclic flow directly determines its stability. Furthermore, our results suggest that non-equilibrium flow networks may offer new insights into

ice-type models and *vice versa*. The framework developed here offers ample opportunity for future generalizations both from a biophysical and a transport optimization perspective. For example, an interesting open biological question concerns how plasmodial organisms such as *Physarum* [2, 95, 131] adapt and optimize their network structure in response to external stimuli, such as light or nutrient sources or geometric constraints [3, 113]. Our investigation suggests that a combined experimental and mathematical analysis of cycle structure may help explain the decentralized computation strategies employed by these organisms. More generally, it will be interesting to explore whether similar symmetry-based statistical approaches can guide the topological optimization of other classes of non-equilibrium networks, including neuronal and man-made information flow networks that typically operate far from equilibrium.

Chapter 3

Compressible active flow networks

After the extensive investigation of the incompressible case in the previous chapter, we will now turn to the case where density or volume can change across the network.[1] Building on Rayleigh's work [112] on driven vibrations and the Toner-Tu model of flocking [133], the theory accounts for network activity through a nonlinear friction [32, 117, 121, 133]. We work in a fully compressible framework allowing accumulated matter at vertices to affect flow through network pressure gradients, as suited to the many biological systems exhibiting flexible network geometry [2, 4, 131] or variations in the density of active components [124]. Although inherently nonlinear, the model can be systematically analyzed through perturbation theory. Such analysis shows how slow global dynamics emerge naturally from the fast local dynamics, enabling prediction of the typical states in large noisy networks; these states have significantly fewer active modes than for energy equipartition [70] in thermal equilibrium. More broadly, our model provides an accessible framework for investigating generic physical phenomena in active systems, including topologically-protected sound modes [124] and the influence of spectral band gaps.

[1] This work was published in the following paper:
Aden Forrow, Francis G. Woodhouse, and Jörn Dunkel. Mode Selection in Compressible Active Flow Networks *Phys. Rev. Lett.*, 119(2):028102, 2017.

3.1 Model

We consider activity-driven mass flow on an arbitrarily-oriented graph $G = (\mathcal{V}, \mathcal{E})$ with $V = |\mathcal{V}|$ vertices and $E = |\mathcal{E}|$ edges. The elements of the $V \times E$ gradient (incidence) matrix ∇ are $\nabla_{ve} = -1$ if edge e is oriented outwards from vertex v, $\nabla_{ve} = +1$ if e is oriented inwards into v, and $\nabla_{ve} = 0$ otherwise. The dynamical state variables are the deviations from the mean mass $\bar{\varrho} = M/V$ on the nodes, $(\varrho_1(t), \ldots, \varrho_V(t))$, and the mass fluxes on the edges, $(\phi_1(t), \ldots, \phi_E(t))$, governed by the non-dimensionalized transport equations

$$\dot{\varrho}_v = \sum_e \nabla_{ve} \phi_e, \tag{3.1a}$$

$$\dot{\phi}_e = -\sum_v \nabla_{ev}^\top \varrho_v + \epsilon \frac{\mu - \phi_e^2}{1 + \phi_e^2} \phi_e + \sqrt{2D}\xi_e(t), \tag{3.1b}$$

where $\xi_e(t)$ is standard Gaussian white noise. Equation (3.1a) ensures mass conservation. The first term on the r.h.s. of Eq. (3.1b) represents the gradient of an ideal gas-type node pressure $p_v \propto \varrho_v$, corresponding to the leading term in a virial expansion; the second term is a Toner-Tu type active friction force derived from a depot model [118, 121] with coupling $\epsilon > 0$ and active–passive control parameter μ, which drives the edge fluxes ϕ_e towards preferred values $\pm\sqrt{\mu}$ when $\mu > 0$. Many networks have non-uniform edge and vertex weights, which can be incorporated into equations of identical form to Eqs. (3.1) with appropriate rescaling of ϱ, ϕ, and ∇, as we will see in the next section.

3.1.1 Weight scaling and nondimensionalization

We could define the model in terms of the dimensional quantities $\hat{\varrho}_v$, $\hat{\phi}_e$, and $\hat{t}$; global dimensional parameters $\hat{\epsilon}$, $\hat{\beta}$, and $\hat{D}$; dimensional edge conductances $\hat{w}_e$ and vertex volumes $\hat{m}_v$; and a dimensionless global parameter μ and function g as

$$
\begin{aligned}
\frac{d\hat{\varrho}_v}{d\hat{t}} &= \sum_e \nabla_{ve}\hat{\phi}_e, \\
\frac{d\hat{\phi}_e}{d\hat{t}} &= -\hat{w}_e \sum_v \nabla_{ev}^{\top}\hat{m}_v^{-1}\hat{\varrho}_v + \hat{\epsilon} g\left(\mu, \frac{\hat{\phi}_e}{\hat{\beta}\hat{w}_e}\right)\hat{\phi}_e + \sqrt{2\hat{D}}\hat{\xi}_e(\hat{t}).
\end{aligned}
$$

The scaling by conductance in the argument of g is chosen to match the phenomenology observed in dense bacterial suspensions, where activity selects a characteristic velocity and not a fixed flux; if the edges are all of the same length, which can be achieved by appropriately discretizing an experimental network, the velocity will be proportional to ϕ_e/w_e and not ϕ. If we choose a conductance scale $\hat{w}$ and volume scale $\hat{m}$ (which together give a time scale $(\hat{m}/\hat{w})^{1/2}$) and insert the rescaled, nondimensional parameters

$$
w_e = \hat{w}^{-1}\hat{w}_e, \qquad m_v = \hat{m}^{-1}\hat{m}_v, \qquad \epsilon = \left(\frac{\hat{m}}{\hat{w}}\right)^{\frac{1}{2}}\hat{\epsilon}, \qquad D_e = \left(\hat{\beta}\hat{w}\right)^{-2}\left(\frac{\hat{m}}{\hat{w}}\right)^{\frac{1}{2}} w_e^{-1}\hat{D}
$$

and variables

$$
\begin{aligned}
\varrho_v &= m_v^{-\frac{1}{2}}\left(\frac{\hat{m}}{\hat{w}}\right)^{-\frac{1}{2}}\left(\hat{\beta}\hat{w}\right)^{-1}\hat{\varrho}_v, & \phi_e &= w_e^{-\frac{1}{2}}\left(\hat{\beta}\hat{w}\right)^{-1}\hat{\phi}_e, \\
t &= \left(\frac{\hat{m}}{\hat{w}}\right)^{-\frac{1}{2}}\hat{t}, & \xi_e(t) &= \left(\frac{\hat{m}}{\hat{w}}\right)^{\frac{1}{4}}\hat{\xi}_e(\hat{t}),
\end{aligned}
$$

we are left with

$$
\begin{aligned}
\frac{d\varrho_v}{dt} &= \sum_e m_v^{-1/2}\nabla_{ve} w_e^{1/2}\phi_e, \\
\frac{d\phi_e}{dt} &= -\sum_v w_e^{1/2}\nabla_{ev}^{\top} m_v^{-1/2}\varrho_v + \epsilon g\left(\mu, \frac{\phi_e}{\sqrt{w_e}}\right)\phi_e + \sqrt{2D_e}\xi_e(t).
\end{aligned}
$$

With constant conductances $w_e = 1$ and volumes $m_v = 1$, we recover the model

introduced above, namely

$$\frac{d\varrho_v}{dt} = \sum_e \nabla_{ve}\phi_e, \tag{3.2a}$$

$$\frac{d\phi_e}{dt} = -\sum_v \nabla_{ev}^\top \varrho_v + \epsilon g(\mu,\phi_e)\phi_e + \sqrt{2D}\xi_e(t), \tag{3.2b}$$

with nonzero entries of the gradient matrix equal to ± 1 and $g(\mu,\phi_e) = \frac{\mu-\phi_e^2}{1+\phi_e^2}$. All of our analysis applies equally well to the varying weights case: the only substantive changes are replacing ∇_{ve} with the weighted gradient $\nabla^*_{ve} = m_v^{-1/2}\nabla_{ve}w_e^{1/2}$ and choosing the appropriate scaling for the noise and activity.

We can combine Eqs. (3.2a) and (3.2b) into one second order equation for the pressure dynamics reading

$$\ddot{\varrho}_v = \sum_e \nabla_{ve}\left(-\sum_u \nabla_{eu}^\top \varrho_u + \epsilon g(\mu,\phi_e)\phi_e + \sqrt{2D}\xi_e(t)\right). \tag{3.3}$$

In the absence of friction, when $g(\mu,\phi_e) = 0$, the dynamics are Hamiltonian with energy

$$H = \frac{1}{2}\sum_{v,e,u} \varrho_v \nabla_{ve}\nabla_{eu}^\top \rho_u + \frac{1}{2}\sum_{e,v,f} \phi_e \nabla_{ev}^\top \nabla_{vf}\phi_f. \tag{3.4}$$

The energy is particularly simple when written in the basis of singular vectors of $\nabla^\top$ with non-zero singular values, giving

$$H = \frac{1}{2}\sum_n \lambda_n^2\left(r_n^2 + f_n^2\right) \equiv \sum_n H_n.$$

3.1.2 Relation to physical flow systems

We choose to explore a minimal model coupling local active energy input to network structure, rather than capture the details of any particular model system. Nevertheless, the key features of our model, namely mass conservation and a polynomial expansion of the active term, are generic enough to be straightforwardly adapted to

a range of applications.

Mass conservation and pressure driven flow are likely to remain in any active flow model; the form of the active term may change in different contexts. In our case, staying close to examples of bacterial suspensions, we model activity as driving spontaneous flow on all edges. An alternative option, more closely related to shuttle streaming in networks, would be to apply an active force f_v that compresses or expands each vertex and drives flow in or out, with modified dynamics

$$\begin{aligned} \frac{d\varrho_v}{dt} &= \sum_e \nabla_{ve}\phi_e, \\ \frac{d\phi_e}{dt} &= -\sum_v \nabla_{ev}^{\top}(\varrho_v + \epsilon f_v) + \sqrt{2D}\xi_e(t). \end{aligned}$$

The correct form of the active force depends on the microscopic details of the driving. Some generic features, however, will not depend on the exact form of f_v and will be discoverable by choosing a simple function of local quantities (ϱ_v, $\dot{\varrho}_v$, etc.) as an approximate driving force.

The same method is used to derive the Toner-Tu equations for continuous active flows [133]; our model can be understood as a discrete version of a special case of these equations. If advective and diffusive terms are rendered negligible in favor of pressure-driven and activity-driven flow by geometric effects or otherwise, and we take only the linear term in the virial expansion of the active pressure, the general Toner–Tu model simplifies to

$$\frac{\partial \vec{v}}{\partial t} = \alpha\vec{v} - \beta|\vec{v}|^2\vec{v} - \sigma_1\vec{\nabla}(\rho - \rho_0) + \vec{f}, \qquad \frac{\partial \rho}{\partial t} + \vec{\nabla}\cdot(\vec{v}\rho) = 0.$$

In a limit where deviations from the mean density are small, so $\rho = \rho_0 + \eta\varrho$ for some $\eta \ll 1$, we can further reduce to

$$\frac{\partial \vec{v}}{\partial t} = \alpha\vec{v} - \beta|\vec{v}|^2\vec{v} - \eta\sigma_1\vec{\nabla}\varrho + \vec{f}, \qquad \eta\frac{\partial \varrho}{\partial t} + (\rho_0 + \eta\varrho)\vec{\nabla}\cdot\vec{v} + \eta\vec{v}\cdot\vec{\nabla}\varrho = 0.$$

Then on short time scales $\tau = t/\eta$, we have

$$\frac{\partial \vec{v}}{\partial \tau} = \eta\alpha\vec{v} - \eta\beta|\vec{v}|^2\vec{v} - \eta^2\sigma_1\vec{\nabla}\varrho + \eta\vec{f}, \qquad \frac{\partial \varrho}{\partial \tau} \approx -\rho_0\vec{\nabla}\cdot\vec{v},$$

where we neglect terms that must be of order η: if the coefficients α, β, and σ_1 are sufficiently large, their terms will remain relevant. The scaling of τ ensures that t is small when τ is order one or smaller. Discretizing the velocity and density fields as well as the noise $\vec{f}$ and replacing the continuous gradient with either $\nabla_{ev}^\top$ or $-\nabla_{ve}$ as appropriate yields Eqs. (3.2).

3.1.3 Compressibility

Compressibility as included in our model is intended to describe changes in density or volume of the active component, not the underlying fluid. For example, variations in ϱ may be interpreted as variations in the density of swimmers in a bacterial system or variations in the tube volume in *Physarum polycephalum*. Such systems may be effectively compressible even though the solvent fluid (e.g. water) is incompressible.

In some cases, compressibility is the primary object of interest. For example, Ref. [124] discusses sound in active fluids in a network using a continuous wave equation derived from the Toner-Tu model. On top of a background flow taking the form of a lattice of counter-rotating cycles, they find modes confined to the edges of a Lieb lattice, which we can reproduce in our discretized setting (Fig. 3-1). In both their setting and ours, these edge modes decay over time without propagating into the bulk (cf. discussion in App. I.B of Ref. [124]).

We can recover an incompressible limit of our model by first extending it to include damping on the vertices:

$$\frac{d\varrho_v}{dt} = \sum_e \nabla_{ve}\phi_e - \eta\varrho_v, \tag{3.9a}$$

$$\frac{d\phi_e}{dt} = -\gamma\sum_v \nabla_{ev}^\top\varrho_v + \epsilon g(\mu,\phi_e)\phi_e + \sqrt{2D}\xi_e(t). \tag{3.9b}$$

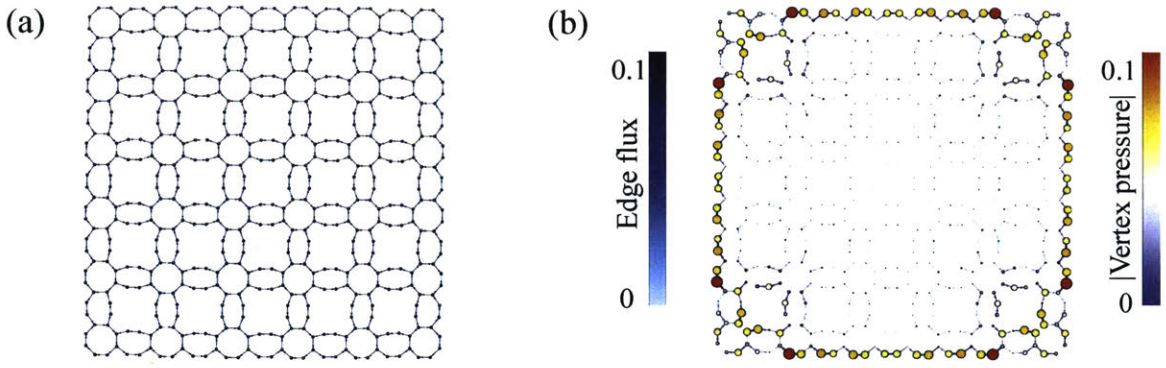

Figure 3-1: Our active network model exhibits behavior similar to the topological edge modes of Ref. [124]. (a) A discretized version of the Lieb lattice considered in Ref. [124]. Edges shared by adjacent 8-cycles have weight $w_e = 2$ to account for the additional width of the corresponding channels. The most stable flow on this network consists of a lattice of counter-rotating cycles, in which both the active friction term $g(\mu, \phi_e/\sqrt{w_e})$ and the pressure variations ϱ_v are everywhere zero. (b) This lattice has modes confined to the edges of the domain, allowing sound waves to propagate and decay without scattering into the bulk (cf. discussion in App. I.B of Ref. [124]); one such mode is pictured. Simulations started in this mode as a perturbation to the most stable flow pattern do not cause density changes in the center. The network model allows study of such phenomena without resorting to full scale simulation of the flow patterns.

This chapter examines the limit $\eta \to 0$ where total mass is exactly conserved. The previous chapter, where we started from a purely edge-based perspective, is in fact the opposite limit, $\eta \to \infty$, where Eq. (3.9a) can only be balanced if $\varrho_v \to 0$ and

$$\varrho_v = \frac{1}{\eta} \sum_e \nabla_{ve} \phi_e.$$

Substituting this into Eq. (3.9b) gives

$$\frac{d\phi_e}{dt} = -\frac{\gamma}{\eta} \sum_v \nabla_{ev}^\top \nabla_{va} \phi_a + \epsilon g(\mu, \phi_e)\phi_e + \sqrt{2D}\xi_e(t).$$

With $g(\mu, \phi_e) = \phi_e^2(1 - \phi_e^2)$, this is equivalent to the model discussed in Chapter 2. If $\gamma \to \infty$ so that γ/η is constant, small deviations from incompressibility are allowed; if $\gamma/\eta \to \infty$, incompressibility is fully enforced. However, compressibility is a necessary ingredient for sound waves [124] and density oscillations [102].

3.2 Mode selection

Active flow networks described by Eqs. (3.2) exhibit rich oscillatory transport behavior, including the mode selection illustrated in and Fig. 3-2 for a hierarchically-weighted network with vertex degrees at most 3 as is typical of *Physarum polycephalum* [15]. When this network is initialized with zero pressure variation and flux, it typically settles into a quasi-steady state with a single dominant oscillation frequency on the highest-weight path. This is a manifestation of the fact that single-frequency selection is the norm on actively driven path graphs.

These oscillatory states arise from the interaction of the nonlinear active driving with the harmonic coupling between ρ and ϕ. With no friction, when $\epsilon = 0$, the normal modes of Eqs. (3.2) coming from the singular value decomposition of ∇_{ve} decouple into undamped harmonic oscillators with constant amplitudes fixed by the initial conditions. If we removed the harmonic terms and only had friction, the nonlinearity would drive the flux to $\pm\sqrt{\mu}$ on every edge. By combining both terms, we find that activity drives flow which the harmonic terms convert to oscillations; the two effects can balance when subsets of modes have fixed nonzero amplitudes, , as we shall show analytically below. In essence, the driving excites every mode linearly and then excited modes suppress other modes supported on similar edges.

Generally, the features of the steady-state attractor will be determined by the topology of the subgraph of high-weight edges, which may be much sparser than the original network. For this reason, as well as for ease of analysis and illustration, we will henceforth assume G to be a tree, as realized in certain peripheral sensory neurons [73], though in general the full model in Eqs. (3.2) is not restricted to any particular class of graph. The behaviors observed on trees can be extended to denser graphs by choosing appropriate edge weights. The complex active flow dynamics encoded by Eqs. (3.2) can be understood analytically by considering the basis of oscillation modes of the network, as we illustrate next in the fully deterministic case ($D = 0$).

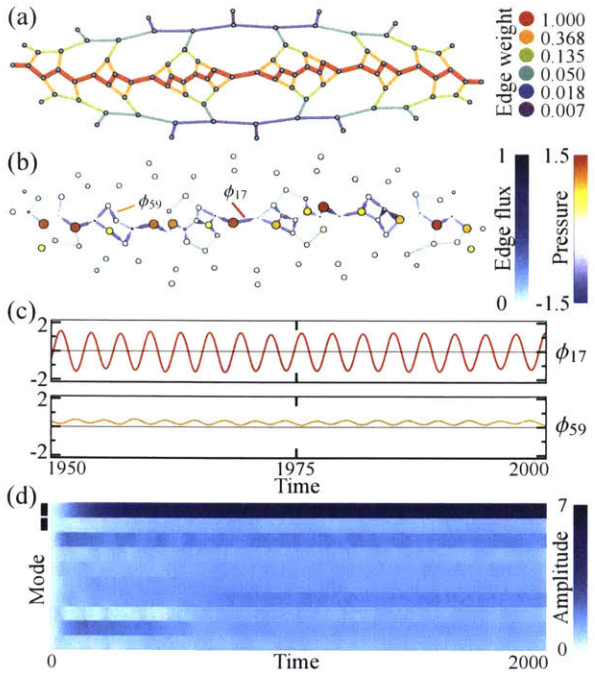

Figure 3-2: Activity can select a single dominant oscillation mode on hierarchically weighted networks. (a) The edges in the graph simulated in (b) and (c) are given weights decreasing exponentially with their distance from the central red path. (b) Oscillations in pressure and flux develop primarily along the central high-weight path. (c) Edge fluxes ϕ_e settle into steady synchronized oscillations as exemplified for two edges indicated in (b), one on (ϕ_{17}) and one off (ϕ_{59}) the path. (d) Plotting the time-dependent amplitude of each analytically-determined flow eigenmode confirms selection of a single oscillatory mode. The ten modes with the highest average amplitude in this simulation run are pictured; the marked top two rows are oscillatory modes, while the remaining rows are cyclic modes. See Fig. 3-3 for all modes. Simulation parameters are $\epsilon = 0.1$, $\mu = 1$, and $D = 10^{-4}$.

3.2.1 Rayleigh friction approximation

While choosing the friction function of the energy depot model introduced in Ref. [121],

$$g(\mu, \phi_e) = \frac{\mu - \phi_e^2}{1 + \phi_e^2},$$

has the convenient theoretical property that it gives a passive constant friction coefficient ϵ for $\mu = -1$ and for $\phi \to \infty$, it is analytically difficult. To simplify the analysis, we approximate this $g(\mu, \phi_e)$ with a symmetric quadratic [112]

$$\hat{g}(\mu, \phi_e) = a - b\phi_e^2, \tag{3.10}$$

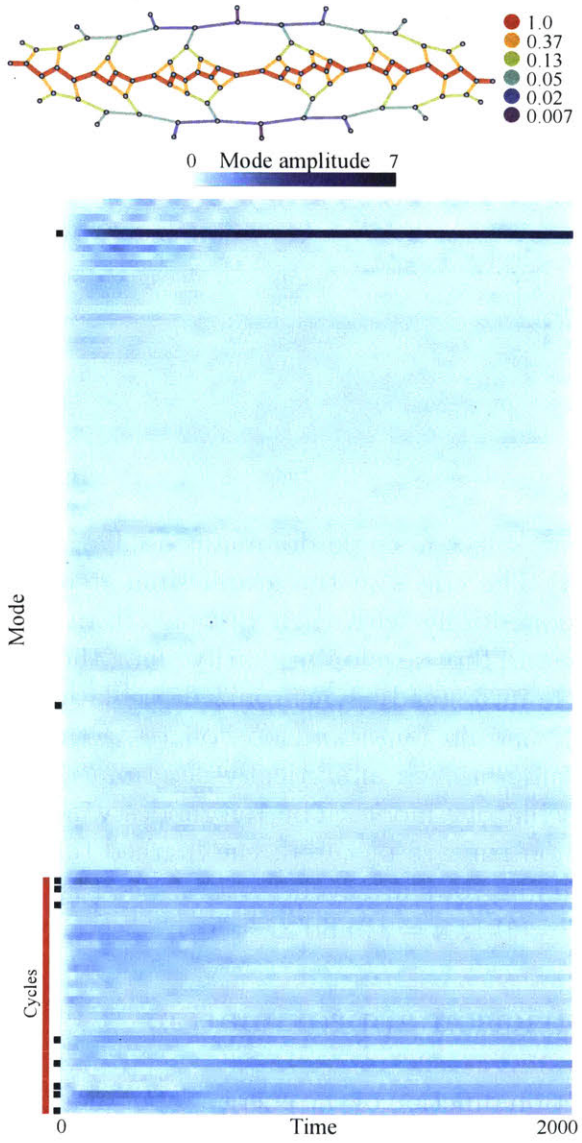

Figure 3-3: Including all of the modes from the simulation in Fig. 3-2 shows clear single mode selection on this weighted network. Edges a distance d from the central red path were given weight e^{-d}. Modes are ordered by frequency from high (top) to low (bottom); the last thirty modes, marked in red, are cycles. The modes pictured in Fig. 3-2 are marked in black.

where $a = \mu$ and $b = 1$ are chosen so that $\hat{g}(\mu, 0) = g(\mu, 0)$ and $\hat{g}(\mu, \phi_e)$ has the same zeros as $g(\mu, \phi_e)$. This ensures that the two functions approximately match when they are both negative, that is, when activity is putting energy into the flow. The large difference between $g(\mu, \phi_e)$ and $\hat{g}(\mu, \phi_e)$ when the flux is large is less important, as the flow will be damped down in either case. The larger damping in $\hat{g}(\mu, \phi_e)$ does result in slightly lower steady amplitudes, both analytically and in simulations.

3.2.2 Perturbation expansion

Now, expand the pressure $\varrho_v = \sum_{n=1}^{E} r_n(t)\varrho_{vn}$ and flux $\phi_e = \sum_{n=1}^{E} f_n(t)\phi_{en}$ in the right and left singular vectors $\boldsymbol{\varrho}_n = (\varrho_{vn})$ and $\boldsymbol{\phi}_n = (\phi_{en})$ of $\nabla^\top$ corresponding to the $E = V - 1$ non-zero singular values λ_n. (On a tree, there is a single zero eigenvalue of $\nabla\nabla^\top$ yielding an additional right singular vector for the pressure, but this corresponds to a constant mass shift and so can be safely neglected.) Defining mode amplitudes $A_n^2 = r_n^2 + f_n^2$, the network energy then takes the simple form $H = \frac{1}{2}\sum_n \lambda_n^2 A_n^2$.

When ϵ, the coefficient of the active driving term, is small there are two distinct timescales, namely the fast oscillation timescale t and the slow friction timescale $\tau = \epsilon t$.After writing ϱ_v and ϕ_e in the mode basis, we can further expand in ϵ as

$$r_n(t) = \sum_{k=0}^{\infty} \epsilon^k r_{kn}(t, \tau), \tag{3.11a}$$

$$f_n(t) = \sum_{k=0}^{\infty} \epsilon^k f_{kn}(t, \tau), \tag{3.11b}$$

where we explicitly separate the dependence on the two timescales. Then

$$\ddot{r}_{kn}(t, \tau) = \partial_t^2 r_{kn} + 2\epsilon\partial_t\partial_\tau r_{kn} + \epsilon^2\partial_\tau^2 r_{kn},$$

$$\ddot{f}_{kn}(t, \tau) = \partial_t^2 f_{kn} + 2\epsilon\partial_t\partial_\tau f_{kn} + \epsilon^2\partial_\tau^2 f_{kn}.$$

At zeroth order in ϵ, with $D = 0$, Eq. (3.3) becomes

$$\sum_{n=1}^{V} \partial_t^2 r_{0n} \varrho_{vn} = -\sum_{n=1}^{V} \lambda_n^2 r_{0n} \varrho_{vn}.$$

The modes ϱ_{vn} are orthonormal, so the terms decouple into separate harmonic oscillators; f_{kn} can be found from r_{kn} using Eq. (3.2a). The leading order solution is then

$$\begin{aligned} r_{0n}(t) &= A_{0n}(\tau)\cos(\lambda_n t - \delta_n(\tau)), \\ f_{0n}(t) &= -A_{0n}(\tau)\sin(\lambda_n t - \delta_n(\tau)). \end{aligned}$$

At first order in ϵ, with $g(\mu, \phi_e) = (\mu - \phi_e^2)$,

$$\sum_{n=1}^{V}(\partial_t^2 r_{1n} + 2\partial_t\partial_\tau r_{0n})\varrho_{vn} = -\sum_{n=1}^{V} \lambda_n^2 r_{1n}\varrho_{vn} + \sum_e \nabla_{ve}\left[\mu - \left(\sum_{n=1}^{E} f_{0n}\phi_{en}\right)^2\right] \sum_{\ell=1}^{E} f_{0\ell}\phi_e.$$

Multiplying by ϱ_{vm} and summing over v, we find

$$\partial_t^2 r_{1m} + 2\partial_t\partial_\tau r_{0m} = -\lambda_m^2 r_{1m} + \lambda_m\left[\mu f_{0m} - \sum_e \phi_{em}\left(\sum_{n=1}^{E} f_{0n}\phi_{en}\right)^3\right]. \tag{3.12}$$

3.2.3 Leading order amplitude dynamics

The influence of activity becomes apparent at first order in ϵ, introducing couplings between mode amplitudes whose dynamics encode the state selection behavior of the active network. Requiring that the $O(\epsilon)$ amplitudes r_{1n} and f_{1n} remain small relative to the leading terms implies that the secular (unbounded) terms in the first order equations must vanish [128]. Assuming negligible mode degeneracies, we will see that the slow dynamics of the $O(1)$ mode amplitudes $A_{0n}(\tau)$ obey

$$\frac{d(A_{0n}^2)}{d\tau} = \left(\mu - \sum_{k=1}^{E} P_{nk} A_{0k}^2\right) A_{0n}^2, \tag{3.13}$$

where the overlap matrix

$$P_{nk} = \frac{3}{2}(1 - \frac{1}{2}\delta_{nk}) \sum_e \phi_{en}^2 \phi_{ek}^2 \tag{3.14}$$

encodes the network topology. Fixed points of Eq. (3.13) can then be found by choosing a subset of the A_{0n} to be zero and solving

$$\sum_{k=1}^{E} P_{nk} A_{0k}^2 = \mu \tag{3.15}$$

for A_{0n}^2 over the remaining non-zero modes. If all the non-zero solutions for A_{0n}^2 are positive, then there is a stationary point with those modes activated.

In more detail, the argument in the previous paragraph begins by noting that the magnitudes of the summands r_{kn} and f_{kn} must remain bounded in order for the expansion in Eqs. (3.11a) and (3.11b) to make sense. From Eq. (3.12), r_{1m} is a harmonic oscillator with natural frequency λ_m driven by the zeroth order oscillations. It will have bounded oscillations only if the resonant terms in Eq. (3.12), those that drive r_{1m} at its natural frequency, are zero. Finding the resonant terms and setting them to zero will fix the leading order mode amplitudes $A_n(\tau)$.

Expanding the cube in Eq. (3.12) gives

$$\begin{aligned}
\partial_t^2 r_{1m} + 2\partial_t \partial_\tau r_{0m} &= -\lambda_m^2 r_{1m} + \lambda_m \left[\mu f_{0m} - \sum_e \phi_{em} \sum_{k,\ell,n=1}^{E} f_{0k}\phi_{ek} f_{0n}\phi_{e\ell} f_{0n}\phi_{en} \right] \\
&= -\lambda_m^2 r_{1m} + \lambda_m \left[\mu f_{0m} + \sum_{k,\ell,n=1}^{E} \left(\sum_e \phi_{em}\phi_{ek}\phi_{e\ell}\phi_{en} \right) \right. \\
&\qquad \left. \times A_{0k} A_{0\ell} A_{0n} \sin(\lambda_k t - \delta_k) \sin(\lambda_\ell t - \delta_\ell) \sin(\lambda_n t - \delta_n) \right].
\end{aligned} \tag{3.16}$$

Now, the product of sines can be expanded into

$$\begin{aligned}\sin(\lambda_k t - \delta_k)\sin(\lambda_\ell t - \delta_\ell)\sin(\lambda_n t - \delta_n) = \frac{1}{4}\Big[&\sin(\delta_k - \delta_\ell - \delta_n - \lambda_k t + \lambda_n t + \lambda_\ell t) \\ &- \sin(\delta_k - \delta_\ell + \delta_n - \lambda_k t - \lambda_n t + \lambda_\ell t) \\ &- \sin(\delta_k + \delta_\ell - \delta_n - \lambda_k t + \lambda_n t - \lambda_\ell t) \\ &+ \sin(\delta_k + \delta_\ell + \delta_n - \lambda_k t - \lambda_n t - \lambda_\ell t)\Big].\end{aligned}$$

We seek only resonant terms, which only occur when $\pm\lambda_k$, $\pm\lambda_\ell$, and $\pm\lambda_n$ sum to λ_m. This happens most often in one of two ways. First, we might have $k = \ell$ and $n = m$ or similar. Alternatively, we might have degenerate modes, $\lambda_k = \lambda_\ell$ and $\lambda_n = \lambda_m$. However, we ignore the latter possibility because degeneracies add significant analytic complications, including nontrivial dynamics of their relative phases. We also ignore the rare possibility of resonant terms arising from interactions of modes with three or four distinct singular values. The results we get with these assumptions closely match simulated time series (Fig. 3-6e-g), suggesting that the existence of degeneracies has little impact on the dynamics of nondegenerate modes.

The remaining resonant terms in Eq. (3.16) must cancel so that r_{1m} is not an oscillator of frequency λ_m driven at frequency λ_m. Thus,

$$\begin{aligned}2\partial_t\partial_\tau r_{0m} = \lambda_m\Bigg[&\mu f_{0m} + \frac{1}{4}\left(\sum_e \phi_{em}^4\right) A_{0m}^3(3\sin(\lambda_m t - \delta_m)) \\ &+ 3\sum_{k=1,k\neq m}^{E}\left(\sum_e \phi_{em}^2\phi_{ek}^2\right) A_{0k}^2 A_{0m}\frac{1}{4}(2\sin(\lambda_m t - \delta_m))\Bigg].\end{aligned}$$

Substituting in r_{0m} and f_{0m},

$$\begin{aligned}-2A'_{0m}\lambda_m\sin(\lambda_m t - \delta_m) + 2\lambda_m^2\cos(\lambda_m t - \delta_m)\delta'_m = \\ \lambda_m\Bigg[&-\mu A_{0m}\sin(\lambda_m t - \delta_m) + \frac{1}{4}\left(\sum_e \phi_{em}^4\right) A_{0m}^3(3\sin(\lambda_m t - \delta_m)) \\ &+ 3\sum_{k=1,k\neq m}^{E}\left(\sum_e \phi_{em}^2\phi_{ek}^2\right) A_{0k}^2 A_{0m}\frac{1}{4}(2\sin(\lambda_m t - \delta_m))\Bigg],\end{aligned}$$

where primes denote differentiation with respect to τ. For this to hold for all t we need the coefficients of the sine and cosine terms to separately cancel. From the cosine term, $\delta'_m = 0$; from the sine term,

$$\begin{aligned} A'_{0m} &= \frac{1}{2}A_{0m}\left(\mu - \frac{3}{4}\left(\sum_e \phi_{em}^4\right)A_{0m}^2 - \frac{3}{2}\sum_{k=1,k\neq m}^{E}\left(\sum_e \phi_{em}^2\phi_{ek}^2\right)A_{0k}^2\right) \\ &\equiv \frac{1}{2}A_{0m}\left(\mu - \sum_{k=1}^{E} P_{mk}A_{0k}^2\right), \end{aligned}$$

where the matrix $\mathbf{P}$ has entries

$$P_{mk} = \tfrac{3}{2}(1 - \tfrac{1}{2}\delta_{mk})\sum_e \phi_{em}^2\phi_{ek}^2$$

as specified in Eq. (3.14). Rewriting in terms of the squared amplitudes,

$$\frac{d}{d\tau}(A_{0m}^2) = 2A_{0m}A'_{0m} = A_{0m}^2\left(\mu - \sum_{k=1}^{E} P_{mk}A_{0k}^2\right). \tag{3.17}$$

As a matrix equation, with $x_m = A_{0m}^2$, this reads

$$\mathbf{x}' = \mathbf{x} \odot (\mu\mathbf{1} - \mathbf{P}\mathbf{x}), \tag{3.18}$$

where $\mathbf{1}$ denotes the vector of ones and $\odot$ is the component-wise product.

To find stationary points, we set

$$\mathbf{x} \odot (\mu\mathbf{1} - \mathbf{P}\mathbf{x}) = 0. \tag{3.19}$$

The obvious way to solve Eq. (3.18) for all stationary points is to exhaustively search over combinations of active modes: on picking certain elements of $\mathbf{x}$ to be zero, the remaining nonzero entries $\hat{\mathbf{x}}$ are found by solving $\hat{\mathbf{P}}\hat{\mathbf{x}} = \mu\mathbf{1}$, where $\hat{\mathbf{P}}$ is $\mathbf{P}$ restricted to those modes chosen to be nonzero. Stability of a fixed point $\mathbf{x}_0$ then follows by standard perturbation analysis: inserting a small perturbation $\mathbf{x}_0 + \delta\mathbf{x}(\tau)$ into

Eq. (3.18) gives

$$\delta\mathbf{x}' = \delta\mathbf{x} - \mathbf{x}_0 \odot (\mathbf{P}\delta\mathbf{x}) - (\mathbf{P}\mathbf{x}_0) \odot \delta\mathbf{x} + O(\delta\mathbf{x}^2) \equiv \mathbf{M}\delta\mathbf{x} + O(\delta\mathbf{x}^2),$$

where $\mathbf{I}$ denotes the identity matrix, and the eigenvalues of $\mathbf{M}$ then determine stability in the usual fashion.

3.2.4 Accuracy of Rayleigh friction approximation

To verify that the Rayleigh friction approximation does not significantly impact the results, we check the amplitude and stability of single modes for the full model with $g(\mu, \phi_e) = (\mu - \phi_e^2)/(1 + \phi_e^2)$ on all edges. Here setting the first order secular terms to zero in a perturbation expansion with $A_{0n} = A_{0p}\delta_{np}$ leads to

$$A_{0p}^2 = (\mu + 1) \sum_e \left(2 - 2\sqrt{\frac{1}{1 + A_{0p}^2 \phi_{ep}^2}} \right). \tag{3.20}$$

Numerically solving Eq. (3.20) for $\mu = 1$ yields solutions within a few percent of the Rayleigh approximation solution $1/\sqrt{P_{pp}}$ which additionally match numerical simulations of the full model even for ϵ as large as 0.5 (Fig. 3-4).

When the system transitions from no energy input to active flow, the steady state amplitudes will grow with μ. If we assume $\mu \ll 1$ (so $A_p \ll 1$) and expand the square root to order A_p^4, we find

$$A_p^2 + O(A_p^4) = \mu / P_{pp}, \tag{3.21}$$

matching the Rayleigh friction result to leading order. The scaling $A_p \sim \sqrt{\mu}$ is typical of a supercritical Hopf bifurcation.

3.2.5 One- and two-mode selection

Activity-driven fixed points with exactly one mode active always exist. If only mode p is active at leading order, then $A_{0n} = \sqrt{\mu/P_{pp}}\,\delta_{np}$ is a fixed point of Eq. (3.13). These amplitudes, which closely match both those calculated with the full unapproximated

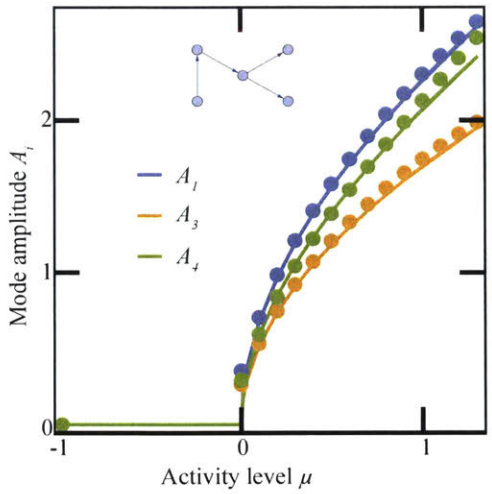

Figure 3-4: Steady state amplitudes A_i as a function of activity μ for the tree pictured undergo a Hopf bifurcation as μ crosses 0. Dots are long-time root-mean-square amplitudes from simulations started in each mode; lines are numerical solutions of Eq. (3.20). Mode A_2 is too unstable to reliably observe in simulations, so it is omitted. For $\mu < 0$, all amplitudes go to zero in simulations; the dot included in that region is at $\mu = -1$ where the friction is purely passive. Some deviations between simulation and analytics are expected because the simulations do not use the Rayleigh friction approximation and $\epsilon \neq 0$. Parameters are $\epsilon = 0.5$ and $D = 0$.

active friction force and those from averages computed over fully nonlinear simulations (Fig. 3-4), show that as μ crosses 0 there is a supercritical Hopf bifurcation with $A_{0n} \sim \sqrt{\mu}$. However, the stability of such a single-mode state depends on topology: our simulations suggest that activity always selects exactly one oscillation mode in simple path graphs, whereas single-mode states are typically unstable in networks with complex topologies. We can use this observation to model more complex active networks with single mode selection by appropriately weighting the edges: if the edge weights for a path are large enough compared to the weights elsewhere in the network, the path behavior dominates (Fig. 3-2).

Insight into stability is provided by the case with up to two modes active. Writing

$$A_{0n} = A_{0p}\delta_{np} + A_{0q}\delta_{nq}, \tag{3.22}$$

Eq. (3.13) yields

$$\frac{d(A_{0p}^2)}{d\tau} = (\mu - P_{pp}A_{0p}^2 - P_{pq}A_{0q}^2)\,A_{0p}^2, \tag{3.23}$$

and symmetrically for A_{0q}^2. Depending on the topology-encoding overlap coefficients P_{nk}, this gives up to four fixed points: the zero state $A_{0p} = A_{0q} = 0$, which is always linearly unstable; the single-mode state $(A_{0p}, A_{0q}) = (\sqrt{\mu/P_{pp}}, 0)$, which is stable if $P_{pq} > P_{pp}$ and a saddle if not, plus analogously for $(0, \sqrt{\mu/P_{qq}})$; and, potentially, a mixed state (A_{0p}^*, A_{0q}^*) where $A_{0p}^* = \sqrt{\mu\,(P_{qq} - P_{pq})/\left(P_{pp}P_{qq} - P_{pq}^2\right)}$ with A_{0q}^* defined symmetrically. When it exists, the mixed state is either stable (if $P_{pq}^2 < P_{pp}P_{qq}$) or a saddle (if $P_{pq}^2 > P_{pp}P_{qq}$), but if one of the single-mode states is stable and one is unstable, then one of A_{0p}^* and A_{0q}^* is imaginary and there is no mixed state. Hence, we have three possible scenarios (Fig. 3-5): one stable single mode and the other a saddle with no mixed state (Fig. 3-5b,c; left); two stable single-mode states with a mixed saddle in-between (Fig. 3-5b,c; center); and two single-mode saddles with a stable mixed state in-between (Fig. 3-5b,c; right). These predictions match simulations quantitatively even for relatively large ϵ beyond the small-ϵ perturbation regime (Fig. 3-5). In fact, simulations show the same qualitative behavior for $\epsilon = 2$, suggesting perturbation analysis remains predictive at high activity.

This two-mode analysis yields a simple topological heuristic for the stability of single-mode states. Since $|\boldsymbol{\phi}_p| = 1$, P_{pp} is small when $\boldsymbol{\phi}_p$ is spread over many edges and large when $\boldsymbol{\phi}_p$ is localized to a few edges. If $\boldsymbol{\phi}_q$ is localized to the same edges as $\boldsymbol{\phi}_p$, P_{pq} will also be large and mode p will be stable to perturbations in mode q. However, if $\boldsymbol{\phi}_q$ is localized to a disjoint set of edges, P_{pq} will be a scaled inner product of near-orthogonal vectors (ϕ_{ep}^2) and (ϕ_{eq}^2) and will be small. Thus localized modes will be unstable to modes in other regions, while conversely if a mode is to be stable alone then it will be spread out across the entire network. Therefore, a stable combination of modes will possess significant flows on all edges of the network.

The number of activated modes in an arbitrary compressible active network depends on intricate interactions between local activity and global flow configurations.

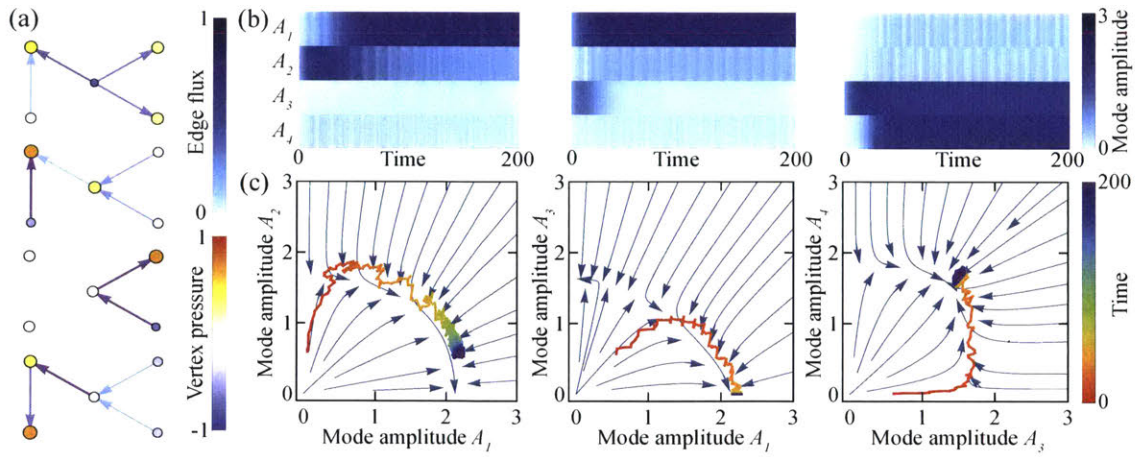

Figure 3-5: First order perturbation theory accurately predicts the stable states on small trees. (a) A five vertex tree possessing four nontrivial modes, as illustrated. (b) On the tree in (a), mode amplitudes settle into one of two stable stationary states, as seen in simulations for three different initial conditions. Modes are ordered by frequency from high (top) to low (bottom). (c) Simulated mode trajectories (rainbow) in (b) match analytic predictions (blue streamlines) in the subspaces of activated modes. There are three possible arrangements of nonzero critical points in each 2D subspace: a saddle point on one axis and a stable node on the other axis (left), a stable node on each axis and a saddle point in the middle (center), or a saddle point on each axis and a stable node in the middle (right). Higher order effects cause both the convergence to a point with $A_2 > 0$ in the left and middle plots and the oscillations in the trajectories. Parameters used are $\epsilon = 0.5$, $\mu = 1$, $D = 0$.

The total number of available modes is equal to the number of edges E, meaning that, were each combination of modes to be a fixed point, a tree could have up to 2^E stationary states. To see how the true number of stationary and stable states depends on tree size, we performed an exhaustive numerical fixed point search of Eq. (3.13) over a large sample of trees with $E \leq 24$ (Fig. 3-6a-d). The naive upper bound of 2^E suggests exponential growth of the mean number of steady states with edges E; this is indeed what we see, going as $\sim (2^E)^{4/5}$. However, though still exponential in E, the mean number of stable states is much smaller at $\sim (2^E)^{1/4}$ (Fig. 3-6a). Remarkably, these stable states have only $\sim E/4$ modes active on average (Fig. 3-6c) in stark contrast to the activation of all E modes under thermal equipartition [70]. Path-like topologies lead to even more dramatic reductions in the number of modes active (Fig. 3-6c), suggesting that a biological system can further reduce the number of active modes through an optimal choice of topology; moreover, hierarchically tuned

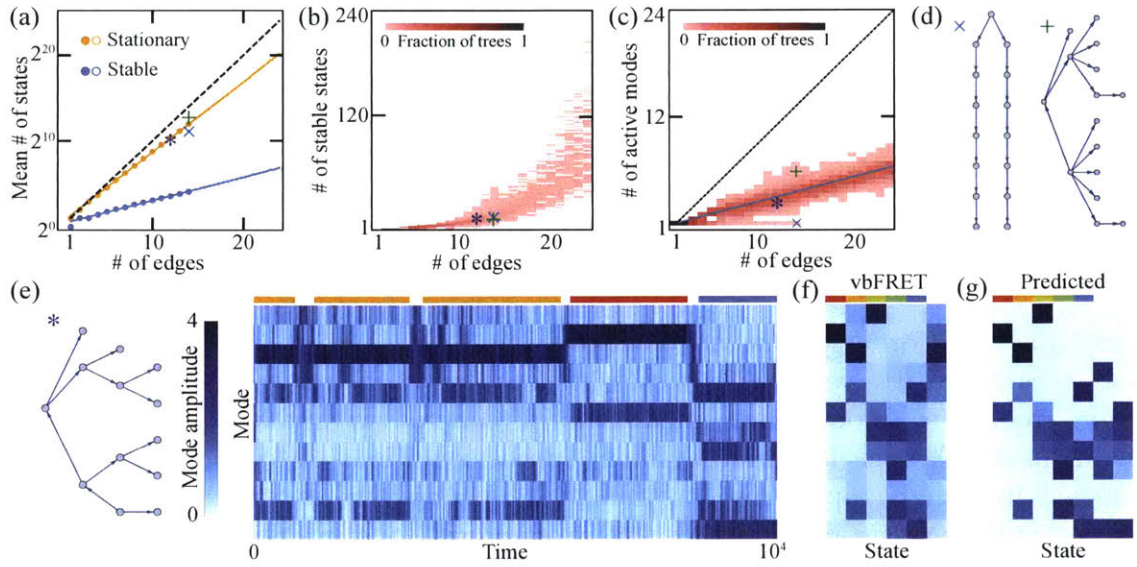

Figure 3-6: States on larger trees possess surprisingly few active modes, which can be inferred from time series with non-zero noise. (a) The mean number of stationary states of Eq. (3.13) grows exponentially with edges E as $1.77^E \approx (2^E)^{4/5}$ (solid orange line), close to the upper bound of 2^E states (dashed black line), while the mean number of stable states grows as $1.21^E \approx (2^E)^{1/4}$ (solid blue line). We counted states on all nonisomorphic trees with $E \leq 14$ edges (filled circles) and on a random sample of $\sim$ 175 trees per point for $15 \leq E \leq 24$ (open circles). Averages are over trees with a fixed number of edges. (b) As E increases, both the mean and the variance of the distribution of trees with each number of stable states increase rapidly. (c) Distribution of the average number of modes active in a stable state. The mean over trees scales like $0.26E \approx E/4$ (solid line), significantly below $E/2$ expected if modes were selected randomly. (d) Two example trees indicated in (a-c) by the corresponding colored symbols. Stable states on paths ($\times$) always only activate one mode; complex trees ($+$) have more modes active. (e) Noisy networks ($D > 0$) transition stochastically between stable states, exemplified by an amplitude-time trace for the tree shown. Modes are ordered by frequency from high (top) to low (bottom). Simulation parameters are $\epsilon = 0.5$, $\mu = 1$, $D = 5 \times 10^{-3}$. (f) States found by vbFRET from simulations on the tree in (e). The second, first, and fifth columns are states seen in (e), indicated by the colored bars above. (g) States predicted by Eq. (3.13) for the tree in (e). The first five states in (f) match those in (g); the sixth column in (f) is likely a transient combination of analytically stable states.

edge capacities as realized in *Physarum* [2, 4, 15] can further enhance mode selection even in non-tree topologies (Fig. 3-2).

3.2.6 Differential growth rates

While the $E/4$ active modes per state that we observe is significantly reduced relative to the total number of modes available, it is still a not insignificant fraction of E. There are, however, several straightforward generalizations of our model that may lead to more strict mode selection. We discuss two possibilities in this and the subsequent section: variations in activity across the network and variations in weights of vertices or edges.

For simplicity, we introduced Eqs. (3.2) with a uniform activity level μ across the entire network. This leads to equal driving on all modes: if Eq. (3.13) is initialized near zero, it can be linearized to

$$\frac{d}{d\tau}(A_{0m}^2) = \mu A_{0m}^2,$$

where all modes grow at the same rate. Mode selection occurs in this system only because of interactions between modes.

In many physical systems, however, differences in growth rate between modes are important for mode selection. For example, the Rayleigh-Plateau instability [111] causes fluid jets to break apart into droplets whose size is determined by the fastest growing unstable perturbation to the jet radius. Nonlinear mode competition akin to that in Eqs. (3.2) may only act on the subset of modes that grow quickly.

We can add this effect to our model by replacing μ in Eqs. (3.2) with edge-dependent parameters μ_e. With the quadratic driving of Eq. (3.10), Eq. (3.2b) becomes

$$\frac{d\phi_e}{dt} = -\sum_v \nabla_{ev}^\top \varrho_v + \epsilon\left(\mu_e - \phi_e^2\right)\phi_e + \sqrt{2D}\xi_e(t).$$

Following through the previous calculations with this change, Eq. (3.12) becomes

$$\partial_t^2 r_{1m} + 2\partial_t \partial_\tau r_{0m} = -\lambda_m^2 r_{1m} + \lambda_m \left[\sum_{e,l} \phi_{em} \mu_e f_{0l} \phi_{el} - \sum_e \phi_{em} \left(\sum_{n=1}^{E} f_{0n} \phi_{en} \right)^3 \right].$$

The first term inside the square brackets no longer simplifies, since the ϕ_{en} are not orthonormal with the weighting μ_e. However, if we again ignore degeneracies, the only resonant term is $\sum_e \phi_{em}^2 \mu_e f_{0m}$ from $l = m$. In this case, defining $\nu_m = \sum_e \phi_{em}^2 \mu_e$, Eq. (3.13) then reads

$$\frac{d}{d\tau}(A_{0m}^2) = A_{0m}^2 \left(\nu_m - \sum_{k=1}^{E} P_{mk} A_{0k}^2 \right), \tag{3.24}$$

where modes have distinct growth rates independent of their interactions. Alternatively, one could specify ν_m arbitrarily in Eq. (3.24), though this would require more complex changes in Eq. (3.2b) coupling activity across edges.

3.2.7 Higher order oscillations

Biological systems exhibit vastly different macroscopic and microscopic time scales [56, 69, 114, 136]. This phenomenon is present in our compressible active flow network, where higher-order nonlinear effects induce slow global time scales from faster small-scale dynamics. When the zeroth-order amplitudes A_{0n} are at a fixed point, the first-order corrections r_{1n} and f_{1n} are harmonic oscillators with natural frequency λ_n driven at linear combinations of the frequencies active at zeroth order. For instance, if two modes p and q are active at zeroth order, the driving frequencies are $3\lambda_p - k(\lambda_p \pm \lambda_q)$ for $k = 0, \ldots, 3$. This introduces new, slower timescales into the dynamics, including oscillations in the energy $H = \frac{1}{2}\sum_n \lambda_n^2 (r_n^2 + f_n^2)$ with frequency $\lambda_p - \lambda_q$. Their magnitude depends on the difference in frequency: slower oscillations, driven by modes with similar frequencies $\lambda_p \approx \lambda_q$, have higher amplitudes (Fig. 3-7).

Before, by setting resonant terms to zero, we found the slow dynamics of A_n. We can also look at the non-resonant terms driving r_{1m} to find higher order effects. If we

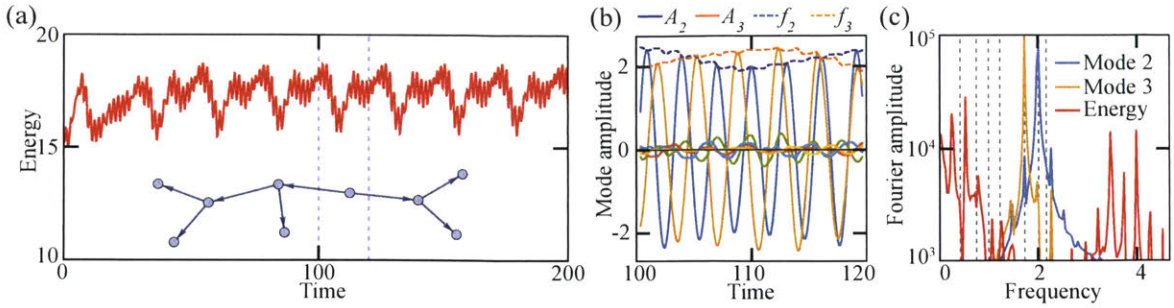

Figure 3-7: Slow global oscillations emerge from the fast active dynamics. (a) First order considerations fix a constant mean flow energy; higher order effects cause significant slow oscillations about that mean. Simulation parameters were $\mu = 1$, $\epsilon = 0.5$, and $D = 0$; the tree used is inset. (b) The mode amplitudes A_2 and A_3, like the energy, oscillate much more slowly than the harmonic oscillations of f_2 and f_3. All other mode amplitudes (unlabelled traces) are close to zero. (c) Frequency spectra of the two active modes and the energy H for the simulation in (a) and (b). The energy oscillates due to higher-order interactions between modes at frequencies that are linear combinations of active mode frequencies, not the harmonic frequencies alone (dashed lines).

let

$$S_{i_1^{n_1}\ldots i_k^{n_k}} = \sum_e \prod_{j=1}^{k} \phi_{ei_j}^{n_j},$$

assume the resonant terms are zero, and assume $A_{0m} = A_{0p}\delta_{mp} + A_{0q}\delta_{mq}$, the remainder of Eq. (3.12) is

$$\begin{aligned}
\partial_t^2 r_{1m} + \lambda_m^2 r_{1m} \;=\; & \frac{1}{4}\lambda_m \Big\{ S_{mp^3} A_{0p}^3 \sin(3\lambda_p t) \\
& + 3S_{mq^2p} A_{0p} A_{0q}^2 \big[\sin((2\lambda_q - \lambda_p)t) - \sin((2\lambda_q + \lambda_p)t) \big] \\
& + 3S_{mqp^2} A_{0p}^2 A_{0q} \big[\sin((2\lambda_p - \lambda_q)t) - \sin((2\lambda_p + \lambda_q)t) \big] \\
& + S_{mq^3} A_{0q}^3 \sin(3\lambda_q t) \Big\}. \qquad (3.25)
\end{aligned}$$

Setting $m = p$ and only looking at the terms closest to resonance, we obtain

$$\partial_t^2 r_{1p} + \lambda_p^2 r_{1p} \;\approx\; \frac{1}{4}\lambda_p \big\{ 3S_{q^2p^2} A_{0p} A_{0q}^2 \sin((2\lambda_q - \lambda_p)t) + 3S_{p^3q} A_{0p}^2 A_{0q} \sin((2\lambda_p - \lambda_q)t) \big\}.$$

Thus

$$\begin{aligned} r_{1p} &\approx c_1 \cos((2\lambda_q - \lambda_p)t - \delta_1) + c_2 \cos((2\lambda_p - \lambda_q)t - \delta_2), \\ f_{1p} &\approx -c_1 \sin((2\lambda_q - \lambda_p)t - \delta_1) - c_2 \sin((2\lambda_p - \lambda_q)t - \delta_2), \end{aligned}$$

where

$$\begin{aligned} c_1 &= \frac{3}{4((2\lambda_q - \lambda_p)^2 - \lambda_p^2)} \lambda_p S_{q^2p^2} A_{0p} A_{0q}^2, \\ c_2 &= \frac{3}{4((2\lambda_p - \lambda_q)^2 - \lambda_p^2)} \lambda_p S_{qp^3} A_{0p}^2 A_{0q}. \end{aligned}$$

The energy in this mode to first order in ϵ is

$$\begin{aligned} H_p &= \frac{\lambda_p^2}{2} \left((r_{0p}^2 + \epsilon r_{1p})^2 + (f_{0p}^2 + \epsilon f_{1p})^2 \right) + O(\epsilon^2) \\ &= \frac{\lambda_p^2}{2} \Big\{ A_{0p}^2 + 2\epsilon A_{0p} \big[c_1 \cos((2\lambda_q - 2\lambda_p)t) + c_2 \cos((\lambda_p - \lambda_q)t) \big] \Big\} + O(\epsilon^2), \end{aligned}$$

exhibiting an order ϵ time dependence. The coefficients c_1 and c_2 are small unless $\lambda_p \approx \lambda_q$. If we kept the frequency $3\lambda_p$, $3\lambda_q$, $2\lambda_p + \lambda_q$, and $2\lambda_q + \lambda_p$ terms from Eq. (3.25), we would find energy oscillations with frequencies $2\lambda_p$, $2\lambda_q$, $3\lambda_q - \lambda_p$, and $\lambda_p + \lambda_q$ (Fig. 3-7); those oscillations have smaller amplitudes as the driving is farther from resonance.

3.3 Stochastic forcing

Real active transport networks will have some nonzero level of thermal or athermal noise [49, 59, 77]. Provided the noise is not too large, it will render previously stable states now only metastable, with flow patterns exhibiting small fluctuations around these metastable states punctuated by noise-driven stochastic transitions between them [59, 145]. Long-time simulations of Eqs. (3.1) with $D > 0$ therefore offer an independent numerical way to find stable fixed points of the amplitude dynamics. We use vbFRET [26], a variational Bayesian analysis of a continuous time

hidden Markov model, to identify states from simulated time series. Almost all of the states discovered by vbFRET match stable states predicted by Eq. (3.13) even in the presence of non-negligible noise (Fig. 3-6e-g), justifying the simplifications used in deriving Eq. (3.13). This also promises that Bayesian methods like vbFRET will function as reliable inference tools for experimental data from real-life active flow networks [2, 84, 131].

3.3.1 Thermalization

In Eqs. (3.2a) and (3.2b) we add Gaussian white noise only to the flux as a physically intuitive source of random fluctuations that preserve mass conservation. However, even with purely passive friction, this does not lead to equipartition of energy as seen in thermal systems.

Written as stochastic differential equations with $g(\mu, \phi) = -1$, Eqs. (3.2a) and (3.2b) become

$$d\varrho_v = \sum_e \nabla_{ve}\phi_e dt, \tag{3.26a}$$

$$d\phi_e = -\sum_v \nabla_{ev}^\top \varrho_v dt - \epsilon\phi_e dt + \sqrt{2D}d\tilde{B}_e(t), \tag{3.26b}$$

where each $\tilde{B}_e(t)$ is standard Brownian motion. The components of the E-dimensional Brownian motion $\mathbf{B}(t) = (\tilde{B}_1, \ldots, \tilde{B}_E(t))$ in any orthonormal basis are also standard Brownian motions, so we can rewrite the system in the mode basis as

$$dr_n = \lambda_n f_n dt, \tag{3.27a}$$

$$df_n = -\lambda_n r_n dt - \epsilon f_n dt + \sqrt{2D}dB_n(t). \tag{3.27b}$$

The associated Fokker-Planck equation for the probability distribution $p(\mathbf{r}, \mathbf{f}, t)$ is

$$\partial_t p = \sum_n \left[-\frac{\partial}{\partial r_n}(\lambda_n f_n p) + \frac{\partial}{\partial f_n}(\lambda_n r_n p) + \frac{\partial}{\partial f_n}(\epsilon f_n p) + D\frac{\partial^2 p}{\partial f_n^2} \right]$$

with $p \to 0$ as $r_n, f_n \to \infty$ and p integrating to 1. Now, without friction or noise, the

dynamics are governed by the Hamiltonian

$$H = \frac{1}{2}\varrho_v \nabla_{ve} \nabla_{eu} \varrho_u + \frac{1}{2}\phi_e \nabla_{ev} \nabla_{va} \phi_a = \frac{1}{2}\sum_n \lambda_n^2 (r_n^2 + f_n^2) \equiv \sum_n H_n.$$

If p is a function of the H_n alone, the Fokker-Planck equation in steady state reduces to

$$0 = \sum_n \frac{\partial}{\partial f_n}(\epsilon f_n p) + D\frac{\partial^2 p}{\partial f_n^2},$$

which has solution

$$p(H_1, \ldots, H_M) \propto \prod_{n=1}^{M} e^{-\frac{H_n}{kT_n}},$$

where $kT_n = \lambda_n^2 D/\epsilon$.

Loosely, adding noise this way couples each mode to a heat bath with a distinct temperature. The result is equipartition of amplitude, not energy: the long-time average $\langle A_n^2 \rangle$ is independent of n. Adding weak coupling between modes by making $\mu > -1$ does not change this.

To get equipartition of energy one could change the coupling to noise, replacing the final term in Eq. (3.27b) with

$$\sqrt{2D_n} dB_n(t) \equiv \frac{\sqrt{2D}}{\lambda_n} dB_n(t).$$

This is only possible for $\lambda_n \neq 0$, which precludes cyclic modes. Equation (3.2b) becomes

$$d\phi_e = -\sum_v \nabla_{ev}^\top \varrho_v dt + \epsilon g(\mu, \phi_e)\phi_e dt + \sum_n \frac{1}{\lambda_n}\phi_{en}\sqrt{2D} dB_n(t).$$

The previous analysis goes through identically, leading to

$$kT_n = \lambda_n^2 D_n/\epsilon = D/\epsilon. \tag{3.28}$$

3.4 Complex networks

To show more concretely the possible oscillatory steady states of Eqs. (3.2), we will describe simulation results for a few example networks. Even with cycles, which we did not explicitly account for in the perturbative analysis in this chapter, the qualitative features of stochastic switching among selected modes remains.

3.4.1 Attractor characteristics on tree networks

The mode interactions of Eq. (3.18) can lead to complex oscillation patterns dependent on global, not local, topology, as shown for a 127-vertex complete binary tree in Fig. 3-8. After initializing with zero pressure variation and flux, the system settles into quasi-steady states with dramatically different dynamics in separate regions of the tree (Fig. 3-8a,b). Flux in edges near the leaves of the tree tends to oscillate rapidly, driving large pressure fluctuations in nearby vertices, whereas flux oscillations near the root are comparatively slow with nearly constant pressure in the vertices (Fig. 3-8b,d). Since, apart from the root and leaves, each vertex has the same local topology, the different time scales emerge from the interaction of the local active friction with the global structure of the tree.

A comprehensive and precise characterization of the relative lifetimes of different attractors in large active flow networks remains out of reach with current numerical methods, in part because the range of noise levels low enough to observe state selection and high enough to observe transitions is quite small. Such a fine-tuning between thermal and active transport processes is a characteristic feature of many, if not all, biological systems that function optimally in a narrow temperature range: bacterial flagellar motors are designed to barely beat Brownian diffusion at room temperature, ATP-driven intracellular transport is tuned such that it improves moderately over thermal diffusion, and so-on. Another well-known example in this context is stochastic resonance in driven multistable systems [49]. However, as all these systems typically exhibit exponential Arrhenius-type waiting times, it is practically impossible to completely explore their attractor statistics in the moderate-to-weak noise regime,

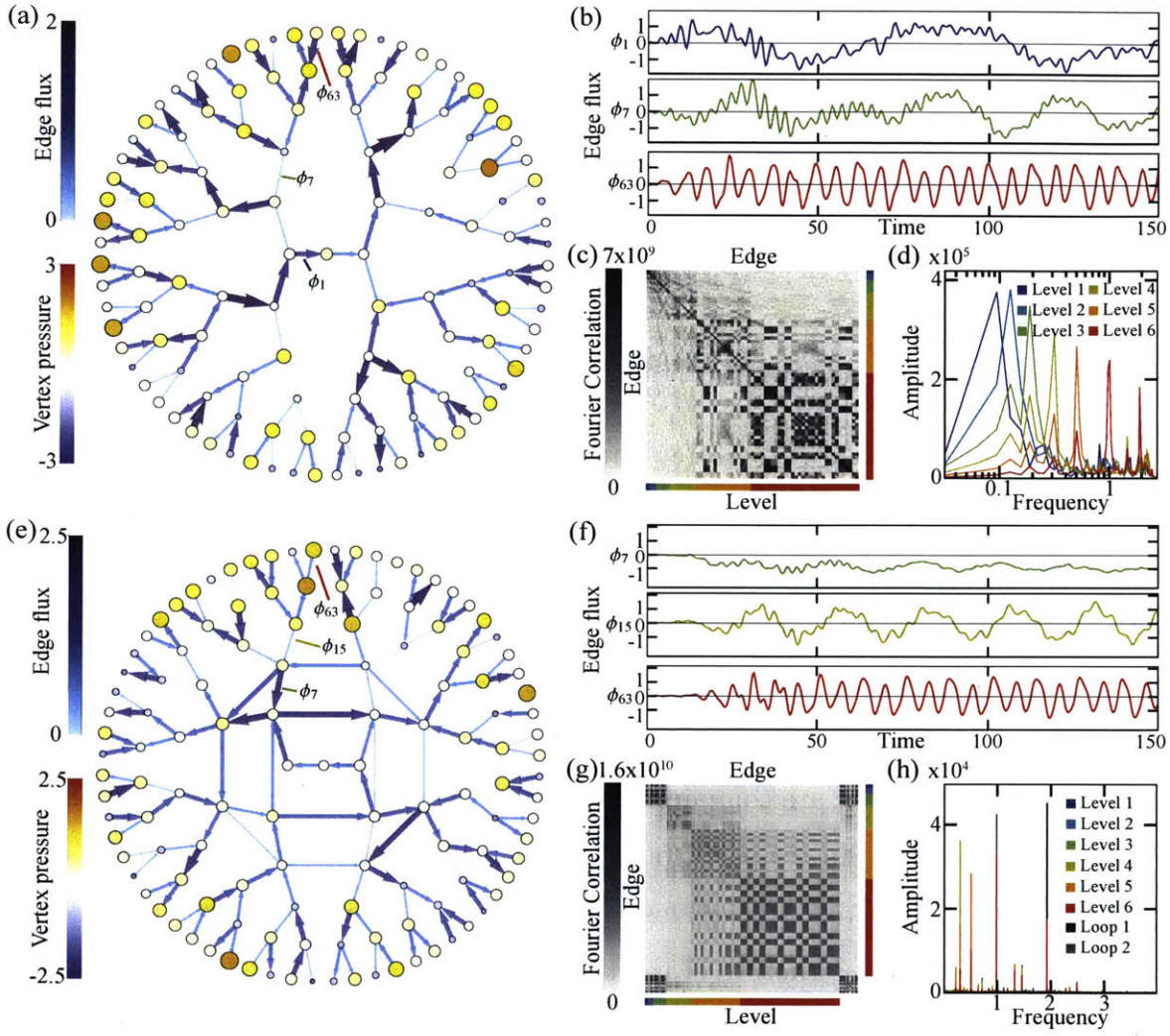

Figure 3-8: Activity causes depth-dependent separation of time scales on a large tree. (a) Most pressure variation occurs near the leaves on large binary trees. (b) The tree in (a) develops an activity-driven steady state with slow oscillations in the center and fast oscillations near the edges, as illustrated by the flux ϕ_e on the three edges labelled in (a). (c) Unnormalized correlations between the Fourier transforms of the flux through the edges of the tree in (a), with phases ignored. Colors indicate the tree level of the tail vertex of the edge. There are strong correlations within each level and between neighboring levels, but low correlations for edges in widely-separated levels. (d) Frequency spectra of each tree level, computed by taking Fourier transforms of the edge fluxes as in (c) and averaging the magnitudes across all edges at each level. A distinct primary oscillation frequency for each level can be seen, which increases with distance from the tree center. Simulation parameters in all panels are $\epsilon = 0.5$, $\mu = 1$, and $D = 10^{-3}$. (e-h) While adding edges in the center leads to steady flow on cycles there, frequency still increases with distance from the center in the outer, tree-like sections.

except for the simplest two-state systems [59].

Nevertheless, long simulation runs as shown in Fig. 3-9 offer some insight into the qualitative behavior of attractors in active flow networks. Specifically, our simulations suggest that, while there is considerable variation in the relative occupancy of different attractors, stable states can be approximately divided in two classes: (1) states with one high energy mode at high amplitude and a few low energy modes at low amplitude and (2) states with multiple low-energy modes active at moderate amplitude, some of them degenerate. States of type (2) tend to quickly transition to other states of type (2) (Fig. 3-9); states of type (1) have a wide range of lifetimes but no obvious transition patterns.

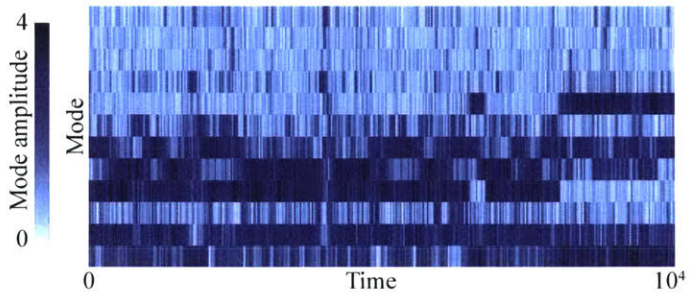

Figure 3-9: Lower energy modes transition more often for the graph in Fig. 3-6. Modes are ordered by frequency from high (top) to low (bottom). Simulation parameters are $\epsilon = 0.5$, $\mu = 1$, $D = 5 \times 10^{-3}$, identical to those in Fig. 3-6. Note that rows 7 and 8, the two modes that switch on and off most, are degenerate.

3.4.2 Networks with cycles

We focus on tree networks in this paper as they allow substantial analytical progress. However, Eqs. (3.1) can be applied without modification to networks with cycles. Cycles correspond to right singular vectors ϕ_n of $\nabla^\top$ with singular value zero. As these are always degenerate, we expect the conclusions of Section 3.2.3 to be most accurate when there are few or no cycles. Alternatively, on a weighted graph where the edges of high conductance form a tree, the attractor characteristics will be similar to the attractors on that tree (Fig. 3-2; all modes pictured in Fig. 3-3).

Qualitatively, we find the same stochastic switching between states with subsets

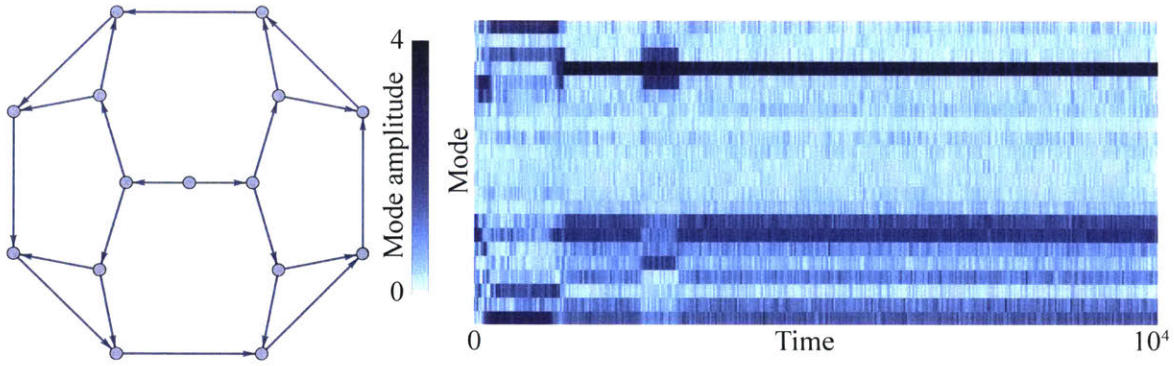

Figure 3-10: States on graphs with cycles, like the one shown, tend to be more stable. Modes are ordered by frequency from high (top) to low (bottom). Note that the eight modes at the bottom, which are the only ones active in the lower half of the trace, are all cycles. Simulation parameters are $\epsilon = 0.5$, $\mu = 1$, $D = 5 \times 10^{-3}$.

of modes active in simulations of Eqs. (3.1) on cyclic graphs even with equal weights, with the additional feature that cyclic modes are particularly stable and take longer to transition on average (Fig. 3-10). If the dynamics of the cycles themselves are of interest, the incompressible analysis of Chapter 2 may be more appropriate.

3.4.3 Band gaps

In addition to distinct activity levels μ_e across edges, we can also introduce edge weights w_e or vertex weights m_v that vary across the network. Changing the conductances w_e and volumes m_v changes our system in two ways: first, by changing the modes to the singular vectors of ∇^*_{ve}; and second, by changing the coupling matrix to

$$\tilde{P}_{mk} = \tfrac{3}{2}(1 - \tfrac{1}{2}\delta_{mk}) \sum_e w_e^{-1} \phi_{em}^2 \phi_{ek}^2, \tag{3.29}$$

which depends explicitly on the edge weights.

Such changes are known to cause qualitative changes in the physics of classical spring-mass networks, including the introduction of band gaps. In an infinite one-dimensional line of beads of equal mass m connected by springs with equal spring constant f, for example, the dispersion relation between frequency ω and wavenum-

ber q is

$$\omega(q) = 2\sqrt{\frac{f}{m}}\left|\sin\left(\frac{qa}{2}\right)\right|,$$

where a is the size of the unit cell, in this case equal to distance between adjacent beads [93]. If instead of equal masses the beads alternate between a smaller mass m_1 and larger mass m_2, the dispersion relation splits into two branches,

$$\omega(q)_{\pm}^2 = f\left(\frac{1}{m_1}+\frac{1}{m_2}\right) \pm f\sqrt{\left(\frac{1}{m_1}+\frac{1}{m_2}\right)^2 - \frac{4}{m_1 m_2}\sin^2\left(\frac{qa}{2}\right)}.$$

Here a unit cell has two beads, so the distance between beads is $a/2$. At $q = \pi/a$, there is a gap between $\omega_+ = \sqrt{2f/m_1}$ and $\omega_- = \sqrt{2f/m_2}$. This band gap shows up in a finite system as a large difference in frequency between modes above and below the gap.

Since varying what are effectively vertex weights causes such a clear qualitative change in behavior in the spring system, we can reasonably expect similar changes in our model. Simulations on paths with alternating vertex weights show a distinct separation of of low- and high-energy states not present with uniform weights (Fig. 3-11), with stronger and more consistent suppression of the low-energy states and few transitions across the band gap created by nonuniform weights. Band gaps in more realistic topologies may have similar effects, allowing for enhanced control of the large-scale behavior.

3.5 Conclusions

Beyond active density oscillations [102], the above theoretical framework can be used to probe the effects of topology on the physical properties of complex active systems. For instance, it was recently shown that continuum Toner–Tu systems in finite lattice confinement possess topologically protected edge-localized sound modes [124]. Similar edge modes can be reproduced in our coarse-grained model through a simplified

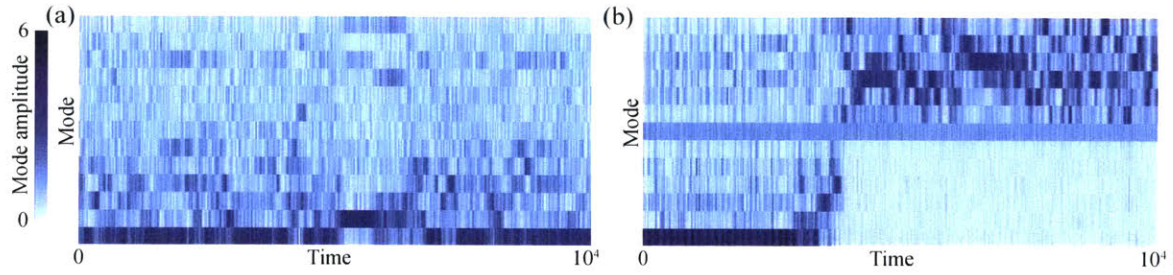

Figure 3-11: The emergence of an activity-driven spectral band gap is exhibited by a simulation on a 14-vertex path with (a) all weights equal to 1 and (b) alternating vertex weights 1 and 5. Modes are ordered by frequency from high (top) to low (bottom). Note that in (b) the central $n = 7$ mode is always active and the low energy states on the right half of the plot are significantly more suppressed than they ever are in (a). The qualitative difference is due to the presence of vertices with unequal weights, not the overall scale of the vertex weights; changing vertex weights uniformly is equivalent to rescaling other parameters. Parameters are $\mu = 1.2$, $D = 5 \times 10^{-3}$, and $\epsilon = 0.5$. Both simulations used the same random seed.

network representation of complex channel geometries (Fig. 3-1). In addition, generalizing to allow different effective weights at vertices opens up band gaps, reflected in the excitation spectrum of spontaneous activity modes (Fig. 3-11). As we focus on phenomenological properties shared by many active systems, akin to the Toner–Tu approach [133], the results and techniques presented here promise insights into the mode selection mechanisms governing a wide range of non-equilibrium transport and force networks.

Chapter 4

Designing spectra

Complex real-world phenomena across a wide range of scales, from aviation and internet traffic to signal propagation in electronic and gene regulatory circuits, can be efficiently described through dynamic network models. In many such systems, the spectrum of the underlying graph Laplacian plays a key role in controlling the matter or information flow. Spectral graph theory has traditionally prioritized analyzing unweighted networks with specified adjacency properties. Here, we introduce a complementary framework, providing a mathematically rigorous weighted graph construction that exactly realizes any desired spectrum. We illustrate the broad applicability of this approach by showing how designer spectra can be used to control the dynamics of various archetypal physical systems. Specifically, we demonstrate that a strategically placed gap induces chimera states in Kuramoto-type oscillator networks, tunes or suppresses pattern formation in a generic Swift-Hohenberg model, and leads to persistent localization in a discrete Gross-Pitaevskii quantum network. Our approach can be generalized to design continuous band gaps through periodic extensions of finite networks.

4.1 Discrete band gaps

Spectral band gaps control the behavior of physical systems in areas as diverse as topological insulators [23, 60], phononic crystals [122], superconductors [13], acoustic

metamaterials [139], and active matter [124]. In addition to ubiquitous physical network models [19, 119, 123, 130] ranging from aviation [25] to electronics [36], there is also considerable interest in virtual or computational networks [151] with fewer physical constraints, such as those recently used to create spiral wave chimeras in coupled chemical oscillators [134]. Often, dynamics in such systems depend on the graph Laplacian [87, 96] and in particular on its spectrum of eigenvalues. Traditionally studied in periodic lattice graph models [79, 122, 124, 139] and more recently also in hyperuniform systems [82], the targeted design of spectra of any desired shape remains a major challenge in modern materials science [58, 139]. Recent breakthroughs in 3D printing [18, 52, 61, 138] and lithography [29] make it possible now to produce and explore network structures that go beyond the traditionally considered periodic lattice geometries.

Building on such experimental and theoretical progress, we present here a mathematically rigorous solution to the longstanding question of how any desired spectrum can be realized exactly on a suitably designed positively-weighted network. In particular, our construction of networks with specified eigenvalues allows us to place arbitrary gaps in the spectrum of the network Laplacian

$$L = D - A, \tag{4.1}$$

where D and A are the weighted degree and adjacency matrices respectively. These gaps, finite analogs to band gaps in continuous systems, enable precise control over the dynamics in a wide range of graph-based physical systems. To follow the analogy, we will name an eigenvalue-free region in our finite networks that is comparable to the range of eigenvalues a discrete band gap (DBG). In a strict sense band gaps can only exist in an extended system with continuous energy bands, and so we also show how to create continuous band gaps by tiling our DBG construction periodically (Section 4.4). Designing a suitably weighted network topology in this way presents an alternative to control procedures based on adjusting model parameters or initial conditions on a given network [94]. The spectral approach towards functional control

of network dynamics proposed here can, for example, be directly implemented with recently developed computer-coupled oscillator setups [134] and may find future applications in networked optical lattices [22, 34, 54, 98] and superconducting waveguide resonators [71].

We motivated the general problem from a broader physics perspective in Section 1.2. Here, after summarizing and explaining the main mathematical result (Section 4.2), we focus on demonstrating its broad applicability explicitly for classical and quantum systems, by showing how suitably placed DBGs can induce chimera states [86, 101] in oscillator networks, control structural growth in pattern formation models, and facilitate state localization in quantum networks (Section 4.3). In parallel, we illustrate how our exact spectral construction can be combined with sparsification algorithms [68, 125] to yield simplified networks preserving DBGs. This approach complements the more traditional procedure of constructing graph ensembles with predefined statistical adjacency characteristics [5, 8, 12, 106]. Finally, we discuss periodic extensions of finite networks as a systematic procedure for designing continuous band gaps (Section 4.4).

4.2 Network construction and sparsification

The problem of recovering a network from its eigenvalues has been studied extensively, both from an algorithmic [38, 40, 64] and mathematical [57, 88] perspective. However, with a few limited exceptions [57], most prior work has focused only on unweighted networks [135], where there are a finite number of graphs on n vertices and thus only a finite number of possible spectra. We here construct an exact solution for the weighted case.

4.2.1 Spectral graph construction

Our main result is that, given a set $\{\lambda_i\}$ of desired eigenvalues ordered so

$$\lambda_1 \geq \ldots \geq \lambda_{n-1} \geq \lambda_n = 0, \tag{4.2}$$

there is a weighted graph G on n vertices with non-negative edge weights whose Laplacian has spectrum $\lambda_1, \ldots, \lambda_{n-1}, 0$. We will denote this Laplacian as L^* to distinguish from a generic Laplacian L. The Laplacian, which determines the graph, can be reconstructed from its eigenvalues and eigenvectors with the eigenvalue decomposition; we therefore need to find a set of eigenvectors that together with $\{\lambda_i\}$ give a graph Laplacian. In fact, the same set of eigenvectors $v^{(k)}, k = 1, \ldots, n-1$, given by

$$v_i^{(k)} = \begin{cases} \frac{1}{\sqrt{k(k+1)}} & i < k+1 \\ -\frac{k}{\sqrt{k(k+1)}} & i = k+1 \\ 0 & i > k+1 \end{cases} . \tag{4.3}$$

suffices for any spectrum. These eigenvectors are strongly localized: the inverse participation ratio (4-norm)

$$\left\|v^{(k)}\right\|_4^4 = 1 - 2k^{-1} + O(k^{-2}) \tag{4.4}$$

indicates near-perfect localization $\left\|v^{(k)}\right\|_4^4 \to 1$ for almost all k, itself a desirable phenomenon [96, 108] which we will exploit later in the context of pattern formation. As the $v^{(k)}$ are mutually orthonormal and orthogonal to the vector of all ones, the matrix

$$L^* = \sum_{k=1}^{n-1} \lambda_k v^{(k)} v^{(k)\top} \tag{4.5}$$

has the desired spectrum with $\frac{1}{\sqrt{n}}\mathbf{1}$ as the final eigenvector for $k = n$ with eigenvalue zero. By explicitly computing the sum over k for $i < j$, we find that the elements of

the designed L^* above the diagonal, L^*_{ij} for $i < j$, are given by

$$\begin{aligned} L^*_{ij} &= \sum_{k=1}^{n-1} \lambda_k u_i^{(k)} u_j^{(k)} \\ &= \lambda_{j-1} u_i^{(j-1)} u_j^{(j-1)} + \sum_{k=j}^{n-1} \lambda_k u_i^{(k)} u_j^{(k)} \\ &\leq \lambda_{j-1} \left[-\frac{1}{j} + \sum_{k=j}^{n-1} \frac{1}{k(k+1)} \right] \\ &= \lambda_{j-1} \left(-\frac{1}{j} + \frac{1}{j} - \frac{1}{n} \right) \\ &= -\frac{\lambda_{j-1}}{n} \leq 0, \end{aligned} \tag{4.6}$$

that is, that the off-diagonal elements of L^* are all nonpositive; L^* therefore corresponds to a graph with nonnegative weight $-L^*_{ij}$ between vertices i and j. From the second to third lines of Eq. (4.6) we use the definition of the eigenvectors in Eq. (4.3); the sum

$$\sum_{k=j}^{n-1} \frac{1}{k(k+1)} = \frac{1}{j} - \frac{1}{n} \tag{4.7}$$

in the third line can be computed as a telescoping sum of partial fractions. $L*$ is symmetric, so the elements below the diagonal must also be nonpositive. This proves that the edge weights of the constructed graph are nonnegative. If all of the eigenvalues are nonzero, all of the off-diagonal elements of $L*$ will be nonzero and the resulting graph will be complete.

Some spectra can only be realized on complete graphs. A graph G with approximately constant spectrum must be complete: if a generic Laplacian L has nonzero eigenvalues $\lambda_k = \lambda + \epsilon_k$ for $k < n$ and $\lambda_n = 0$, then

$$\lambda I - L = \frac{\lambda}{n} \mathbf{1}\mathbf{1}^\top - \sum_{k=1}^{n-1} \epsilon_k v^{(k)} v^{(k)\top}.$$

The off-diagonal elements of $\lambda I - L$, which equal the original edge weights of G, are therefore $\frac{\lambda}{n} + O(\epsilon)$. For small ϵ_k, every edge has nonzero weight; if $\epsilon = 0$, we have that

the complete graph with equal weights is the only network with a fully degenerate spectrum. More commonly, the network that realizes a spectrum is not unique. For example, if there are k zero eigenvalues, then we can partition the eigenvalues into k groups each containing one zero. The disjoint union of graphs constructed to have each group's spectrum will have the full desired spectrum. If there is more than one nonzero eigenvalue and $k > 1$, there will be multiple partitions that give nonisomorphic graphs; typically, this construction will give an enormous number of isospectral disconnected graphs.

For connected graphs, with only one zero eigenvalue, our construction also shows that the spectrum of any non-complete weighted graph cannot uniquely specify that graph, in line with older results on, for example, the spectra of trees [88]. Given any connected graph with at least one missing edge, our design can match the spectrum with a complete graph that cannot be isomorphic to the given one. In fact, since we have $\binom{n}{2}$ parameters (the edge weights) and only $n-1$ constraints (the eigenvalues, excluding the trivial 0 eigenvalue), there can be a continuous $\binom{n}{2} - n + 1$ parameter family of isospectral graphs near our construction. We will investigate this family further in future work, including its possible application to sparsification.

Controlling the eigenvalues allows us to create networks with precisely specified gaps. For instance, choosing

$$\lambda_1 = \lambda_2 = \ldots = \lambda_{n/2-1} \tag{4.8}$$

and

$$\lambda_{n/2} = \lambda_{(n/2)+1} = \ldots = \lambda_{n-1} \tag{4.9}$$

with n even leads to a graph with edge weights

$$-L^*_{ij} = \lambda_{n-1}/n \tag{4.10}$$

if $i > n/2$ or $j > n/2$ and

$$-L^*_{ij} = (2\lambda_1 - \lambda_{n-1})/n \tag{4.11}$$

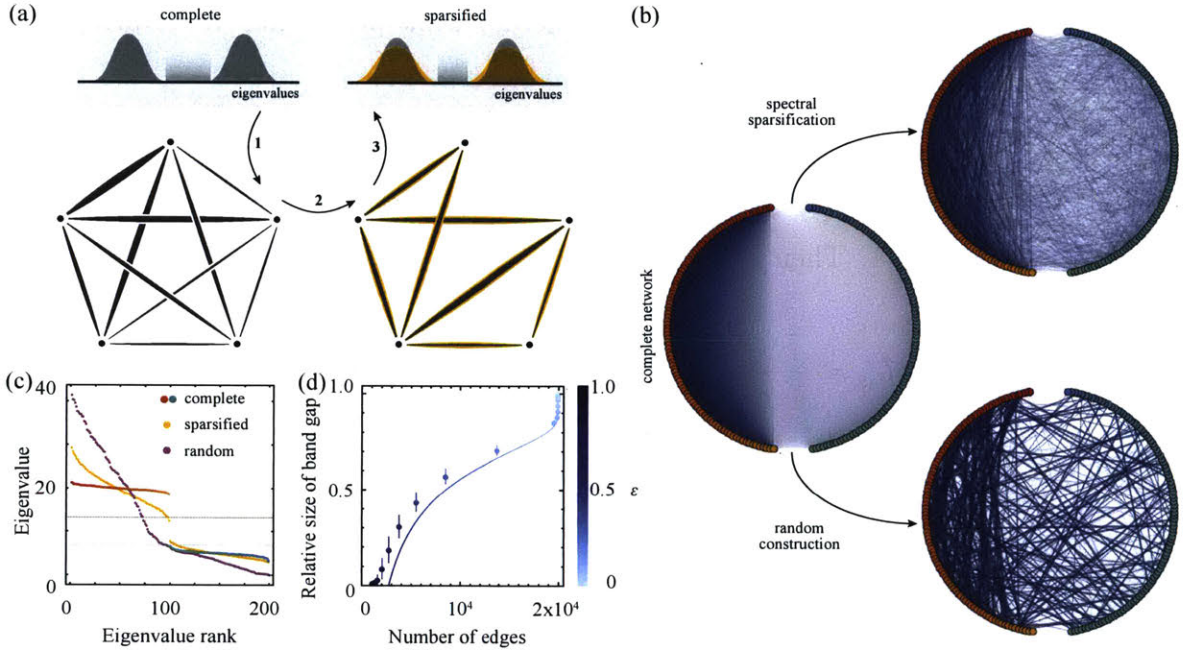

Figure 4-1: Designing networks from spectra. (a), Schematic of DBG network construction. Given a spectrum of eigenvalues distributed in two (or more) groups, we build a graph with non-negative edge weights that realizes this spectrum exactly (1). Sparsification of this complete DBG network with the Spielman-Srivastava [125] algorithm (2) yields a new network with wider eigenvalue distributions and a smaller gap (3). (b), Example graphs used in applications below: Starting from a DBG graph on 200 vertices with 100 eigenvalues set to i.i.d. $\mathcal{N}(5, 0.25)$ and 99 set to i.i.d. $\mathcal{N}(20, 0.25)$ (left), sparsification with $\epsilon = 0.5$ creates a new graph (top) with the number of edges reduced from 19900 to 3758. As a control, we also compare to a gapless random graph (bottom) with 362 edges and the same weighted vertex degrees as the original DBG graph. (c), The eigenvalues for the graphs in (b). The mode on the complete DBG network with the k-th largest nonzero eigenvalue is supported on the first $k+1$ vertices, counted counterclockwise from the top red vertex, and highly localized on vertex $k+1$, which is colored to match in (b). Grey lines indicate the borders of the unstable region for the Swift-Hohenberg model with the parameters used in Fig. 4-3. (d), Sparsified networks retain a significant gap even for relatively large ϵ. Each point shows the mean number of edges and gap size at fixed ϵ between 1 (left) and 0.01 (right), starting from a graph on 200 vertices designed to have 100× eigenvalue 5 and 99× eigenvalue 20. The solid curve shows the worst-case gap estimate, reduction by a factor $1 - \frac{5}{3}\epsilon$. Sample size is 1000 for $\epsilon \geq 0.1$ and 300 for $\epsilon < 0.1$. Error bars are ± 1 standard deviation; horizontal error bars are smaller than the marker size.

otherwise; that is, there are two groups of vertices, one strongly connected within itself and one weakly connected to everything. Adding a small amount of noise to each eigenvalue then lifts the eigenvalue degeneracy while preserving the connectivity structure and retaining a gap (Fig. 4-1b,c).

In detail, suppose we have eigenvalues λ_1 with multiplicity m and $\lambda_{n-1} < \lambda_1$ with multiplicity $n - m - 1$. Then if $i < j \leq m + 1$

$$\begin{aligned} L^*_{ij} &= -\frac{\lambda_1}{j} + \sum_{k=j}^{m} \frac{\lambda_1}{k(k+1)} + \sum_{k=m+1}^{n-1} \frac{\lambda_{n-1}}{k(k+1)} \\ &= -\frac{\lambda_1}{m+1} + \lambda_{n-1}\left(\frac{1}{m+1} - \frac{1}{n}\right). \end{aligned}$$

Else, if $i < j$ and $j > m + 1$,

$$L^*_{ij} = \lambda_{n-1}\left[-\frac{1}{j} + \sum_{k=j}^{n-1} \frac{1}{k(k+1)}\right] = -\frac{\lambda_{n-1}}{n}.$$

There are two types of edges: edges with both endpoints in the first $m + 1$ vertices have weight $\lambda_{n-1}/n + (\lambda_1 - \lambda_{n-1})/(m + 1)$, while other edges have weight λ_{n-1}/n.

4.2.2 Sparsification

Since complete graphs can be difficult to realize physically, we explore the effect of the sparsification-by-resistances algorithm developed by Spielman and Srivastava [125]. Given an accuracy parameter ϵ, this sparsification creates a network with $O((n \log n)/\epsilon^2)$ edges whose eigenvalues match the eigenvalues of the original network to within a multiplicative factor $1 \pm \epsilon$ with high probability. Sparsification by resistances aims to preserve the entire spectrum, not just a gap; future sparsification algorithms directly constructed to preserve a gap could therefore improve on its efficiency. In other applications, the networks of interest are virtual ones [134] and sparsification may not be necessary.

Rather than removing edges from the initial graph, the sparsification algorithm

constructs a new graph starting from disconnected vertices. Specifically, we first compute the effective resistance R_{ij} between every pair of vertices in the initial graph, treating the edge weights as conductivities. We then sample $q = (n \log n)/\epsilon^2$ edges at random, with the probability p_{ij} of sampling edge (i, j) proportional to $w_{ij}R_{ij}$. Each edge we sample is added to the sparsified graph with weight $w_{ij}/(qp_{ij})$; if an edge is added multiple times, the weights are summed. Clearly, the new graph will have at most q edges. We leave the argument that this preserves the spectrum to Ref. [125].

We can use the $1 \pm \epsilon$ multiplicative error bound to estimate the size of a discrete band gap after sparsification. Suppose we start from a network with eigenvalues λ_1, λ_2, and 0, with some multiplicities, where $\lambda_1 > \lambda_2$. The eigenvalues $\{\mu_i\}$ of the sparsified graph corresponding to λ_1 should be no smaller than $\mu_i \geq (1 - \epsilon)\lambda_1$, while the eigenvalues $\{\nu_i\}$ corresponding to λ_2 should be no larger than $\nu_i \leq (1 + \epsilon)\lambda_2$. The sparsified graph should therefore have a gap $\Delta = \min_i \mu_i - \max_i \nu_i$ of size

$$\Delta \geq \left(1 - \frac{\lambda_1 + \lambda_2}{\lambda_1 - \lambda_2}\epsilon\right)(\lambda_1 - \lambda_2).$$

That is, the gap contracts by a factor at most $1 - \frac{\lambda_1+\lambda_2}{\lambda_1-\lambda_2}\epsilon$. For the parameters used in Fig. 4-1d, this is $(1 - \frac{5}{3}\epsilon)$.

4.3 Applications

We now demonstrate the practical potential of DBGs with three generic network models. In each case, we compare the dynamics on a complete DBG network (Fig. 4-1b, left) both to a sparsified approximate DBG network (Fig. 4-1b, top) and to a random connected network (Fig. 4-1b, bottom) constructed to have the same weighted vertex degrees as the DBG network (Section 4.3.1). The gap is approximately preserved in the sparsified network and vanishes entirely in the random graph (Fig. 4-1c,d). Matching the degrees in the random graph to the DBG network ensures that any differences in dynamics are not due to differences in coarse features like the average

connectivity, but rather are likely caused by the spectral differences. Often, the behavior of optimized networks is sensitive to small perturbations [100]; here, behaviors preserved in the sparsified graph are robust to significant changes.

Laplacian matrices occur in a wide range of physical systems, in many of which, like the spring networks and random walks mentioned earlier, the effect of the spectrum and band gaps is known. In other models, gaps can have significant but less well-understood effects. We have chosen three nonlinear models to investigate in more detail in order to illustrate the diversity of potential applications for this work. These three systems are each generic, widely studied, and show distinct nontrivial effects of gapped spectra.

First we will discuss the Kuramoto model of coupled phase oscillators, typically studied as a model for synchronization. Here the Laplacian straightforwardly determines the linear behavior near synchronization and has a complex relationship with the nonlinear dynamics. Next we will present a discretized Swift-Hohenberg type pattern forming system, where controlling the Laplacian spectrum directly controls the steady states of a nonlinear equation. Finally, to diversify our range of physical applications, we will integrate our networks in a quantum mechanical model based on the Gross-Pitaevskii equation. Band gaps in such energy-conserving systems can inhibit transfer of energy between different modes, and we will see how this can tune diffusion of the wavefunction.

A natural question in the context of the previous two chapters is what happens when the DBG networks are put in the active flow models. Sadly, there are few exciting developments. These constructed networks are complete, so they are very far from planar and there are a large number of cycles that dominate the flow even in the compressible case. Meanwhile, in the incompressible setting, flow states with most edges at their desired flux are common. With relatively few frustrated edges, transitions are relatively rare.

Simulations for the applications were performed using a third or fourth order Adams-Bashforth linear multistep method with a time step $\Delta t = 10^{-4}$. All simulations were written in C++ using Armadillo [120].

4.3.1 Random matched-degree graphs

Given a weighted graph G, we can construct a random simple graph $\tilde{G}$ with the same vertex degrees as G in a way analogous to known methods for sampling random regular graphs [89]. Let $w(e)$ denote the weight of edge e and $d(v)$ denote the weighted degree of vertex v. Begin with a disconnected graph with a loop of weight $d(v)/2$ at each vertex v; this has the same degrees as G but is not simple. Repeat the following steps until there are no loops:

1. Pick a loop $l = (u, u)$ and another edge $e = (v, w)$ at random, with $v \neq u \neq w$.
2. (a) If $w(l) > w(e)$, remove e and add $e' = (u, v)$ and $e'' = (u, w)$ with weight $w(e)$. Subtract $w(e)$ from the weight of l.

   (b) Else, remove l and add $e' = (u, v)$ and $e'' = (u, w)$ with weight $w(l)$. Subtract $w(l)$ from the weight of e.

Once there are no more loops, merge all sets of edges between the same pair of vertices into one edge with the same total weight. Since the degree of each vertex is preserved at each step, the final graph has the same degrees as G. In the examples considered here, the algorithm terminates quickly.

4.3.2 Kuramoto oscillators

Our first application is the Kuramoto model of coupled oscillators [74, 127]. Introduced by Kuramoto in 1975, it has since been studied extensively as a generic setting for interesting synchronization behavior. One of the more surprising discoveries was the existence of chimera states [75], where sets of identical oscillators divide into coexisting synchronized and desynchronized clusters. Commonly considered in networks with identically-coupled oscillators, chimeras or chimera-like states can also appear with asymmetric couplings [66]. So far, relatively little attention has been paid to the effect of the spectrum of the coupling network, or, in particular, to what effect a gapped spectrum should have.

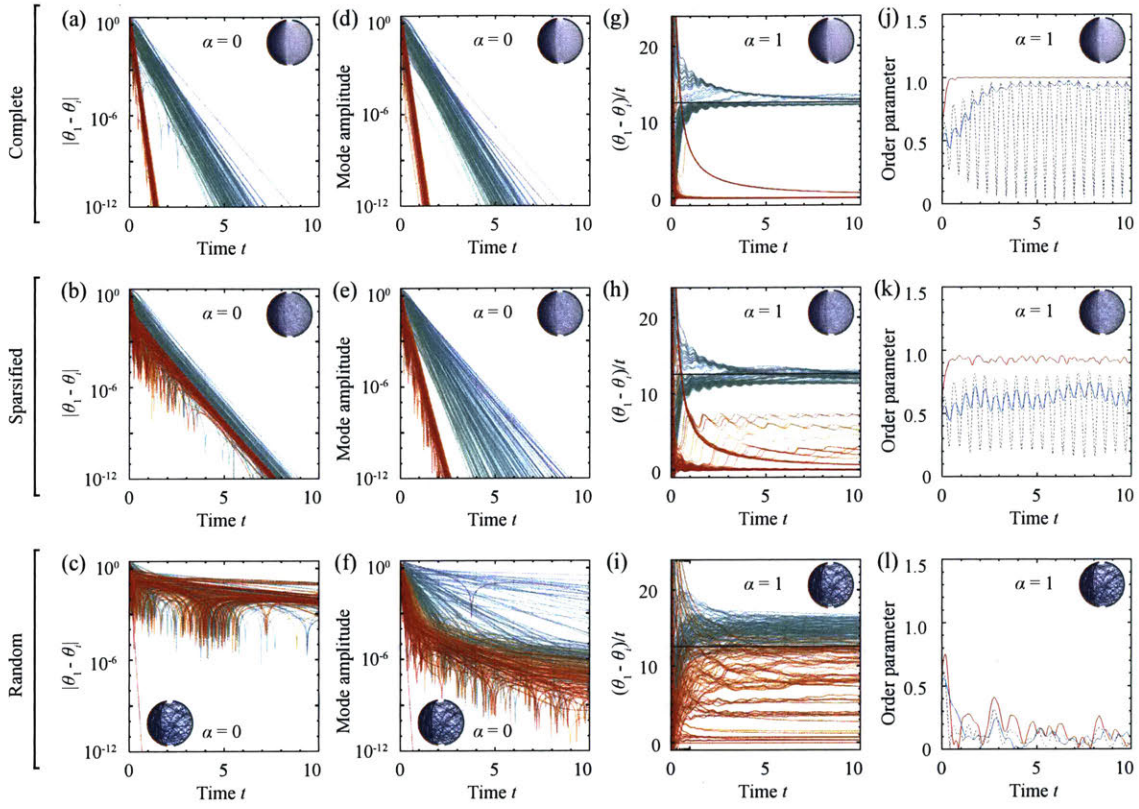

Figure 4-2: DBG networks lead to staggered synchronization and chimeras. (a-f), In the Kuramoto model with $\alpha = 0$, the complete (first row) and sparsified (second row) graphs synchronize much faster than the random graph (third row). For the complete graph the gap affects the rate of synchronization, with highly-connected vertices synchronizing faster (a), while on the sparsified graph the gap is only visible in the mode basis (e). (g-i), Weak chimera states appear when $\alpha = 1$. Both the complete (g) and sparsified (h) graphs have two dominant groups of phase-locked oscillators, with the complete graph more fully synchronized. Dynamics on the random graph (i) are much less coherent. Solid black lines indicate the predicted approximate frequency difference for a network with two distinct eigenvalues, 5 and 20. (j-l), Order parameter $r = |\sum_j e^{i\theta_j}|$ for the simulations in (g-i) for the strongly-connected vertices (red), weakly-connected vertices (teal), and all vertices (gray).

Recent experiments coupling Belousov-Zhabotinsky reactions via a computer-controlled projector have shown the emergence of chimeras [134]; we will show this can be achieved in the weak sense of Ref. [9] using our construction with an appropriately gapped spectrum. In the Kuramoto model phases θ_i on the vertices evolve with a natural frequency ω and a nonlinear coupling defined by the network adjacency matrix:

$$\frac{d\theta_i}{dt} = \omega + \sum_{j=1}^{n} A_{ij} \sin(\theta_j - \theta_i + \alpha). \tag{4.12}$$

On a connected graph with $\alpha = 0$, there is always a stable attractor $\theta_i = \theta_0 + \omega t$. The rate of convergence to this state within its basin of attraction is controlled by the eigenvalues of the Laplacian L [87]: if we linearize to $\sin(\theta_j - \theta_i) \approx \theta_j - \theta_i$ then perturbations p to the stable attractor will follow Eq. (1.1). Both the complete and sparsified example graphs in Fig. 4-1 have no eigenvalues near zero, so they synchronize much faster than the random graph (Fig. 4-2a-c). The rescaled spectral gap λ_{n-1}/λ_1 is sometimes called the synchronizability of the network [100]: for a fixed average connectivity, networks with lower synchronizability will typically have more disordered dynamics. The other gap between the two large clusters of eigenvalues divides the modes into two groups, one synchronizing faster than the other (Fig. 4-2d-e); moreover, on the complete graph, the localization of the eigenvectors causes staggered synchronization of vertices (Fig. 4-2a).

If α is sufficiently large, the oscillators no longer synchronize at a single frequency. On DBG networks, global coherence gives way to weak chimera states [9] where vertices synchronize into two clusters with distinct frequencies (Fig. 4-2g-i). For the exactly-gapped network with edges of weight $w_1 = \lambda_{n-1}/n + (\lambda_1 - \lambda_{n-1})/(m+1)$ or $w_2 = \lambda_{n-1}/n$ there is a steady state with $\theta_i = \theta_1$ for $i \leq m+1$ and $\theta_i = \theta_n$ for $i > m+1$. In this state,

$$\frac{d}{dt}(\theta_n - \theta_1) = [nw_2 - (m+1)(w_1 + w_2)] \sin(\alpha) - nw_2 \sin(\theta_n - \theta_1 + \alpha). \tag{4.13}$$

The two phases θ_1 and θ_n can synchronize only if there is a solution to

$$\sin(\theta_n - \theta_1 + \alpha) = \left[1 - 2\frac{m+1}{n} - \left(\frac{\lambda_1}{\lambda_{n-1}} - 1\right)\right] \sin(\alpha). \tag{4.14}$$

This synchronization is possible if α is small enough that the right hand side is less than one. If the two groups do not synchronize, and $nw_2 = \lambda_2$ is not too large, the second r.h.s. term in Eq. (4.13) will average to nearly zero giving an approximate mean frequency difference

$$\left\langle \frac{d}{dt}(\theta_n - \theta_1) \right\rangle \approx [nw_2 - (m+1)(w_1 + w_2)] \sin(\alpha), \tag{4.15}$$

which reduces to

$$\left\langle \frac{d}{dt}(\theta_n - \theta_1) \right\rangle \approx -(\lambda_1 - \lambda_{n-1}) \sin(\alpha) \tag{4.16}$$

if $m + 1 = \frac{n}{2}$ as in Fig. 4-2. More general cluster synchronization [35, 105] could be achieved by adjusting the number and size of the gaps. In contrast, the random graph becomes thoroughly incoherent at comparable values of α (Fig. 4-2i,l). The coherence can be quantified by the order parameter

$$r = \left| \sum_j e^{i\theta_j} \right|, \tag{4.17}$$

which oscillates for the complete and sparsified networks but is near zero for the random graph (Fig. 4-2j-l), indicating complete disorder.

The result of our construction with a DBG is similar to a standard two-cluster model where chimeras appear [101]. In this model, vertices are divided into two groups of size $n/2$ with edge weight $-L_{ij} = \mu$ if i and j are in the same cluster and $-L_{ij} = \nu < \mu$ if i and j are in different clusters. In the limit $n \to \infty$, this system exhibits stable chimera states with one cluster synchronized and the other cluster incoherent. However, for our DBG network, we relax the assumptions that intra-cluster couplings μ are identical and stronger than inter-cluster couplings ν. Perhaps surprisingly,

oscillators on the weakly-connected side are consistently closer to synchronizing with each other than with strongly-connected oscillators, even though the coupling among weakly-connected vertices is smaller than the coupling between weakly- and strongly-connected vertices. Ours are weak chimeras, where we do not require one cluster to be incoherent, but they exist stably on small networks.

The effect appears more related to the gap than to the degeneracy of the eigenvalues. The densely-connected side of the sparsified graph is mostly synchronized, even though the eigenvalues above the gap are no longer approximately degenerate. However, the spectrum is not the only determinant of behavior in the Kuramoto model. The classic simplest example of a gapped network, a periodic chain with alternating high- and low-weight edges, does not synchronize in clusters so simply.

This could be realized experimentally in any Kuramoto-type system where the connectivity is controlled. For example, our networks could be input directly into the chemical oscillator system of Ref. [134] where the authors found spiral-wave chimeras.

4.3.3 Swift-Hohenberg pattern formation

As the second application, we study Swift-Hohenberg pattern formation dynamics on a network [99, 129]. The Swift-Hohenberg equation (4.19) [129] is a common, generic model of pattern formation, intended to model the selection of patterns with a well-defined scale. It has been applied in areas well beyond the thermally-driven convection for which it was developed, ranging from wrinkling of elastic shells [126] to lasers [76]. Though originally defined in a continuous setting, the model can be easily extended to discrete network systems using the analogy between $-\nabla^2$ and L [99].

In contexts with a continuous, gapless spectrum of eigenvalues, the standard Swift-Hohenberg parameters define the length scales of the system. With a gap, however, there is an additional interaction between the length scales of pattern formation and the location of the gap. Just as acoustic band gaps can inhibit transmission of sound of particular frequencies [122], gaps in this system should inhibit pattern formation at the corresponding scales.

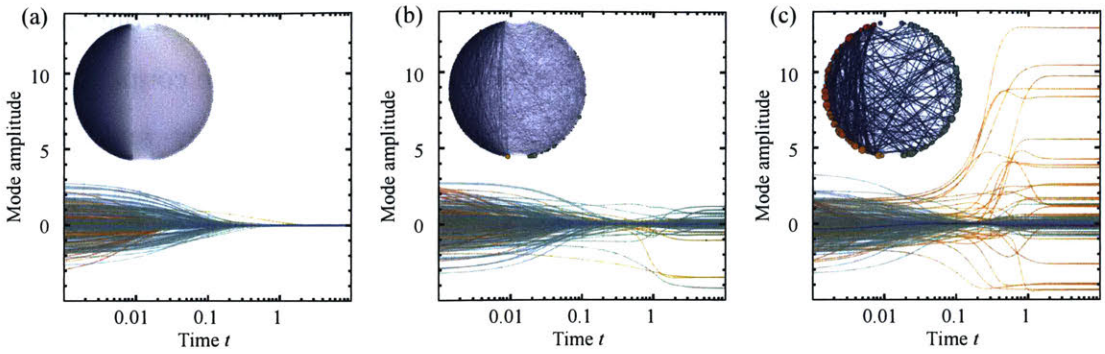

Figure 4-3: Generic suppression of pattern formation with a designed discrete band gap. (a), Pattern formation in the Swift-Hohenberg system is completely suppressed by constructing a gap around the range where eigenvalues would be unstable (Fig. 4-1c). (b), On a sparsified graph that has a few eigenvalues just within the unstable region, some modes settle at small nonzero values. (c), On the random graph many more eigenvalues are well within the unstable region and the corresponding modes settle at larger amplitudes. Inset graphs show the final steady state on each graph; the size of vertices corresponds to $|\phi|$. All simulations used identical initial conditions $u_i \sim \mathcal{N}(0,1)$ and parameters $\alpha = 90$, $D_1 = -20$, $D_2 = 1$.

Consider a scalar field ϕ_i on the vertices obeying

$$\frac{d\phi_i}{dt} = -D_1 \sum_{j=1}^{n} L_{ij}\phi_j - D_2 \sum_{j,k=1}^{n} L_{ij}L_{jk}\phi_k - \alpha\phi_i - \phi_i^3. \tag{4.18}$$

This is the discrete network equivalent to the usual continuous Swift-Hohenberg model [99, 129]

$$\partial\phi/\partial t = D_1\nabla^2\phi - D_2\nabla^4\phi - \alpha\phi - \phi^3; \tag{4.19}$$

the extra minus sign in front of the D_1 term in Eq. (4.18) arises from the adopted standard sign convention for the discrete graph Laplacian L. The fixed point $\phi_i = 0$ of Eq. (4.18), which exists for any values of the parameters D_1, D_2 and α, is linearly stable to perturbations in a Laplacian eigenmode with eigenvalue λ if the growth rate $\sigma \equiv -\alpha - D_1\lambda - D_2\lambda^2 < 0$. With α and D_2 positive, σ is negative for small and large λ, but choosing $D_1 < -2\sqrt{\alpha D_2}$ creates a range of unstable λ in between. This can drive pattern formation that is eventually stabilized by the nonlinearity. The patterns can only form, however, if L has eigenvalues in the unstable range. Controlling the spectrum of L^* therefore allows us to completely suppress pattern formation in

arbitrarily large systems by placing a gap around the unstable region (Figs. 4-1c, 4-3a). If we sparsify the network with sufficiently small ϵ, the gap will be preserved and again no patterns will form. Eventually, though, increased sparsification will push some eigenvectors into the edges of the unstable region and bring back partial pattern formation (Fig. 4-3b), which becomes fully developed in the random graph (Fig. 4-3c). The maximum ϵ for which patterns will be fully suppressed for given parameter settings can be predicted straightforwardly from the expected changes in the eigenvalues, in a similar fashion to the post-sparsification gap size in Fig. 4-1d.

Pattern suppression relies only on controlling the available eigenvalues. Our construction, however, has the additional desirable [96, 108] feature that the eigenvectors are highly localized. This allows us to control not just whether patterns form, but also which patterns appear. By choosing the eigenvalues of modes corresponding to a set S of vertices to lie inside the unstable range, while leaving all other eigenvalues outside of that range, we can selectively activate only the set S. While this only guarantees that the linear part of Eq. (4.18) selects the desired pattern, because the local nonlinearity only weakly couples different localized modes, the pattern typically survives in the nonlinear regime (Fig. 4-4).

Depending on initial conditions, vertices corresponding to eigenvalues above the unstable range may have small activations, since the activated modes have small but nonzero amplitudes there. With random initial conditions, however, positive and negative contributions from activated modes with opposite signs often nearly cancel yielding uniform patterns (Fig. 4-4e). Uniformity can also be achieved by having no eigenvalues above the unstable range or sufficiently many high eigenvalues that the amplitudes of the activated modes on those vertices is nearly zero. Alternatively, this phenomenon could be used to design more complex patterns with multiple levels of activation.

The conclusion that a band gap can suppress pattern formation does not depend on the discreteness of our system. Experimentally, then, it would be worth investigating both ways to realize a network Swift-Hohenberg model where our networks could be used directly and continuous Swift-Hohenberg systems where a band gap could

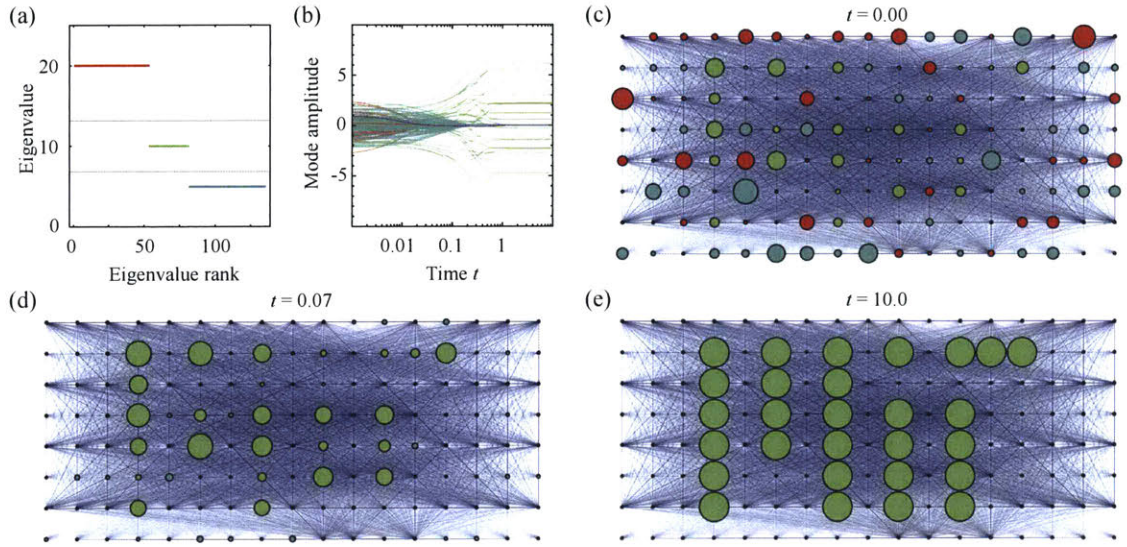

Figure 4-4: Controlling pattern formation with a designed discrete band gap. (a) Instead of placing a gap in the spectrum around the unstable pattern-forming range, as in Fig. 4-3, we deliberately place particular eigenvalues in the middle of that range corresponding to eigenvectors localised on a desired pattern. (b) From random initial conditions, the system settles into a state where only the chosen modes have nonnegligible amplitudes. (c–e) Time series of pattern evolution on a designed network, with vertices colored according to the stability of the mode localized there as in (a). The size of the vertices indicates $|\phi|$. (c) The encoded pattern is not obvious from either the designed network or the random initial conditions. (d) By time $t = 0.07$ the stable modes have nearly all vanished. (e) The steady state reveals the eigenmode-designed pattern. Because the modes are highly localized, selecting a set of modes to activate is approximately equivalent to selecting a set of vertices to activate. Thus we can encode an arbitrary pattern as the steady state. Depending on initial conditions, the system may settle into other stable states with slight variations in the vertex activations; the pattern is always identifiable and often as clear as shown. The parameters $\alpha = 90$, $D_1 = -20$, and $D_2 = 1$ are identical to those in Fig. 4-3; the tuning parameters to control pattern formation are only the network edge weights.

be introduced.

4.3.4 Gross-Pitaevskii localization

Having discussed two classical applications to non-conservative systems, we now show how DBGs can control quantum dynamics with conserved energy. In experiments with Bose-Einstein condensates (BECs) in optical lattices [54] researchers often approximate the continuous quantum state with a discrete wavefunction in the Bose-Hubbard model [28]. Similar Hamiltonians also combining Laplacian-like coupling with local potentials arise for the recently realized fermionic lattice gases [34, 98] and connected superconducting waveguides [71].

Assuming the coupling and potentials can be sufficiently well controlled, one can create a network version of the Gross-Pitaevskii model of BEC wavefunctions. Just as in the Swift-Hohenberg example, we take the Gross-Pitaevskii equation for a complex wavefunction ψ and replace the continuous Laplacian ∇^2 with its discrete analog $-L$:

$$i\frac{d\psi_j}{dt} = \sum_{k=1}^{n} L_{jk}\psi_k + g|\psi_j|^2\psi_j. \tag{4.20}$$

This discrete nonlinear Schrödinger equation [11, 107] can be written $i\frac{d\psi_i}{dt} = \frac{\partial E}{\partial \psi_i^*}$, where the energy E is the sum of the kinetic energy $T = \sum_{i,j} \psi_i^* L_{ij} \psi_j$ and the potential energy $U = \frac{1}{2}g\sum_j (\psi_j^*\psi_j)^2$. In the special case of a lattice system, T would include cross-site interaction energies. The potential energy quantifies the localization of ψ: with $g > 0$, it is large when the probability $\psi^*\psi$ is concentrated at a single vertex and small when $\psi^*\psi$ is spread out. Delocalization is limited by the size of the network, as $U \geq \frac{g}{2n}$, but can vary widely even on a finite network. If ψ is initialized at a single vertex j, then $U = g/2$, independent of j, while $T = L_{jj}$ equals the degree of j.

We find that the interplay of the total energy conservation constraint in such a model with the kinetic energy gap inhibits spreading of the wavefunction on DBG networks. The effect is reminiscent of Anderson localization [7] and could appear in similar experimental setups [22, 115], though the mechanism is distinct. Since energy is conserved, the wavefunction can delocalize and reduce its potential energy only

by converting it to kinetic energy. The rate of potential energy loss, set by g, must therefore match the rate of kinetic energy gain, set by the differences in eigenvalues among the modes involved. Suppose the wavefunction is mostly in a localized mode j with eigenvalue λ_j. Spreading to a higher mode k with $\lambda_k - \lambda_j \gg g$ would increase kinetic energy by more than it would decrease potential energy, while a weak higher mode $0 < \lambda_k - \lambda_j \ll g$ or a lower mode $\lambda_k < \lambda_j$ would not increase kinetic energy by enough, if at all. Both are barred by energy conservation. The amplitude in mode j can only be reduced if there are other modes k with $\lambda_k \sim \lambda_j + g$.

To see this in more detail, suppose we have a wavefunction comprising two modes, $\psi_j = c_1 v_j^{(1)} + c_2 v_j^{(2)}$, with initial complex amplitudes c_1, c_2. Suppose also that these eigenmodes are localized on two different vertices, with $v^{(1)} \approx (-1, \epsilon, \epsilon, \ldots, \epsilon)$ and $v^{(2)} \approx (\epsilon, -1, \epsilon, \ldots, \epsilon)$. The system energy as a function of c_1 and c_2 is then

$$E = \lambda_1 |c_1|^2 + \lambda_2 |c_2|^2 + \tfrac{1}{2} g \left[|c_1|^4 + |c_2|^4 + O(\epsilon) \right].$$

If the squared amplitudes change slightly, to $|c_1|^2 - \delta$ and $|c_2|^2 + \delta$, the change in energy to leading order in δ is

$$\Delta E = \left[\lambda_2 - \lambda_1 + g \left(|c_2|^2 - |c_1|^2 \right) \right] \delta + O(\epsilon).$$

Conservation of energy requires $\Delta E = 0$, so in order to transfer a noticeable amplitude $\delta \gg \epsilon$ from the first mode to the second we must have $\lambda_2 - \lambda_1 + g(|c_2|^2 - |c_1|^2) \approx 0$. In the cases considered in Fig. 4-5, where $|c_1| \approx 1$ and $|c_2| \approx 0$, this reduces to $\lambda_2 - \lambda_1 \approx g$. Thus on a network with a spectral gap, the localization of ψ can depend non-trivially on the interplay between g and the spectrum.

Initializing ψ at a weakly-connected vertex brings out this interplay as g is varied. The initial state, with high potential energy and low kinetic energy, is localized on modes with eigenvalue below the spectral gap. On the sparsified network, a low value of g makes nearby modes below the gap accessible for delocalization, causing the wavefunction to spread (Fig. 4-5a). However, increasing g pushes the region where transfer is possible inside the spectral gap, inhibiting the spread of the wavefunction

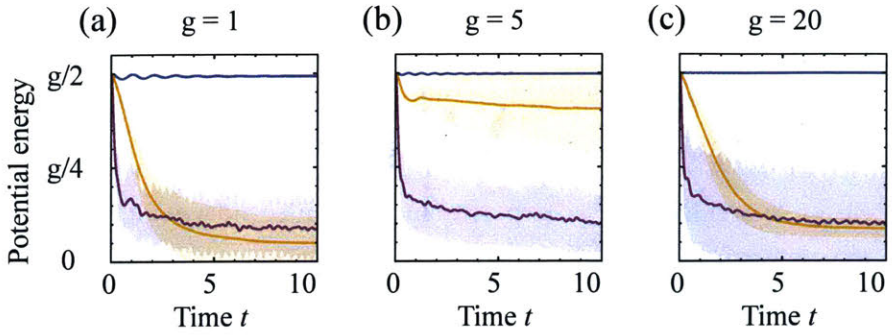

Figure 4-5: Localization on a DBG quantum network. (a-c), When the wavefunction in the Gross-Pitaevskii model of Eq. (4.20) is initialized at a weakly connected vertex with low kinetic energy, localization or delocalization (indicated by high or low potential energy, respectively) is controlled by the interplay between the graph spectrum and the rate of potential energy loss g. The random graph (purple) always delocalizes, due to its dense spectrum. However, while the sparsified graph (yellow) can delocalize for low g (a) and high g (c), again due to available eigenmodes, intermediate g (b) places the range of allowed modes inside the spectral gap, preventing delocalization. The complete graph (blue) always inhibits spreading due to the extreme localization of its eigenvectors.

on the sparsified network (Fig. 4-5b). Further increase of g once again enables delocalization as the modes above the gap becomes accessible for energy transfer (Fig. 4-5c). In contrast, the dense spectrum of the random graph means delocalization occurs in all three instances (Fig. 4-5). Interestingly, the complete DBG network appears to remain localized for all values of g in our simulations (Fig. 4-5); this is likely due to the strong localization and near-zero overlap of the eigenmodes.

Experimentally, this could be realized either with BECs in appropriately-tuned optical potentials or as a physical network of waveguides. Building the large complete networks we introduced is beyond current experimental techniques but may be possible with future advancements. For the short term, we will show in the next section how extending smaller, low-connectivity networks periodically can lead to more practical networks with approximately the same spectral properties.

4.4 Band structure in periodic networks

High connectivity can make it difficult to build experimental versions of complex networks. This motivated our study of spectral sparsification, as the sparsified graphs should be easier to realize in an experiment. An alternative approach to making practically-usable networks is to create a periodic crystal where we control the behavior of the unit cell. Keeping the unit cell small will reduce the connectivity and simplify fabrication, while the periodic structure will enable building on a larger scale. The key question is then: can the spectrum of the full system be controlled by tuning only the unit cell? In what follows, we show that it can.

We can construct infinite periodic networks in a standard way from any base network G by tiling periodically and rewiring edges (Fig. 4-6a,d). Starting from the original vertex set $\{j\}$ for $1 \leq j \leq n$ and edge weights $-L_{jk}$, we make an infinite string G^∞ of copies of G with vertices indexed by j, the label in G, and $c \in \mathbb{Z}$, the unit cell. This will give a new, infinite Laplacian L^∞. For the edges that will not be rewired, we set $L^\infty_{jc,kc} = L_{jk}$ for all c. Doing this for all edges would leave the copies of G disconnected. To connect them, we choose a subset of edges $\{(j,k)\}$ and rewire them to cross between unit cells; for example, if (j,k) is an edge to be rewired to have k in a unit cell to the left of j we can set $L^\infty_{jc,k(c-1)} = L_{jk}$ for all c and symmetrically set $L^\infty_{k(c-1),jc} = L_{kj}$. The remainder of the entries of L^∞ are set to zero.

Since L^∞ is periodic, Bloch's Theorem allows us to write the eigenvectors as

$$U^\infty_{jc}(q) = e^{iqc}\tilde{U}_j(q),$$

where q is a wavenumber in the first Brilloun zone $-\pi < q < \pi$. The $\tilde{U}$ then satisfy

$$\lambda(q)e^{iqc}\tilde{U}_j(q) = \sum_{k,d} L^\infty_{jc,kd}e^{iqd}\tilde{U}_k(q),$$

which reduces to a new eigenvalue equation for a matrix of size n:

$$\lambda(q)\tilde{U}(q) = \tilde{L}(q)\tilde{U}(q),$$

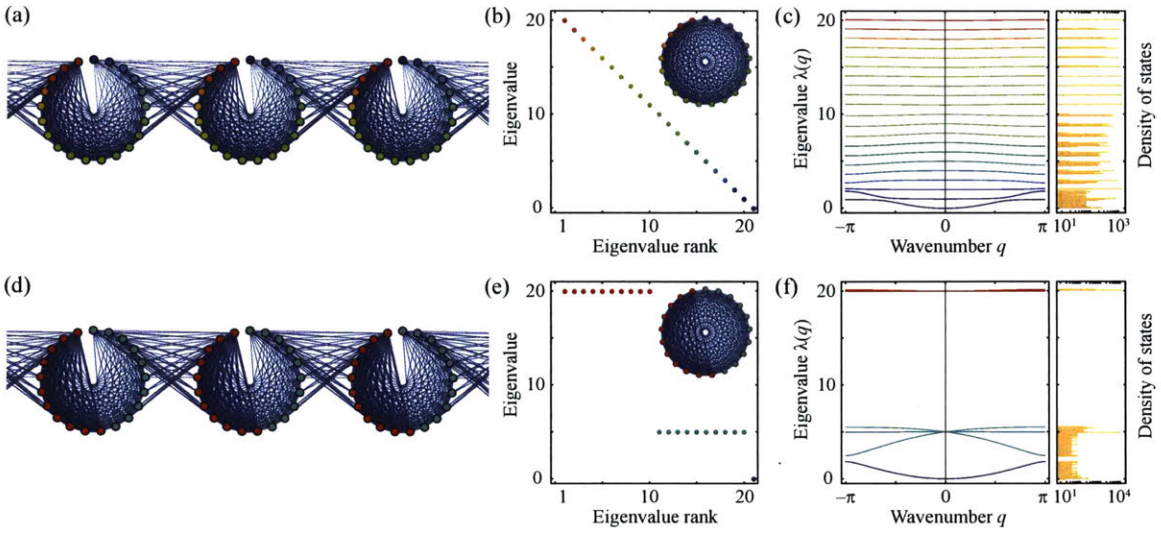

Figure 4-6: Designed spectra on a discrete network are preserved when extended periodically in one dimension. (a) We extend a finite network to an infinite one by rewiring a subset of the edges to cross between adjacent copies of the original network. Here, we take the network with the spectrum in (b) and rewired the edge between vertices j and k if $|k-j| > n/2$. This rewires roughly one quarter of the edges. (b) One unit cell in (a) would have a discrete spectrum with $\lambda_j = 21 - j$. (c) Most of the eigenvalue bands do not change significantly with q, so the density of states consists of 21 sharp peaks with low- or zero-density regions between. (d) The same construction as in (a) can be repeated for any spectrum; this is the result for a gapped network. (e) One unit cell in (d) would have a gapped spectrum, with 10 eigenvalues equal to 20 and 10 equal to 5, in addition to the always-present zero eigenvalue. (f) Again, most of the eigenvalue bands are roughly constant, even though the eigenvectors do depend strongly on q. The gap in the middle of the spectrum is nearly perfectly preserved; a small gap remains between the bottom two bands. Note the log scale on both density of states plots.

where the matrix elements of $\tilde{L}(q)$ are the same as those of L for edges within a single unit cell and differ by a factor $e^{iq(c-d)}$ for edges that cross between unit cells c and d.

Using these transformations, which are standard in the study of lattice systems [79], we can find the continuous spectra of periodic tilings of our designed networks. Even without any optimization of which edges to rewire, the spectral characteristics can persist in the infinite system. If we rewire all edges with $|j-k| > n/2$, for example, a spectrum of equally-spaced eigenvalues leads to a density of states with corresponding equally-spaced large spikes (Fig. 4-6a-c), while a discrete band gap is almost entirely preserved (Fig. 4-6d-f). In both cases, only the bottom few bands vary significantly

with q even though by rewiring approximately one quarter of the edges we are far from a small perturbation. Note that, because we moved edges incident to the first vertex, all of the eigenvectors do change and are not localized for nonzero q. We have observed this preservation of the spectrum consistently in a small number of examples; in the future, it would be useful to investigate the exact conditions on rewiring necessary to keep the spectrum nearly independent of q.

4.5 Conclusions

Controlling dynamics on a network typically requires detailed understanding of its spectral properties. Here we have reversed the conventional approach by starting from a desired spectrum and providing a mathematically rigorous construction of a matching network. This enabled us to induce chimera states, suppress or fine-tune pattern formation, and control wavefunction localization [6] using suitably designed gapped spectra.

We introduced our three applications only to showcase a few possibilities and we expect the construction to be useful in many other contexts. Still, these three already provide opportunities for experimental realizations, including computer-coupled chemical oscillators [134], cold atomic systems with precisely-specified optical potentials [22, 28, 34, 54, 98], or etched superconducting waveguide resonators [71]. For metamaterials that can be approximated as spring networks, designing the Laplacian would determine the transmission properties and allow selective acoustic damping. Diffusive transport networks designed with these principles could have mixing times controlled independently for different initial conditions. Any of these models can also be naturally extended to periodic systems, where the spectral properties are preserved well without any further optimization.

Our method, which starts from global properties, complements traditional approaches using small-scale local rules to build and analyze networks [12, 20, 78, 91]. In the future, the above results may also prove useful as a standard of comparison for other networks. Contrasting the dynamics on an important class of networks with

the dynamics on networks designed to have identical spectra can help identify the important features of that class. Moreover, as dynamics are often related to matrices other than the Laplacian [149], it will be interesting to investigate control of their spectra for weighted networks as well. Although our construction works optimally with fully-connected graphs, one can expect that improved sparsification algorithms together with recent progress in 3D printing and lithography [29, 82] may soon lead to physically-realizable networks with arbitrary gaps; since any graph can be embedded in 3D [37], the framework introduced here lays a conceptual foundation for the targeted design of complex non-periodic metamaterials with desired spectral properties.

Bibliography

[1] Réka Albert and Albert-László Barabási. Statistical mechanics of complex networks. *Rev. Mod. Phys.*, 74(1):47, 2002.

[2] Karen Alim, Gabriel Amselem, François Peaudecerf, Michael P. Brenner, and Anne Pringle. Random network peristalsis in Physarum polycephalum organizes fluid flows across an individual. *Proc. Natl. Acad. Sci. U.S.A.*, 110(33):13306–13311, 2013.

[3] Karen Alim, Natalie Andrew, and Anne Pringle. Physarum. *Curr. Biol.*, 23(24):R1082–R1083, 2013.

[4] Karen Alim, Natalie Andrew, Anne Pringle, and Michael P. Brenner. Mechanism of signal propagation in Physarum Polycephalum. *Proc. Natl. Acad. Sci. USA*, 114(20):5136–5141, 2017.

[5] Amir Amir, Yuval Oreg, and Yoseph Imry. Localization, anomalous diffusion, and slow relaxations: A random distance matrix approach. *Phys. Rev. Lett.*, 105(7):070601, 2010.

[6] Ariel Amir, Jacob J. Krich, Vincenzo Vitelli, Yuval Oreg, and Yoseph Imry. Emergent percolation length and localization in random elastic networks. *Phys. Rev. X*, 3(2):021107, 2013.

[7] P. W. Anderson. Absence of diffusion in certain random lattices. *Phys. Rev.*, 109(5):1492–1505, 1958.

[8] Alex Arenas, Albert Diaz-Guilera, and Conrad J. Perez-Vicente. Synchronization reveals topological scales in complex networks. *Phys. Rev. Lett.*, 96(11):114102, 2006.

[9] Peter Ashwin and Oleksandr Burylko. Weak chimeras in minimal networks of coupled phase oscillators. *Chaos*, 25(1):013106, 2015.

[10] Jayanth R. Banavar, Francesca Colaiori, Alessandro Flammini, Amos Maritan, and Andrea Rinaldo. Topology of the fittest transportation network. *Phys. Rev. Lett.*, 84(20):4745, 2000.

[11] Ole Bang, Jens Juul Rasmussen, and Peter L. Christiansen. Subcritical localization in the discrete nonlinear Schrodinger equation with arbitrary power nonlinearity. *Nonlinearity*, 7(1):205–218, 1994.

[12] Albert-László Barabási and Réka Albert. Emergence of scaling in random networks. *Science*, 286(5439):509–512, 1999.

[13] J. Bardeen, L. N. Cooper, and J. R. Schrieffer. Theory of superconductivity. *Phys. Rev.*, 108(5):1175–1204, 1957.

[14] Murray T. Batchelor, J. Suzuki, and C. M. Yung. Exact results for Hamiltonian walks from the solution of the fully packed loop model on the honeycomb lattice. *Phys. Rev. Lett.*, 73(20):2646, 1994.

[15] Werner Baumgarten, Tetsuo Ueda, and Marcus J. B. Hauser. Plasmodial vein networks of the slime mold Physarum polycephalum form regular graphs. *Phys. Rev. E*, 82(4):046113, 2010.

[16] Rodney J. Baxter. *Exactly Solved Models in Statistical Mechanics.* Academic Press, San Diego, CA, 1982.

[17] Olivier Benichou, Thomas Guérin, and Raphaël Voituriez. Mean first-passage times in confined media: from Markovian to non-Markovian processes. *J. Phys. A: Math. Theor.*, 48(16):163001, 2015.

[18] Nirveek Bhattacharjee, Arturo Urrios, Shawn Kang, and Albert Folch. The upcoming 3d-printing revolution in microfluidics. *Lab Chip*, 16:1720–1742, 2016.

[19] Ginestra Bianconi. Interdisciplinary and physics challenges of Network Theory. *EPL*, 111:56001, 2015.

[20] Ginestra Bianconi and Albert-László Barabási. Competition and multiscaling in evolving networks. *Europhys. Lett.*, 54(4):436–442, 2000.

[21] Ginestra Bianconi, Paolo Pin, and Matteo Marsili. Assessing the relevance of node features for network structure. *Proc. Natl. Acad. Sci. U.S.A.*, 106(28):11433–11438, 2009.

[22] Juliette Billy, Vincent Josse, Zhanchun Zuo, Alain Bernard, Ben Hambrecht, Pierre Lugan, David Clément, Laurent Sanchez-Palencia, Philippe Bouyer, and Alain Aspect. Direct observation of Anderson localization of matter waves in a controlled disorder. *Nature*, 453(7197):891–894, 2008.

[23] B. Bradlyn, L. Elcoro, J. Cano, M. G. Vergniory, Z. Wang, C. Felser, M. I. Aroyo, and B. A. Bernevig. Topological quantum chemistry. *Nature*, 547(7663):298–305, 2017.

[24] Antoine Bricard, Jean-Baptiste Caussin, Nicolas Desreumaux, Olivier Dauchot, and Denis Bartolo. Emergence of macroscopic directed motion in populations of motile colloids. *Nature*, 503(7474):95–98, 2013.

[25] Dirk Brockmann, Lars Hufnagel, and Theo Geisel. The scaling laws of human travel. *Nature*, 439(7075):462–465, 2006.

[26] Jonathan E. Bronson, Jingyi Fei, Jake M. Hofman, Ruben L. Gonzalez, and Chris H. Wiggins. Learning Rates and States from Biophysical Time Series: A Bayesian Approach to Model Selection and Single-Molecule FRET Data. *Biophys. J.*, 97(12):3196–3205, 2009.

[27] Richard A. Brualdi and Stephen Mellendorf. Regions in the Complex Plane Containing the Eigenvalues of a Matrix. *Am. Math. Mon.*, 101(10):975–985, 1994.

[28] I. Brunelli, G. Giusiano, F. P. Mancini, P. Sodano, and A. Trombettoni. Topology-induced spatial Bose-Einstein condensation for bosons on star-shaped optical networks. *J. Phys. B*, 37(7):S275–S286, 2004.

[29] Tiemo Bückmann, Nicolas Stenger, Muamer Kadic, Johannes Kaschke, Andreas Frölich, Tobias Kennerknecht, Christoph Eberl, Michael Thiel, and Martin Wegener. Tailored 3D mechanical metamaterials made by dip-in direct-laser-writing optical lithography. *Adv. Mater.*, 24(20):2710–2714, 2012.

[30] Jerome Buhl, David J. T. Sumpter, Iain D. Couzin, Joe J. Hale, Emma Despland, E. R. Miller, and Steve J. Simpson. From disorder to order in marching locusts. *Science*, 312(5778):1402–1406, 2006.

[31] Ed Bullmore and Olaf Sporns. Complex brain networks: graph theoretical analysis of structural and functional systems. *Nat. Rev. Neurosci.*, 10(3):186–198, 2009.

[32] P. S. Burada and B. Lindner. Escape rate of an active brownian particle over a potential barrier. *Phys. Rev. E*, 85:032102, 2013.

[33] Soline Chanet, Callie J. Miller, Eeshit Dhaval Vaishnav, Bard Ermentrout, Lance A. Davidson, and Adam C. Martin. Actomyosin meshwork mechanosensing enables tissue shape to orient cell force. *Nat. Comm.*, 8:15014, 2017.

[34] Lawrence W. Cheuk, Matthew A. Nichols, Melih Okan, Thomas Gersdorf, Vinay V. Ramasesh, Waseem S. Bakr, Thomas Lompe, and Martin W. Zwierlein. Quantum-gas microscope for fermionic atoms. *Phys. Rev. Lett.*, 114:193001, 2015.

[35] Young Sul Cho, Takashi Nishikawa, and Adilson E. Motter. Stable Chimeras and Independently Synchronizable Clusters. *Phys. Rev. Lett.*, 119(8):084101, 2017.

[36] Joel E. Cohen and Paul Horowitz. Paradoxical behaviour of mechanical and electrical networks. *Nature*, 352(6337):699–701, 1991.

[37] Robert F. Cohen, Peter Eades, Tao Lin, and Frank Ruskey. Three-dimensional graph drawing. *Algorithmica*, 17(2):199–208, 1997.

[38] Francesc Comellas and Jordi Diaz-Lopez. Spectral reconstruction of complex networks. *Phys. A*, 387(25):6436–6442, 2008.

[39] Francis Corson. Fluctuations and redundancy in optimal transport networks. *Phys. Rev. Lett.*, 104(4):048703, 2010.

[40] Dragoš Cvetkovič. Spectral recognition of graphs. *Yugoslav J. Oper. Res.*, 22(2):145–161, 2012.

[41] Lucilla De Arcangelis, Joel Koplik, Sidney Redner, and David Wilkinson. Hydrodynamic dispersion in network models of porous media. *Phys. Rev. Lett.*, 57(8):996, 1986.

[42] Madalena M. Dias and Alkiviades C. Payatakes. Network models for two-phase flow in porous media. Part 1. Immiscible microdisplacement of non-wetting fluids. *J. Fluid Mech.*, 164:305–336, 1986.

[43] J. Dunkel, W. Ebeling, U. Erdmann, and V. A. Makarov. Coherent motions and clusters in a dissipative Morse ring chain. *Int. J. Bifurcat. Chaos*, 12(11):2359–2377, 2002.

[44] Jörn Dunkel, Sebastian Heidenreich, Knut Drescher, Henricus H. Wensink, Markus Bär, and Raymond E. Goldstein. Fluid dynamics of bacterial turbulence. *Phys. Rev. Lett.*, 110(22):228102, 2013.

[45] W. Ebeling, U. Erdmann, J. Dunkel, and M. Jenssen. Nonlinear dynamics and fluctuations of dissipative Toda chains. *J. Stat. Phys.*, 101(1/2):443–457, October 2000.

[46] Aden Forrow, Francis G. Woodhouse, and Jörn Dunkel. Mode Selection in Compressible Active Flow Networks. *Phys. Rev. Lett.*, 119(2):028102, 2017.

[47] Michael J. Fuerstman, Pascal Deschatelets, Ravi Kane, Alexander Schwartz, Paul J.A. Kenis, John M. Deutch, and George M. Whitesides. Solving mazes using microfluidic networks. *Langmuir*, 19(11):4714–4722, 2003.

[48] S. Fürthauer, M. Neef, S. W. Grill, K. Kruse, and F Jülicher. The Taylor–Couette motor: spontaneous flows of active polar fluids between two coaxial cylinders. *New J. Phys.*, 14(2):023001, 2012.

[49] L. Gammaitoni, P. Hänggi, P. Jung, and F. Marchesoni. Stochastic resonance. *Rev. Mod. Phys.*, 70(1):223–287, 1998.

[50] Mauro Garavello and Benedetto Piccoli. *Traffic Flow on Networks.* American Institute of Mathematical Sciences, Springfield, MO, 2006.

[51] Yuval Gazit, David A. Berk, Michael Leunig, Laurence T. Baxter, and Rakesh K. Jain. Scale-invariant behavior and vascular network formation in normal and tumor tissue. *Phys. Rev. Lett.*, 75(12):2428, 1995.

[52] A. Sydney Gladman, Elisabetta A. Matsumoto, Ralph G. Nuzzo, L. Mahadevan, and Jennifer A. Lewis. Biomimetic 4d printing. *Nat. Mater.*, 15(4):413–418, 2016.

[53] Chris Godsil and Gordon F. Royle. *Algebraic Graph Theory.* Springer-Verlag, New York, NY, 2001.

[54] Markus Greiner, Olaf Mandel, Tilman Esslinger, Theodor W. Hänsch, and Immanuel Bloch. Quantum phase transition from a superfluid to a Mott insulator in a gas of ultracold atoms. *Nature*, 415:39–44, 2002.

[55] Geoffrey Grimmett. *Probability on Graphs: Random Processes on Graphs and Lattices.* Cambridge University Press, 2010.

[56] Jacob Halatek and Erwin Frey. Highly Canalized MinD Transfer and MinE Sequestration Explain the Origin of Robust MinCDE-Protein Dynamics. *Cell Rep.*, 1(6):741–752, 2012.

[57] Lorenz Halbeisen and Norbert Hungerbühler. Reconstruction of Weighted Graphs by their Spectrum. *Eur. J. Comb.*, 21(5):641–650, 2000.

[58] Melinda Y. Han, Barbaros Özyilmaz, Yuanbo Zhang, and Philip Kim. Energy band-gap engineering of graphene nanoribbons. *Phys. Rev. Lett.*, 98(20):206805, 2007.

[59] Peter Hänggi, Peter Talkner, and Michal Borkovec. Reaction-rate theory: fifty years after Kramers. *Rev. Mod. Phys.*, 62(2):251, 1990.

[60] M. Z. Hasan and C. L. Kane. Colloquium: Topological insulators. *Rev. Mod. Phys.*, 82(4):3045–3067, 2010.

[61] Limei Huang, Ruiqi Jiang, Jingjun Wu, Jizhou Song, Hao Bai, Bogeng Li, Qian Zhao, and Tao Xie. Ultrafast digital printing toward 4d shape changing materials. *Adv. Mater.*, 29(7):1605390, 2017.

[62] Geertjan Huiskamp. Difference formulas for the surface Laplacian on a triangulated surface. *J. Comp. Phys.*, 95(2):477–496, 1991.

[63] Pierre Illien, Olivier Bénichou, Gleb Oshanin, and Raphaël Voituriez. Velocity anomaly of a driven tracer in a confined crowded environment. *Phys. Rev. Lett.*, 113(3):030603, 2014.

[64] Mads Ipsen and Alexander S. Mikhailov. Evolutionary reconstruction of networks. *Phys. Rev. E*, 66(4):046109, 2002.

[65] Hawoong Jeong, Bálint Tombor, Réka Albert, Zoltan N. Oltvai, and A-L Barabási. The large-scale organization of metabolic networks. *Nature*, 407(6804):651–654, 2000.

[66] Xin Jiang and Daniel M. Abrams. Symmetry-broken states on networks of coupled oscillators. *Phys. Rev. E*, 93(5):052202, 2016.

[67] Eleni Katifori, Gergely J. Szöllősi, and Marcelo O. Magnasco. Damage and fluctuations induce loops in optimal transport networks. *Phys. Rev. Lett.*, 104(4):048704, 2010.

[68] Jonathan A. Kelner and Alex Levin. Spectral Sparsification in the Semi-streaming Setting. *Theory Comp. Syst.*, 53(2):243–262, 2013.

[69] Rex A. Kerr, Herbert Levine, Terrence J. Sejnowski, and Wouter-Jan Rappel. Division accuracy in a stochastic model of Min oscillations in Escherichia coli. *Proc. Natl. Acad. Sci. U.S.A.*, 103(2):347–352, 2006.

[70] Aleksandr I. Khinchin. *Mathematical Foundations of Statistical Mechanics*. Dover, New York, 1949.

[71] Alicia J. Kollár, Mattias Fitzpatrick, and Andrew A. Houck. Hyperbolic Lattices in Circuit Quantum Electrodynamics. arXiv:1802.09549, 2018.

[72] Jané Kondev. Liouville field theory of fluctuating loops. *Phys. Rev. Lett.*, 78(23):4320, 1997.

[73] Justus Kromer, Ali Khaledi-Nasab, Lutz Schimansky-Geier, and Alexander B. Neiman. Emergent stochastic oscillations and signal detection in tree networks of excitable elements. *Sci. Rep.*, 7(1):1–13, 2017.

[74] Yoshiki Kuramoto. Self-entrainment of a population of coupled non-linear oscillators. *Int. Symp. Math. Prob. Theor. Phys.*, 39:420–422, 1975.

[75] Yoshiki Kuramoto and Dorjsuren Battogtokh. Coexistence of Coherence and Incoherence in Nonlocally Coupled Phase Oscillators. *Nonlinear Phenom. Complex Syst.*, 5(4):380–385, 2002.

[76] J. Lega, J. V. Moloney, and A. C. Newell. Swift-Hohenberg Equation for Lasers. *Phys. Rev. Lett.*, 73(22):2978–2981, 1994.

[77] Benjamin Lindner, Jordi Garcıa-Ojalvo, Alexander Neiman, and Lutz Schimansky-Geier. Effects of noise in excitable systems. *Phys. Rep.*, 392(6):321–424, 2004.

[78] Tom Lorimer, Florian Gomez, and Ruedi Stoop. Two universal physical principles shape the power-law statistics of real-world networks. *Sci. Rep.*, 5(1):12353, 2015.

[79] T. C. Lubensky, C. L. Kane, X. Mao, A. Souslov, and K. Sun. Phonons and elasticity in critically coordinated lattices. *Rep. Prog. Phys.*, 073901:73901, 2015.

[80] Enkeleida Lushi, Hugo Wioland, and Raymond E. Goldstein. Fluid flows created by swimming bacteria drive self-organization in confined suspensions. *Proc. Natl. Acad. Sci. U.S.A.*, 111(27):9733–9738, 2014.

[81] Ben D. MacArthur, Rubén J. Sánchez-García, and James W Anderson. Symmetry in complex networks. *Discrete Appl. Math.*, 156(18):3525–3531, 2008.

[82] Weining Man, Marian Florescu, Kazue Matsuyama, Polin Yadak, Geev Nahal, Seyed Hashemizad, Eric Williamson, Paul Steinhardt, Salvatore Torquato, and Paul Chaikin. Photonic band gap in isotropic hyperuniform disordered solids with low dielectric contrast. *Opt. Express*, 21(17):19972–19981, 2013.

[83] Daniel Marbach, James C. Costello, Robert Küffner, Nicole M. Vega, Robert J. Prill, Diogo M. Camacho, Kyle R. Allison, The DREAM5 Consortium, Manolis Kellis, James J. Collins, and Gustavo Stolovitzky. Wisdom of crowds for robust gene network inference. *Nat. Meth.*, 9(8):796–804, 2012.

[84] Sophie Marbach, Karen Alim, Natalie Andrew, Anne Pringle, and Michael P. Brenner. Pruning to Increase Taylor Dispersion in Physarum polycephalum Networks. *Phys. Rev. Lett.*, 117(17), 2016.

[85] M. C. Marchetti, J.-F. Joanny, S. Ramaswamy, T. B. Liverpool, J. Prost, Madan Rao, and R. Aditi Simha. Hydrodynamics of soft active matter. *Rev. Mod. Phys.*, 85(3):1143, 2013.

[86] Erik A. Martens, Shashi Thutupalli, Antoine Fourriére, and Oskar Hallatschek. Chimera states in mechanical oscillator networks. *Proc. Natl. Acad. Sci. U.S.A.*, 110(26):10563–10567, 2013.

[87] Patrick N. Mcgraw and Michael Menzinger. Laplacian spectra as a diagnostic tool for network structure and dynamics. *Phys. Rev. E*, 77(3):031102, 2008.

[88] Brendan D. McKay. On the spectral characterisation of trees. *Ars Comb.*, 3:219–232, 1977.

[89] Brendan D. McKay and Nicholas C. Wormald. Uniform Generation of Random Regular Graphs. *J. Algorithms*, 11:52–67, 1990.

[90] Giulia Menichetti, Luca Dall'Asta, and Ginestra Bianconi. Network controllability is determined by the density of low in-degree and out-degree nodes. *Phys. Rev. Lett.*, 113(7):078701, 2014.

[91] R. Milo, S. Shen-Orr, S. Itzkovitz, N. Kashtan, D. Chklovskii, and U. Alon. Network Motifs: Simple Building Blocks of Complex Networks. *Science*, 298(5594):824–827, 2002.

[92] Karolis Misiunas, Stefano Pagliara, Eric Lauga, John R. Lister, and Ulrich F. Keyser. Nondecaying hydrodynamic interactions along narrow channels. *Phys. Rev. Lett.*, 115(3):038301, 2015.

[93] Prasanta Misra. *Physics of Condensed Matter.* Elsevier Science, 2011.

[94] Adilson E. Motter. Networkcontrology. *Chaos*, 25(9):097621, 2015.

[95] Toshiyuki Nakagaki, Hiroyasu Yamada, and Ágota Tóth. Intelligence: Maze-solving by an amoeboid organism. *Nature*, 407(6803):470–470, 2000.

[96] Hiroya Nakao and Alexander S. Mikhailov. Turing patterns in network-organized activator-inhibitor systems. *Nat. Phys.*, 6(7):544–550, 2010.

[97] Tamás Nepusz and Tamás Vicsek. Controlling edge dynamics in complex networks. *Nat. Phys.*, 8(7):568–573, 2012.

[98] Matthew A. Nichols, Lawrence W. Cheuk, Melih Okan, Thomas R. Hartke, Enrique Mendez, T. Senthil, Ehsan Khatami, Hao Zhang, and Martin W. Zwierlein. Spin Transport in a Mott Insulator of Ultracold Fermions. arXiv:1802.10018, 2018.

[99] Christos Nicolaides, Ruben Juanes, and Luis Cueto-Felgueroso. Self-organization of network dynamics into local quantized states. *Sci. Rep.*, 6(1):21360, 2016.

[100] Takashi Nishikawa, Jie Sun, and Adilson E. Motter. Sensitive Dependence of Optimal Network Dynamics on Network Structure. *Phys. Rev. X*, 7:041044, 2017.

[101] Mark J. Panaggio and Daniel M. Abrams. Chimera states: coexistence of coherence and incoherence in networks of coupled oscillators. *Nonlinearity*, 28(3):R67–R87, 2015.

[102] M. Paoluzzi, R. Di Leonardo, and L. Angelani. Self-sustained density oscillations of swimming bacteria confined in microchambers. *Phys. Rev. Lett.*, 115(18):188303, 2015.

[103] Romualdo Pastor-Satorras, Claudio Castellano, Piet Van Mieghem, and Alessandro Vespignani. Epidemic processes in complex networks. *Rev. Mod. Phys.*, 87(3):925, 2015.

[104] D. J. G. Pearce and M. S. Turner. Emergent behavioural phenotypes of swarming models revealed by mimicking a frustrated anti-ferromagnet. *J. R. Soc. Interface*, 12(111):20150520, 2015.

[105] Louis M. Pecora, Francesco Sorrentino, Aaron M. Hagerstrom, Thomas E. Murphy, and Rajarshi Roy. Cluster synchronization and isolated desynchronization in complex networks with symmetries. *Nat. Comm.*, 5(May):4079, 2014.

[106] Tiago P. Peixoto. Eigenvalue spectra of modular networks. *Phys. Rev. Lett.*, 111(9):098701, 2013.

[107] D. E. Pelinovsky, D. A. Zezyulin, and V. V. Konotop. Nonlinear modes in a generalized PT-symmetric discrete nonlinear Schrödinger equation. *J. Phys. A*, 47(8):085204, 2014.

[108] Priodyuti Pradhan, Alok Yadav, Sanjiv K. Dwivedi, and Sarika Jalan. Optimized evolution of networks for principal eigenvector localization. *Phys. Rev. E*, 96(2):022312, 2017.

[109] Manu Prakash and Neil Gershenfeld. Microfluidic bubble logic. *Science*, 315(5813):832–835, 2007.

[110] Miha Ravnik and Julia M. Yeomans. Confined active nematic flow in cylindrical capillaries. *Phys. Rev. Lett.*, 110(2):026001, 2013.

[111] John W. S. B. Rayleigh. On the instability of jets. *Proc. Lond. Math. Soc.*, s1-10(1):4–13, 1878.

[112] John W. S. B. Rayleigh. *The Theory of Sound vol. 1.* Macmillan, New York, 2 edition, 1894.

[113] Chris R. Reid, Tanya Latty, Audrey Dussutour, and Madeleine Beekman. Slime mold uses an externalized spatial "memory" to navigate in complex environments. *Proc. Natl. Acad. Sci. U.S.A.*, 109(43):17490–17494, 2012.

[114] Ingmar H. Riedel-Kruse, Claudia Müller, and Andrew C. Oates. Synchrony Dynamics During Initiation, Failure, and Rescue of the Segmentation Clock. *Science*, 317(5846):1911–1915, 2007.

[115] Giacomo Roati, Chiara D'Errico, Leonardo Fallani, Marco Fattori, Chiara Fort, Matteo Zaccanti, Giovanni Modugno, Michele Modugno, and Massimo Inguscio. Anderson localization of a non-interacting Bose-Einstein condensate. *Nature*, 453(7197):895–898, 2008.

[116] Robert W. Robinson and Nicholas C. Wormald. Almost all cubic graphs are Hamiltonian. *Random Struct. Algor.*, 3(2):117–126, 1992.

[117] Pawel Romanczuk, Markus Bär, Werner Ebeling, Benjamin Lindner, and Lutz Schimansky-Geier. Active Brownian Particles. From Individual to Collective Stochastic Dynamics. *Eur. Phys. J. Spec. Top.*, 202:1–162, 2012.

[118] Pawel Romanczuk, Werner Ebeling, Udo Erdmann, and Lutz Schimansky-Geier. Active particles with broken symmetry. *Chaos*, 21(4):047517, 2011.

[119] Henrik Ronellenfitsch and Eleni Katifori. Global optimization, local adaptation, and the role of growth in distribution networks. *Phys. Rev. Lett.*, 117:138301, 2016.

[120] Conrad Sanderson and Ryan Curtin. Armadillo: a template-based C++ library for linear algebra. *J. Open Source Software*, 1:26, 2016.

[121] Frank Schweitzer, Werner Ebeling, and Benno Tilch. Complex motion of brownian particles with energy depots. *Phys. Rev. Lett.*, 80:5044–5047, 1998.

[122] Ole Sigmund and Jakob S. Jensen. Systematic design of phononic band-gap materials and structures by topology optimization. *Philos. Trans. R. Soc. A*, 361(1806):1001–1019, 2003.

[123] B. Sonnenschein, M. A. Zaks, A. B. Neiman, and L. Schimansky-Geier. Excitable elements controlled by noise and network structure. *Eur. Phys. J.: Spec. Top.*, 222(10):2517–2529, 2013.

[124] Anton Souslov, Benjamin C. van Zuiden, Denis Bartolo, and Vincenzo Vitelli. Topological sound in active-liquid metamaterials. *Nat. Phys.*, 13:1091–1094, 2017.

[125] Daniel A. Spielman and Nikhil Srivastava. Graph Sparsification by Effective Resistances. *SIAM J. Comp.*, 40(6):1913–1926, 2008.

[126] Norbert Stoop, Romain Lagrange, Denis Terwagne, Pedro M. Reis, and Jörn Dunkel. Curvature-induced symmetry breaking determines elastic surface patterns. *Nat. Mat.*, 14(3):337–342, 2015.

[127] Steven H. Strogatz. From Kuramoto to Crawford: exploring the onset of synchronization in populations of coupled oscillators. *Phys. D*, 143(1-4):1–20, 2000.

[128] Steven H. Strogatz. *Nonlinear Dynamics and Chaos.* Westview Press, Boulder, CO, 2015.

[129] J. Swift and P. C. Hohenberg. Hydrodynamic fluctuations at the convective instability. *Phys. Rev. A*, 15(1):319–328, 1977.

[130] Alexandra M. Tayar, Eyal Karzbrun, Vincent Noireaux, and Roy H. Bar-Ziv. Propagating gene expression fronts in a one-dimensional coupled system of artificial cells. *Nat. Phys.*, 11(12):1037–1041, 2015.

[131] Atsushi Tero, Seiji Takagi, Tetsu Saigusa, Kentaro Ito, Dan P. Bebber, Mark D. Fricker, Kenji Yumiki, Ryo Kobayashi, and Toshiyuki Nakagaki. Rules for biologically inspired adaptive network design. *Science*, 327(5964):439–442, 2010.

[132] Elsen Tjhung, Davide Marenduzzo, and Michael E. Cates. Spontaneous symmetry breaking in active droplets provides a generic route to motility. *Proc. Natl. Acad. Sci. U.S.A.*, 109(31):12381–12386, 2012.

[133] John Toner, Yuhai Tu, and Sriram Ramaswamy. Hydrodynamics and phases of flocks. *Ann. Phys.*, 318:170–244, 2005.

[134] Jan Frederick Totz, Julien Rode, Mark R. Tinsley, Kenneth Showalter, and Harald Engel. Spiral wave chimera states in large populations of coupled chemical oscillators. *Nat. Phys.*, 8:662–665, 2017.

[135] Edwin R. Van Dam and Willem H. Haemers. Which graphs are determined by their spectrum? *Linear Algebr. Appl.*, 373:241–272, 2003.

[136] Archana Varma, Kerwyn C. Huang, and Kevin D. Young. The Min system as a general cell geometry detection mechanism: Branch lengths in Y-shaped Escherichia coli cells affect Min oscillation patterns and division dynamics. *J. Bacteriol.*, 190(6):2106–2117, 2008.

[137] Tamás Vicsek and Anna Zafeiris. Collective motion. *Phys. Rep.*, 517(3):71–140, 2012.

[138] Kan Wang, Yung-Hang Chang, YiWen Chen, Chuck Zhang, and Ben Wang. Designable dual-material auxetic metamaterials using three-dimensional printing. *Mater. Des.*, 67:159–164, 2015.

[139] Pai Wang, Yue Zheng, Matheus C. Fernandes, Yushen Sun, Kai Xu, Sijie Sun, Sung Hoon Kang, Vincent Tournat, and Katia Bertoldi. Harnessing Geometric Frustration to Form Band Gaps in Acoustic Channel Lattices. *Phys. Rev. Lett.*, 118(8):084302, 2017.

[140] Mark E. Watkins. A theorem on Tait colorings with an application to the generalized Petersen graphs. *J. Comb. Theory*, 6(2):152–164, 1969.

[141] Duncan J. Watts and Steven H. Strogatz. Collective dynamics of 'small-world' networks. *Nature*, 393(6684):440–442, 1998.

[142] Hassler Whitney. Congruent graphs and the connectivity of graphs. *Am. J. Math.*, 54(1):150–168, 1932.

[143] Hugo Wioland, Francis G. Woodhouse, Jörn Dunkel, and Raymond E. Goldstein. Ferromagnetic and antiferromagnetic order in bacterial vortex lattices. *Nat. Phys.*, 12(4):341–345, 2016.

[144] Hugo Wioland, Francis G. Woodhouse, Jörn Dunkel, John O. Kessler, and Raymond E. Goldstein. Confinement stabilizes a bacterial suspension into a spiral vortex. *Phys. Rev. Lett.*, 110(26):268102, 2013.

[145] Francis G. Woodhouse, Aden Forrow, Joanna B. Fawcett, and Jörn Dunkel. Stochastic cycle selection in active flow networks. *Proc. Natl. Acad. Sci. U.S.A.*, 113(29):8200–8205, 2016.

[146] Francis G. Woodhouse and Raymond E. Goldstein. Spontaneous circulation of confined active suspensions. *Phys. Rev. Lett.*, 109(16):168105, 2012.

[147] Kun-Ta Wu, Jean Bernard Hishamunda, Daniel T. N. Chen, Stephen J. DeCamp, Ya-Wen Chang, Alberto Fernández-Nieves, Seth Fraden, and Zvonimir Dogic. Transition from turbulent to coherent flows in confined three-dimensional active fluids. *Science*, 355(6331):eaal1979, 2017.

[148] Mengjie Wu, Feng Xiao, Rebecca M. Johnson-Paben, Scott T. Retterer, Xiaolong Yin, and Keith B. Neeves. Single-and two-phase flow in microfluidic porous media analogs based on Voronoi tessellation. *Lab Chip*, 12(2):253–261, 2012.

[149] Gang Yan, Georgios Tsekenis, Baruch Barzel, Jean-Jacques Slotine, Yang-Yu Liu, and Albert-László Barabási. Spectrum of controlling and observing complex networks. *Nat. Phys.*, 11(9):779–786, 2015.

[150] Christian A. Yates, Radek Erban, Carlos Escudero, Iain D. Couzin, Jerome Buhl, Ioannis G. Kevrekidis, Philip K. Maini, and David J. T. Sumpter. Inherent noise can facilitate coherence in collective swarm motion. *Proc. Natl. Acad. Sci. U.S.A.*, 106(14):5464–5469, 2009.

[151] Soon-Hyung Yook, Hawoong Jeong, and Albert-László Barabási. Modeling the internet's large-scale topology. *Proc. Natl. Acad. Sci. U.S.A.*, 99(21):13382–13386, 2002.